

GEORGIA INSTITUTE OF TECHNOLOGY
ENGINEERING EXPERIMENT STATION
ATLANTA, GEORGIA 30332

FINAL TECHNICAL REPORT
EES/GIT PROJECT A-2115

360-DEGREE SCANNING ANTENNA DEVELOPMENT

By

D. G. Bodnar, W. J. Barnes, L. E. Corey and D. M. Hatcher

Under

Contract Number N00123-78-C-0468

July 1979

Prepared for

UNITED STATES NAVY
NAVAL OCEAN SYSTEMS CENTER
SAN DIEGO, CALIFORNIA 92152

ABSTRACT

A design study has been performed for a lightweight, cylindrical array antenna for a hostile-mortar-locating radar system. A mathematical model of the array was developed which permitted tradeoff studies to be made of various array parameters. Data computed using the model compared very well with experimental and other theoretical data. Critical components of the array were built and tested and shown to perform satisfactorily, and a design for the array was developed for operation at Ku-band frequencies. The antenna beam is capable of scanning 360° in azimuth and from $+3^\circ$ to $+6^\circ$ in elevation, and the estimated weight of the entire antenna is 78 pounds. The proposed antenna comprised (a) a cylindrical radiating structure composed of broadwall slots in dielectrically-loaded rectangular waveguide, (b) dielectric wedge transitions from dielectrically-loaded waveguide to parallel plates, and (c) a rotating geodesic lens for collimation of the feedhorn energy and scanning of the far-field beam.

TABLE OF CONTENTS

	<u>Page</u>
I. INTRODUCTION.....	1
A. Selection of Major Components.....	1
1. Waveguide Elements.....	2
2. Feed and Azimuth Collimating System.....	5
3. Parallel Plate to Waveguide Transition.....	9
4. Weight.....	11
B. Description of Selected Antenna.....	14
II. DESCRIPTION OF CYLINDRICAL ARRAY.....	17
A. Rotary Joint.....	20
B. Feed Horn and Azimuth-Plane Collimation.....	20
C. Transitions.....	20
D. Waveguide Arrays.....	22
E. Termination.....	22
F. Characteristics of Cylindrical Arrays.....	23
1. Element Pattern Nulls.....	23
2. Aperture Projection.....	29
3. Grating Lobes.....	32
4. Defocus of Main Beam with Elevation Steering.....	34
G. Design Procedure for Cylindrical Array.....	34
III. MATHEMATICAL ARRAY MODEL.....	39
A. Description of Mathematical Array Model.....	39
1. Element Pattern Model.....	39
2. Model of Complete Cylindrical Array.....	41
3. Verification of Array Model.....	49

TABLE OF CONTENTS (cont.)

B.	Computer Model Results.....	51
1.	Grating Lobes and Beamwidth vs. Illumination Sector..	55
2.	Grating Lobe Levels vs. Element Spacing.....	55
3.	Grating Lobe and Beamwidth vs. Radius.....	60
4.	Defocus of Main Beam vs. Steering Angle.....	72
IV.	EXPERIMENTAL MEASUREMENTS AND RESULTS.....	81
A.	Coax-to-Waveguide Adapter.....	81
B.	Parallel Plate-to-Waveguide Transition.....	95
C.	Waveguide Slotted Arrays.....	105
D.	Partial Array.....	108
V.	SUMMARY AND CONCLUSIONS.....	115
VI.	REFERENCES.....	119

LIST OF FIGURES

<u>Figure</u>	<u>Page</u>
1. Alternative design concept for cylindrical array.....	3
2. Cylindrical array composed of edge slots in rectangular waveguide...	4
3. Cylindrical array composed of broadwall slots in rectangular waveguide.....	4
4. Single-layer pillbox feed.....	6
5. Double-layer pillbox feed.....	7
6. Geodesic horn feeding waveguide end-on.....	8
7. Basic cylindrical array concept.....	10
8. Estimated weight versus antenna diameter for complete Ku-band, cylindrical array.....	13
9. Illustration of cylindrical array configuration.....	15
10. Conceptual drawing of waveguide cylindrical array.....	18
11. Antenna Feed System.....	19
12. Feed horn.....	21
13. Cylindrical waveguide slot array antenna.....	24
14. Illustration of element patterns on a cylindrical surface.....	25
15. Calculated radiation pattern for a single thin axial slot in a 36-inch diameter perfectly conducting right circular cylinder.....	26
16. Computed (by NELC) power patterns of a single energized element in an equally spaced array of slots on a conducting cylinder. Element spacings are indicated.....	27
17. Comparison of computed (by NELC) element patterns for different slot spacings on a conducting cylinder.....	28
18. Maximum illumination sector of cylindrical array antenna.....	30
19. Projected aperture from cylindrical array.....	31
20. Local grating lobes on a cylindrical array.....	33

LIST OF FIGURES (cont.)

<u>Figure</u>	<u>Page</u>
21. Coordinate System for beam steering of main beam.....	35
22. Outline of mathematical model calibration procedure.....	37
23. Block diagram of mathematical array model.....	40
24. Ring of equally spaced elements.....	42
25. Diagram of cylindrical array structure.....	43
26. Diagram of the far-field pattern of an array element with the element located at the origin of a coordinate system.....	45
27. Diagram of the far-field pattern of an array element with the element located on a cylindrical surface.....	46
28. Coordinate system for N th array element.....	47
29. Polar plot of a 7 element horizontal dipole linear array steered to 75 degrees.....	50
30. Far-field pattern for a 32 element uniformly spaced circular array..	52
31. Far-field pattern for a 7 x 13 uniformly spaced cylindrical array...	53
32. E-plane (Azimuth) radiation pattern of a 47 element cylindrical array of slotted waveguide operating at a frequency of 9.4 GHz. Conical cut, $\theta = 60^\circ$. Feed offset, $\Delta = 0.34$ in.....	54
33. Far-field pattern for cylindrical array antenna with $\lambda=0.72''$, $R = 12''$, $S = 0.42''$ and $\phi_{ill} = 120^\circ$	56
34. Far-field pattern for a cylindrical array antenna with $\lambda = 0.72''$, $R = 12''$, $S = 0.42''$ and $\phi_{ill} = 105^\circ$	57
35. Far-field pattern for a cylindrical array antenna with $\lambda = 0.72''$, $R = 12''$, $S = 0.42''$ and $\phi_{ill} = 75^\circ$	58
36. Beamwidth vs. illumination sector (ϕ_{ill}) for $\lambda = 0.72''$ and $S = 0.42''$.	59
37. Element pattern for element in cylindrical array environment with $S = 0.48'' (0.67\lambda)$	61
38. Far-field pattern for a cylindrical array antenna with $\lambda = 0.72''$, $R = 12''$, $S = 0.48''$ and $\phi_{ill} = 120^\circ$	62
39. Element pattern for element in cylindrical array environment with $S = 0.42'' (.58\lambda)$	63

LIST OF FIGURES (cont.)

<u>Figure</u>	<u>Page</u>
40. Far-field pattern for cylindrical array antenna with $\lambda = 0.72''$, $R = 12''$, $S = 0.42''$ and $\phi_{i11} = 120^\circ$	64
41. Element pattern for element in cylindrical array environment with $S = 0.36''$ (0.5λ).....	65
42. Far-field pattern for cylindrical array antenna with $\lambda = 0.72''$, $R = 12''$, $S = 0.36''$ and $\phi_{i11} = 120^\circ$	66
43. Grating lobe level vs. illumination sector (ϕ_{i11}) for element spacings of $S = 0.48''$, $S = 0.42''$ and $S = 0.36''$ with $R = 12''$ and $\lambda = .72''$	67
44. Far-field pattern for cylindrical array antenna with $\lambda = 0.72''$, $R = 10''$, $S = 0.42''$ and $\phi_{i11} = 90^\circ$	68
45. Far-field pattern for cylindrical array antenna with $\lambda = 0.72''$, $R = 12''$, $S = .42''$ and $\phi_{i11} = 90^\circ$	69
46. Far-field pattern for cylindrical array antenna with $\lambda = 0.72''$, $R = 14''$, $S = 0.42''$ and $\phi_{i11} = 90^\circ$	70
47. Grating lobe level and beamwidth vs. radius with $\lambda = 0.72''$, $S = 0.42''$ and $\phi_{i11} = 90^\circ$	71
48. Defocusing of the main beam vs. steering angle for $R = 10''$ and $\phi_{i11} = 90^\circ$	73
49. Defocusing of the main beam vs. steering angle for $R = 12''$ and $\phi_{i11} = 90^\circ$	74
50. Defocusing of main beam vs. steering angle for $R = 14''$ and $\phi_{i11} = 90^\circ$	75
51. Defocusing of the main beam vs. steering angle for $R = 12''$ and $\phi_{i11} = 60^\circ$	76
52. Defocusing of the main beam vs. steering angle for $R = 12''$ and $\phi_{i11} = 120^\circ$	77
53. Defocusing of the main beam vs. steering angle for $R = 12''$ and $\phi_{i11} = 90^\circ$. Note that $\theta_o = 4.5^\circ$	78
54. Adapter from SMA coax-to-dielectrically loaded, WR-62 waveguide.....	83
55. Return loss of a Lexan filled adapter with $SL = 0.23''$ and $PL = 0.205''$	85

LIST OF FIGURES (cont.)

<u>Figure</u>	<u>Page</u>
56. A measured return loss of two dielectrically loaded adapters connected together with an OSM load on one and the OSM load by itself.....	86
57. Dielectrically loaded, waveguide terminations.....	88
58. Return loss of Lexan adapter with Lexan waveguide load.....	89
59. Smith chart plot of impedance of Lexan coax-to-waveguide adapter as a function of frequency for SL = 0.219" and PL = 0.231".....	90
60. Return loss of X-band waveguide-to-SMA adapter with X-band waveguide load.....	91
61. Return loss of adapter as a function of back wall spacing (SL) and probe length (PL) for Stycast loading.....	92
62. Return loss of adapter as a function of back wall spacing (SL) and probe length (PL) for Rexolite loading.....	93
63. Return loss of adapter as a function of back wall spacing (SL) and probe length (PL) for Lexan loading.....	94
64. Pyramidally shaped, dielectric transition from dielectrically-loaded WR-62 waveguide to air-filled parallel plates.....	97
65. Blunt tip, pyramidally shaped, dielectric transition from dielectrically loaded WR-62 waveguide to air-filled parallel plates.....	98
66. Blunt end transition from dielectrically loaded WR-62 waveguide to air-filled parallel plates.....	99
67. Configuration for mutual coupling tests of transitions looking into parallel plates.....	100
68. Return loss from coax-to-waveguide adapter and pyramidally shaped, dielectric transition in parallel plates with TL = 3.93 inches. Dielectric is Lexan.....	101
69. Return loss vs. taper length TL for sharp tip and BL for blunt tip pyramidally shaped transitions.....	102
70. Return loss from coax-to-waveguide adapter and pyramidally shaped, dielectric, transition in parallel plates with TL = 4.13 inches. The dielectric is Lexan and no side transitions are present.....	103

LIST OF FIGURES (cont.)

<u>Figure</u>	<u>Page</u>
71. Return loss from coax-to-waveguide adapter and pyramidially shaped dielectric transition in parallel plates with TL = 4.13 inches. The dielectric is Lexan and there is one transition on either side of the active one.....	104
72. Configuration for mutual couplings tests of blunt transitions looking into parallel plates.....	106
73. Illustration of an individual slotted waveguide array used in the partial array.....	107
74. Photograph of partial array mock-up on Georgia Tech antenna range...	109
75. Azimuth plane pattern of partial array mock-up at 8.75 GHz.....	111
76. Azimuth plane pattern of partial array mock-up at 9.00 GHz.....	112
77. Azimuth plane pattern of partial array mock-up at 9.25 GHz.....	113
78. Expanded azimuth plane pattern of partial array mock-up at 8.75 GHz.	114
79. Computer Simulation of Prototype Array ($R = 20''$, $S = .715''$, $\lambda = 1.35''$, $\phi_{111} = 94.3^\circ$).....	115
80. Diagram showing elevation scanning.....	122

LIST OF TABLES

<u>Table</u>		<u>Page</u>
1.	Waveguide array weight comparisons for alternate configuration...	12
2.	Weight breakdown for alternate operating frequencies.....	12
3.	Estimated performance of complete cylindrical array antenna.....	16
4.	Dielectrics used in loaded waveguide measurements.....	82
A1.	Steering angle errors.....	119

I. INTRODUCTION

Under this program personnel of the Systems and Antennas Branch of the Engineering Experiment Station (EES) at the Georgia Institute of Technology have conducted a design study for the Naval Ocean Systems Center (NOSC) of a 360° scanning antenna for use in a lightweight hostile-mortar-locating radar system. The basic characteristics that this system must have are: (1) the total radar system must be suitable for separation into a number of pieces whose size and weight are commensurate with amphibious landings of individual Marines and (2) the system must provide a high enough degree of measurement accuracy so that counterfire can neutralize a hostile mortar. Several competing antenna concepts for this application were examined under a previous effort by EES [1], and a cylindrical array of waveguides with an electromechanical feed was recommended as the best approach. This report summarizes the results of a design study of the cylindrical array approach recommended by the preceding program. Under a companion contract [2], EES examined the radar aspects of the system.

Several element designs were considered during the study reported herein from both an electrical and a mechanical point of view. The most promising element was designed, fabricated, and tested. Other components that are critical to the successful performance of the antenna were also built and tested. All tests indicated that the proposed approaches would permit the desired performance to be obtained from the antenna.

A. Selection of Major Components

The study performed under this contract was limited to a small, lightweight cylindrical array antenna as determined from the previous study. The major components of this array are the following:

1. rotary joint
2. primary feed
3. feed collimator
4. parallel plate-to-waveguide transitions
5. dielectrically-loaded slotted waveguide arrays
6. waveguide terminations

A number of design approaches are available for each of these components. The selection process used in arriving at the final proposed configuration will be discussed next. The various design alternatives are shown in Figure 1. The radiating elements in the array can, for example, either be broadwall or edge slots. The slots in the broadwall case can either be continuous or discrete and formed out of either dielectrically loaded waveguide or printed circuit board. Coupling of the energy from the feed to the waveguides can be achieved by a number of techniques including end-on coupling and sidewall coupling. Several methods are available for collimating the energy incident on the cylindrical array of waveguides so that a collimated beam is formed in azimuth. These include a geodesic horn or a parabolic pillbox.

1. Waveguide Elements

An edge slot array consists of a series of waveguides with the broadwall of the waveguide stacked one beside the other as shown in Figure 2. Slots are cut in the outer narrow wall of the waveguide and typically wrap around into the broadwall sides of the waveguide. The edge slot array was discarded because of several problems that exist with its design. First of all the waveguides must be close together in order to obtain a reasonable active element pattern. The wrapped-around portion of the slot will be close to the wall of the next waveguide, and so the slot may be cut off. In addition, this array will be heavier since more waveguides are involved than in a broadwall slot array. Also there are problems in feeding waveguides with this orientation from the parallel plate structure which will be used to collimate the energy incident on the waveguides. For all of these reasons the edge slot array was discarded.

A printed circuit board technique can also be used for producing the radiating portion of cylindrical array. Individual dipole elements could be etched on a printed circuit board and each fed by coaxial cables. Alternately, slots could be etched in the surface to create a slotted waveguide array. Such a structure can be very lossy at X- or Ku-band and there are also problems in plating through the printed circuit board to make the sidewalls of the waveguide for this structure. Consequently, the printed circuit board approach was abandoned for the cylindrical array surface.

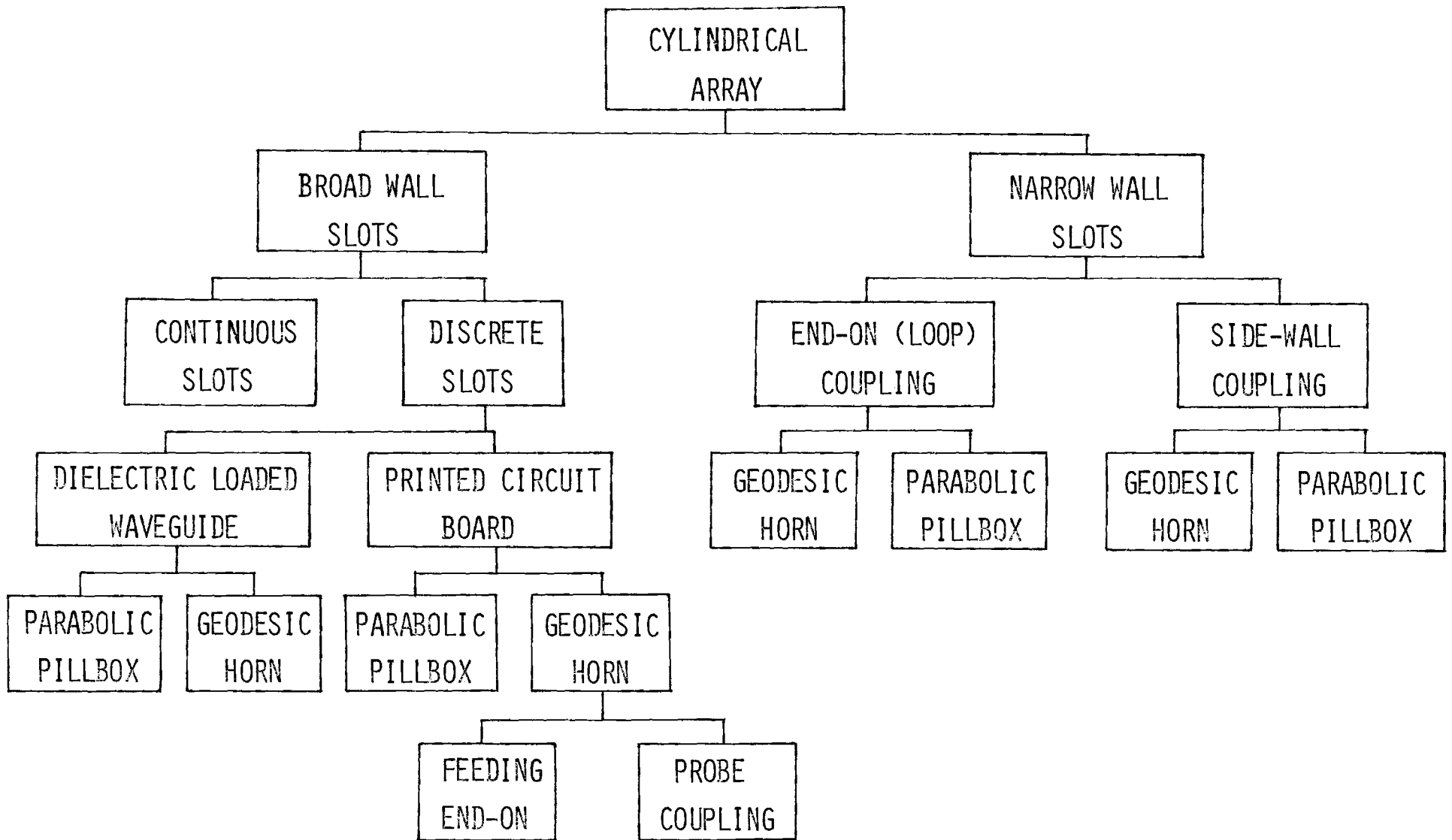


Figure 1. Alternative Design Concepts for Cylindrical Array.

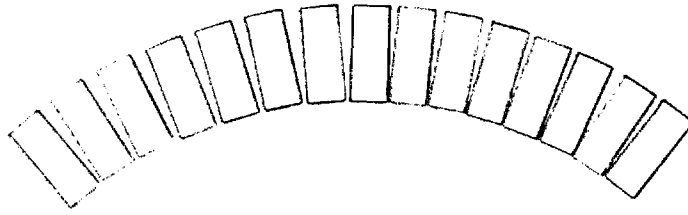


Figure 2. Cylindrical Array Composed of Edge Slots in Rectangular Waveguide.

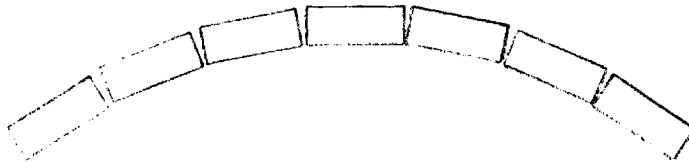


Figure 3. Cylindrical Array Composed of Broadwall Slots in Rectangular Waveguide.

A broadwall slotted array, depicted in Figure 3, consists of a group of waveguides forming a cylinder with the narrow walls of the waveguides touching one another. Fewer waveguides are involved in forming the cylindrical surface in this approach than with an edge wall slotted array. Hence, this approach will be lighter than an edge slot array. Losses in this structure will be less than for a printed circuit board array, and it is also easier to obtain a broadband coupling between the feeding structure and the waveguides for broadwall slot arrays than it is for the printed circuit board array or for the edge slot array. For these reasons it was decided that a broadwall slotted array structure was the best approach for this application.

As will be shown in Chapter III, dielectric loading is required in the waveguides to reduce their physical size. The size reduction permits the waveguides to be moved closer together and thus prevent grating lobes from being formed. The dielectric loading allows energy which would otherwise be cut off to propagate in the waveguide.

2. Feed and Azimuth Collimating System

The primary feed for the array will be a horn. Energy from this horn must be collimated in the horizontal plane to produce the proper excitation of the waveguide elements on the cylindrical surface of the array. As shown in Figure 1, there are several ways of accomplishing this collimation. Figures 4 - 6 illustrate the principal collimation techniques. The single-layer pillbox shown in Figure 4 is equivalent to a slice through a paraboloidal antenna. Energy is radiated by the feedhorn, reflected by the parabola back toward the cylinder, and finally coupled into the slots in the cylinder. This approach suffers from aperture blockage produced by the feed which in turn creates high azimuth sidelobes. This effect was observed in the antenna built under the previous contract [1]. To remedy this problem, either a double-layer pillbox as shown in Figure 5 or a geodesic lens as shown in Figure 6 can be used to replace the single-layer pillbox. Energy reflected by the near parabolic barrier in the double-layer pillbox is directed to a second parallel plate region thus avoiding blockage from the feed. This structure was examined mechanically and electrically. Although it can be designed electrically there is a problem in supporting the member between two parallel plate regions. This member

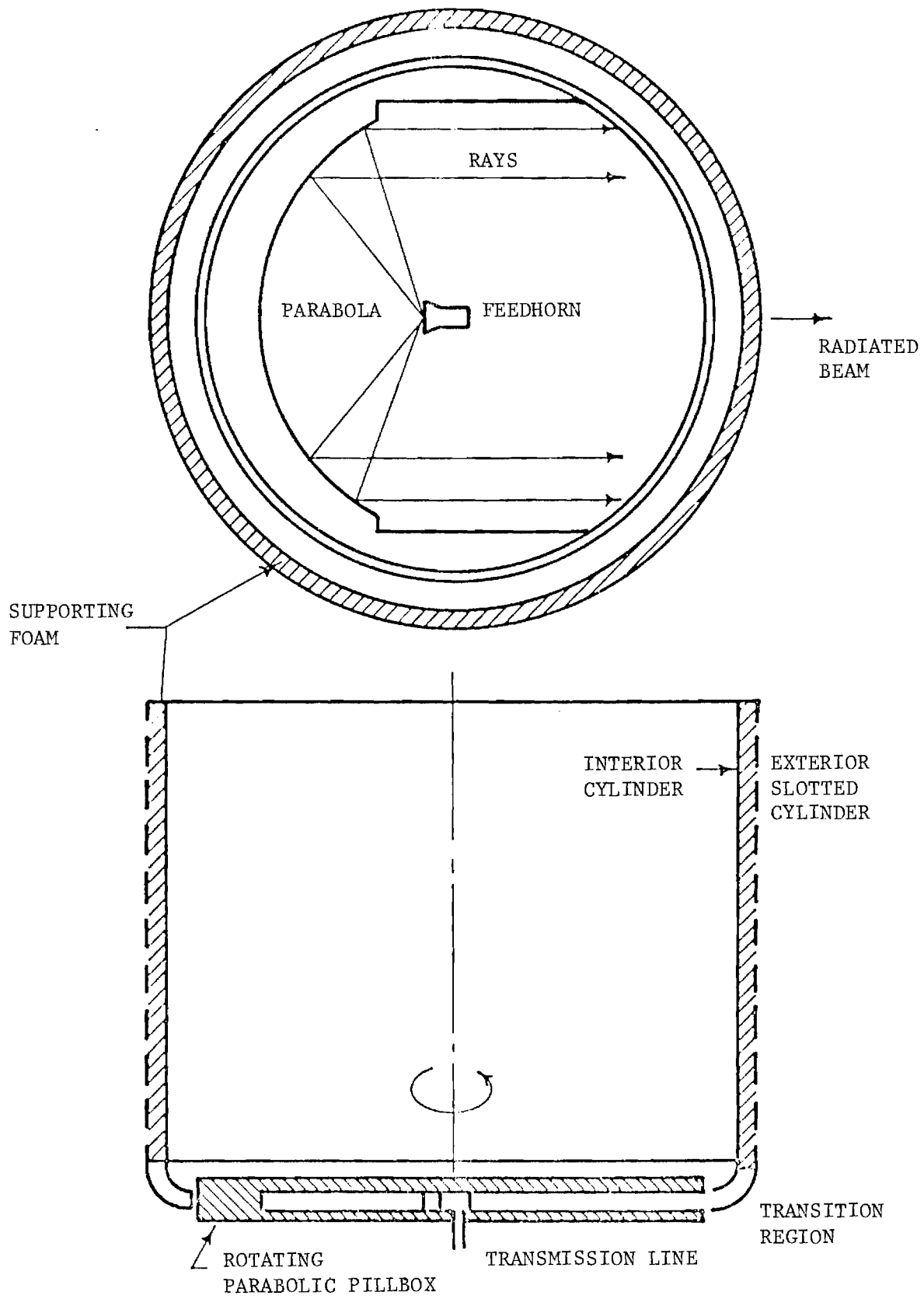


Figure 4. Single-layer Pillbox Feed.

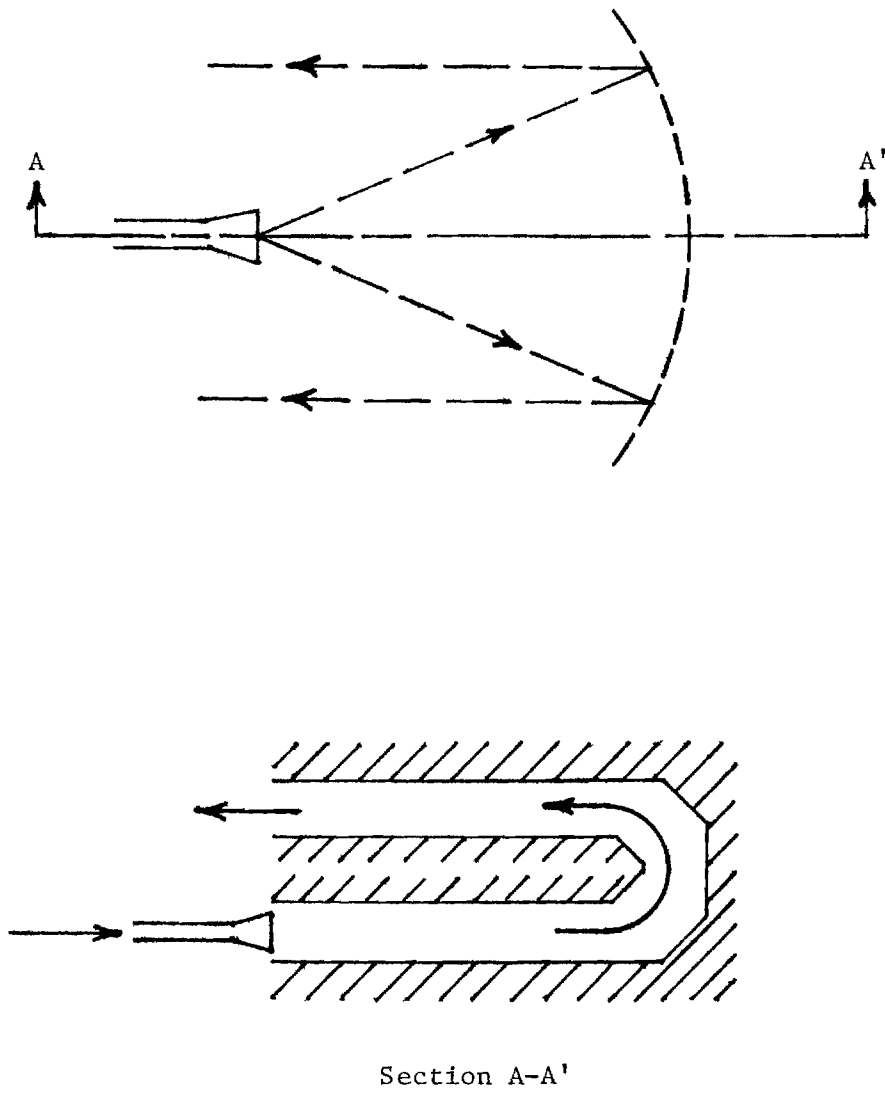


Figure 5 . Double-layer Pillbox Feed.

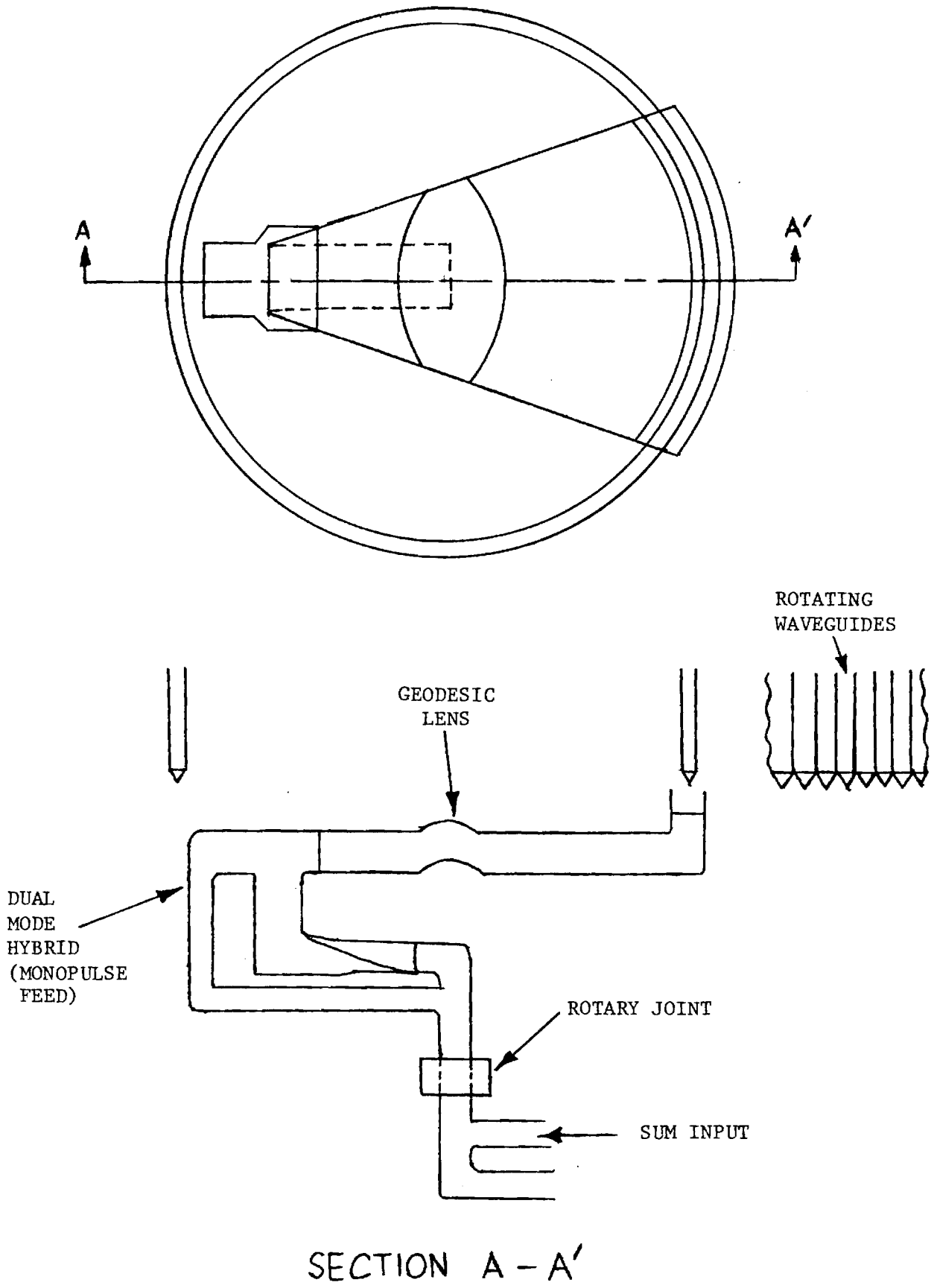


Figure 6. Geodesic Horn Feeding Waveguide End-on.

is basically a flat plate which must span the entire diameter of the cylinder. Considerable weight must be added to prevent this member from vibrating excessively. Since a light-weight antenna is mandatory for this application, the double-layer pillbox was abandoned.

A geodesic lens is formed by making a bulge in a parallel plate structure so that central rays through the lens are delayed relative to those passing through the edge of the lens. By proper selection of dimensions, an equal path-length device is produced that is very broadband. EES has built many geodesic lenses in a number of shapes and so does not anticipate any problems with building this device. The geodesic lens does not suffer from aperture blockage since energy passes through it only once. In addition it does not have the weight problem of a double-layer pillbox since it is a single-layer structure. Finally the bulge in the metal adds structural rigidity to the parallel plates. For all these reasons, the geodesic lens was selected as the azimuth collimating device.

3. Parallel Plate to Waveguide Transition

The coupling of energy from the parallel plate region into the waveguides is a major design area. The design is compounded by the fact that the waveguides are dielectrically loaded. One method for performing this coupling is shown in Figure 7 and involves using coaxial probes and cables to join the two regions. The coaxial connections are expensive. Each coax assembly costs approximately \$15 for a total of \$2,700 in material costs alone per system. These assemblies must be phase matched, which is a tedious task considering there are about 180 assemblies.

Figure 6 shows an alternate coupling scheme. The dielectric in the waveguide is extended out of the waveguide in the form of a wedge. These wedges are then placed in the parallel plate region. The wedge creates an impedance match between the parallel plate region and the dielectrically loaded waveguide region. This is the recommended approach and experimental data on this transition design is presented in Chapter IV.

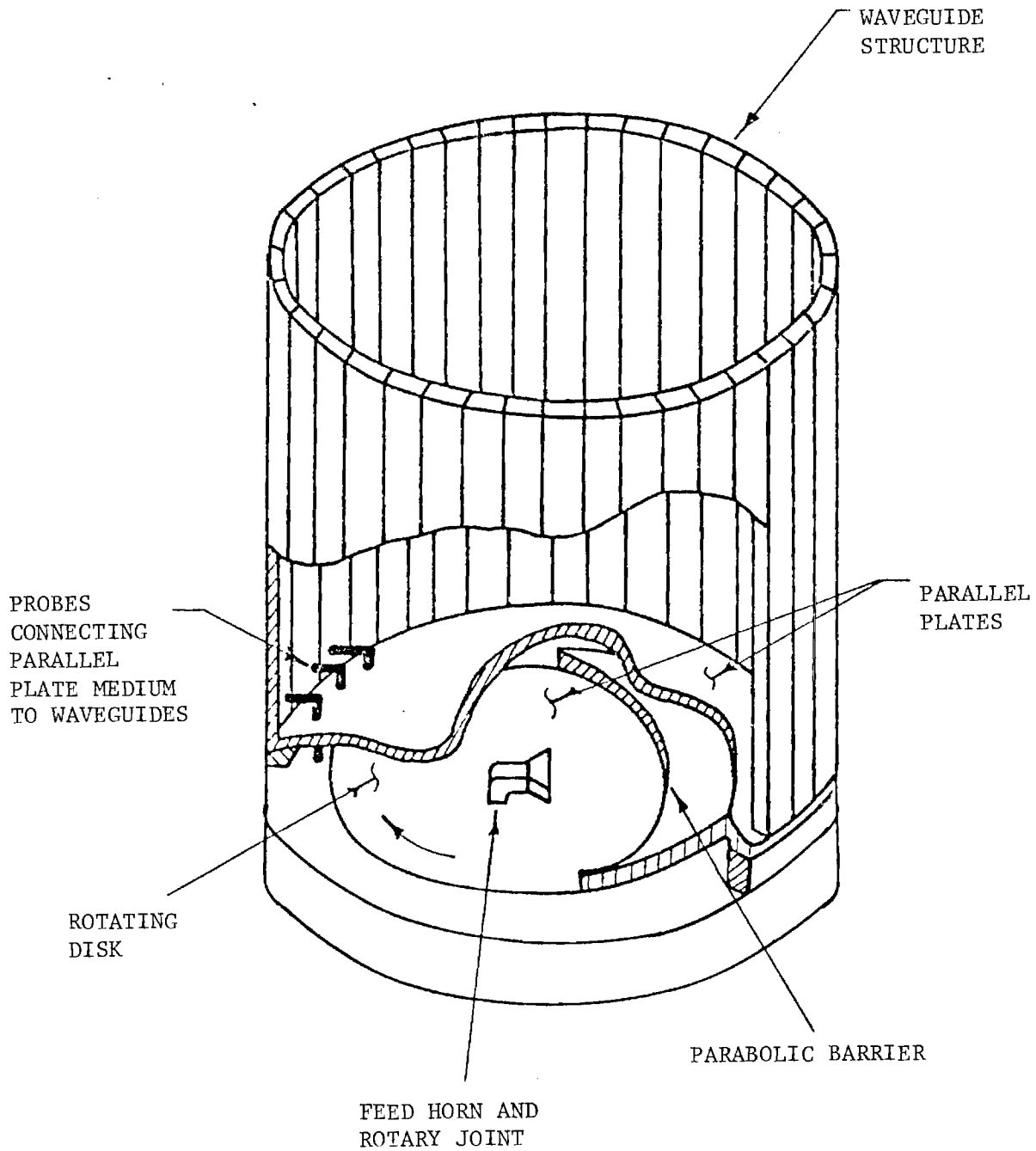


Figure 7. Basic Cylindrical Array Concept.

4. Weight

A preliminary mechanical design was performed for the antenna and a weight estimate made. The frequency of operation was X-band and Rexolite loaded Ku-band waveguide was assumed for the waveguide array elements. Since NOSC desired that the entire antenna weight be 100 pounds or less, various fabrication techniques were considered for reducing the weight of the array including chemical milling of the waveguide walls, electroless plating, photo etching and electrical discharge machining. If just the waveguide elements that form the cylindrical surface of the array are considered, then the weights shown in Table I are obtained. If standard 0.040 inch thick aluminum wall waveguide is used, then the weight of the waveguide elements alone is 96 lbs. (including the weight of the dielectric). If the waveguide walls are thinned to 0.020 inch by one of the above techniques, the weight is reduced to 70 lbs. Finally if the dielectric is simply plated with 0.005 inch thick copper, the weight is reduced to 67 pounds.

Thus, using the lightest fabrication technique for the radiating array structure and estimating the weight of the other components of the antenna gives a total weight for the antenna of 177 pounds as shown in Table II. Examination of the various design alternatives for reducing this weight suggested that only very expensive fabrication techniques would reduce this weight substantially.

The only feasible way to reduce the weight under the 100 pound design weight for the antenna was to change the frequency of operation so as to reduce the size of the antenna. Discussions with the sponsor suggested that Ku-band frequency operation would be an acceptable operating frequency range. Table I shows that the weight of the cylindrical portion of the array is reduced from 67 pounds to 23 pounds for the 0.005 inch copper plated dielectric when the operating frequency is changed from X to Ku-band. The overall weight of the antenna is reduced from 177 pounds to 78 pounds as seen in Table II. Thus, the most feasible way to keep the weight of the antenna under 100 pounds is to change the frequency of operation to Ku-band. Hence, for the remainder of the program, the frequency of operation was assumed to be in Ku-band. Figure 8 shows the estimated weight variation of the entire Ku-band antenna as a function of antenna diameter.

TABLE I
 WAVEGUIDE ARRAY WEIGHT COMPARISONS
 FOR ALTERNATE CONFIGURATION

	X-Band Ku Guide Array (WR62)	Ku-Band K Guide Array (WR42)
Std. 0.040" wall	96 lb.	35 lb.
Thinned to 0.020"	70 lb.	25 lb.
Plated 0.005" Cu	67 lb.	23 lb.

TABLE II
 WEIGHT BREAKDOWN FOR ALTERNATE OPERATING FREQUENCIES

	X-Band Operation <u>Ku Guide Array</u>	Ku-Band Operation <u>K Guide Array</u>
Waveguide Array	67 lb.	23 lb.
Housing	60 lb.	20 lb.
Drive System	25 lb.	25 lb.
Geodesic Feedhorn	<u>25 lb.</u>	<u>10 lb.</u>
Total	177 lb.	78 lb.

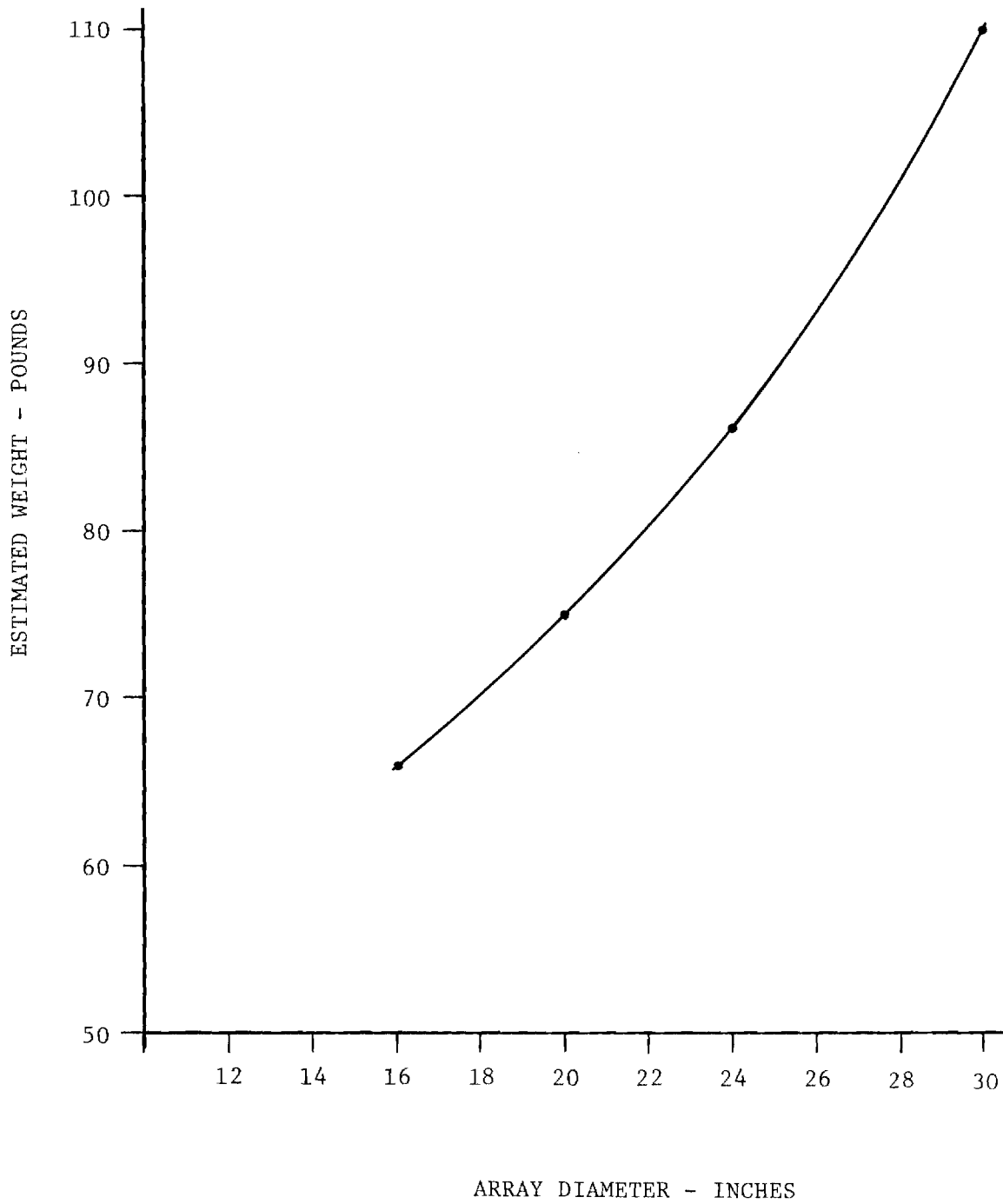


Figure 8. Estimated Weight Versus Antenna Diameter for Complete Ku-band, Cylindrical Array.

B. Description of Selected Antenna

The basic geometry of the cylindrical array configuration selected after the preceding considerations is shown in Figure 9. It consists of a primary feedhorn illuminating a geodesic lens which in turn illuminates the cylindrical array structure. Energy is coupled from the output of the parallel plate structure of the geodesic lens into the individual waveguides by means of dielectric wedges extending out from the waveguides. Energy is radiated from the waveguides to free space through broadwall slots cut in the rectangular waveguides. The antenna beam is scanned in azimuth by rotating the primary feed and the geodesic lens as a unit. Scanning in elevation is accomplished by changing the frequency of the transmitter. A traveling wave design is required for the radiating waveguides since frequency scanning (by changing the transmitter frequency) will be used to produce elevation scanning. A portion of the energy in the waveguide must be dissipated in a load at the top of each waveguide because a traveling wave array design is used. This can be accomplished either with a waveguide load or a coaxial load. Figure 9 shows a coaxial load since it produces a more compact structure. Table III lists the performance expected from the final antenna.

In Chapter II of this report the major components of the array are described in more detail. The results of a theoretical study on selecting the parameters for the radiating structure are presented in Chapter III, and experimental data on critical array components and on a partial mock-up of the final array are given in Chapter IV.

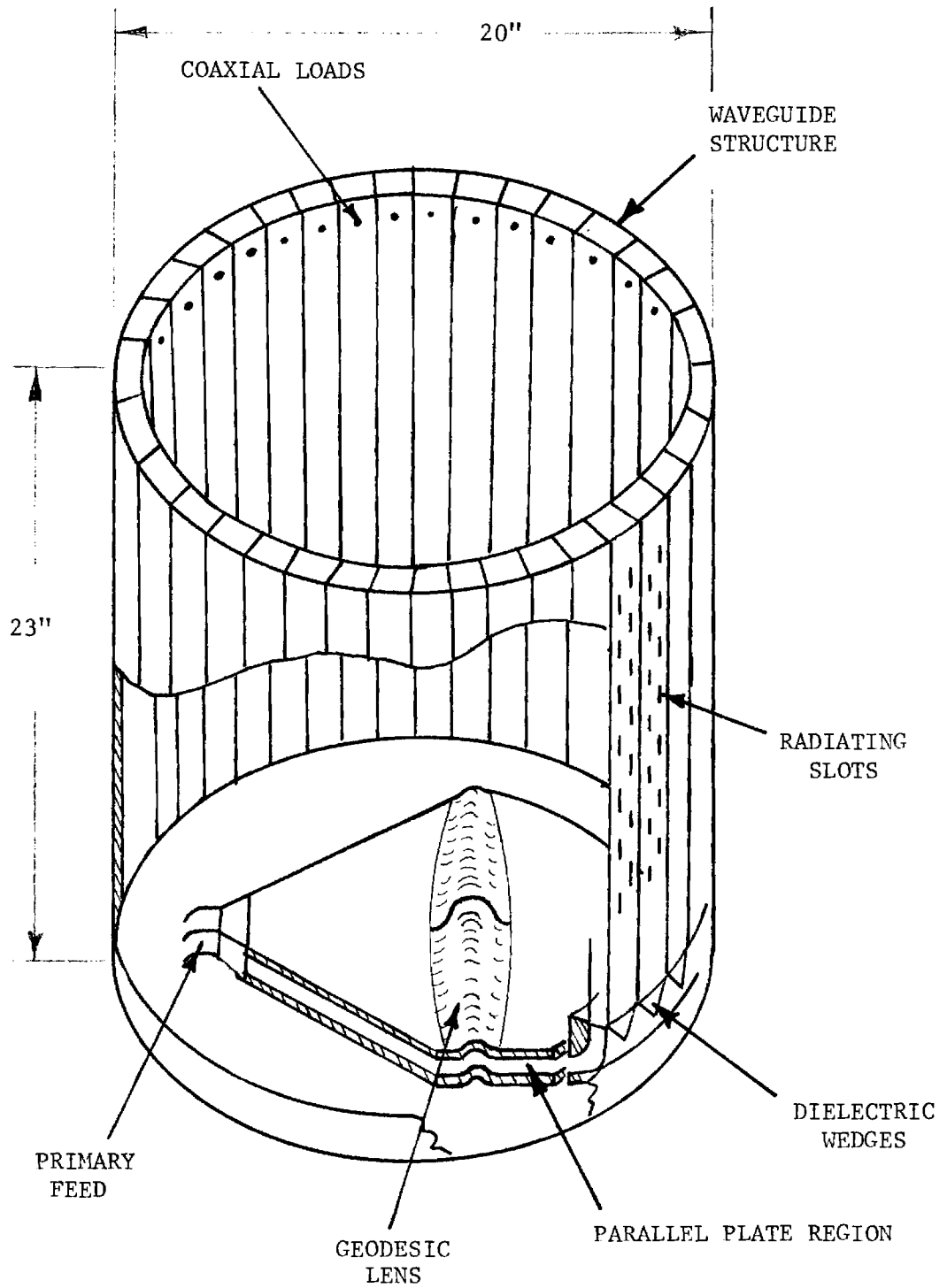


Figure 9. Illustration of Cylindrical Array Configuration.

Table III

Estimated Performance of

Complete Cylindrical Array Antenna

Frequency	16 GHz
Gain	33 dBi
Beamwidth	
Az	3°
El	3°
Sidelobes	
Az	22 dB
El	22 dB
Scan Sector	
Az	360°
El	3° to 6°
Az Scan Rate	6 rps max.
Freq. Change for El scan	700 MHz
Transmitter Power	100 KW max. peak
Tracking	
Az	Monopulse (or Beam Splitting)
El	Lobe Switching
Weight	100 lbs. max.

II. DESCRIPTION OF CYLINDRICAL ARRAY

A general illustration of the proposed cylindrical array is shown in Figures 9 - 11, and the reasons for selecting this geometry were given in Chapter I. The primary components that constitute this array are the following: a rotary joint, a primary feed, a geodesic lens collimator, dielectric wedge transitions, slotted waveguides, and coaxial loads. A dual-mode hybrid tee forms the primary feed for the antenna. It permits azimuth-plane monopulse sum and difference antenna patterns to be formed thus improving the azimuth accuracy of the system. A dual-channel rotary joint connects the two ports of the hybrid to the transmitter and receiver package which is located external to the antenna shown in Figure 10.

A general description of antenna operation from a transmit point of view is as follows. Energy from the feed enters a parallel plate structure in which a geodesic lens or fold is located. This lens converts the spherical wave from the hybrid into a plane wave. This plane wave travels through the remainder of the parallel plate region and is channelled through dielectric wedge transitions into the bottom of the dielectrically-loaded rectangular waveguides that make up the cylindrical surface. The radiating aperture of the antenna consists of the slots cut in the broadwall of the rectangular waveguides. Each waveguide is terminated at its upper end with a coaxial load.

The waveguide array and the dielectric wedges shown in Figure 10 and 11 are stationary. The parallel plates, geodesic horn, hybrid and the rotary joint all rotate as a unit. This rotation scans the antenna beam in azimuth. Elevation scanning of the beam is accomplished by changing the frequency of the transmitter. In Table III are listed the expected performance from the proposed antenna system; most of these specifications were established by NOSC.

In the following sections of this chapter, each of the major components of the antenna is described in more detail and problems associated with cylindrical array design are discussed. Experimental data on some of these items are given in Chapter IV while tradeoffs in the array parameters are discussed in Chapter III.

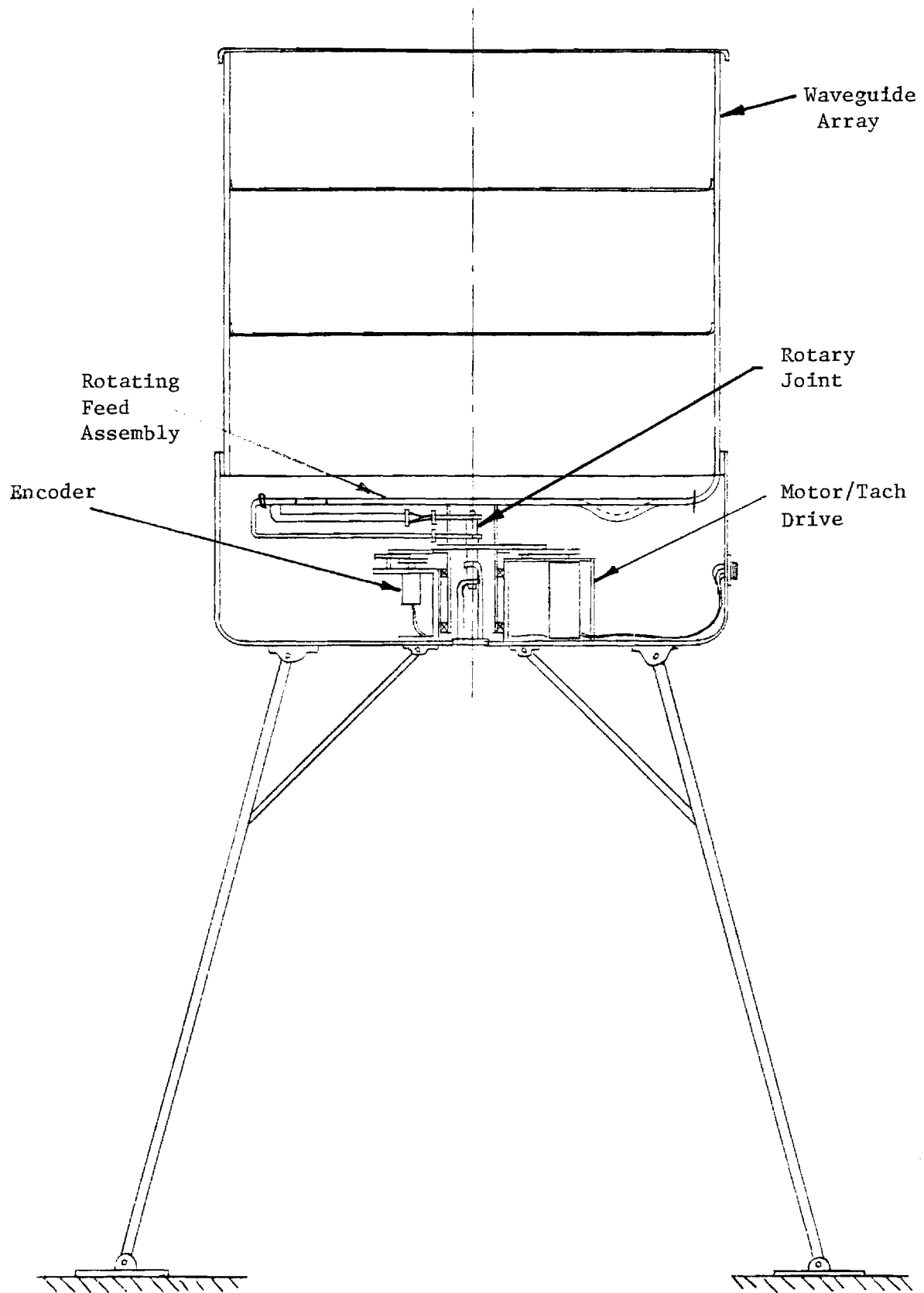


Figure 10. Conceptual Drawing of Waveguide Cylindrical Array.

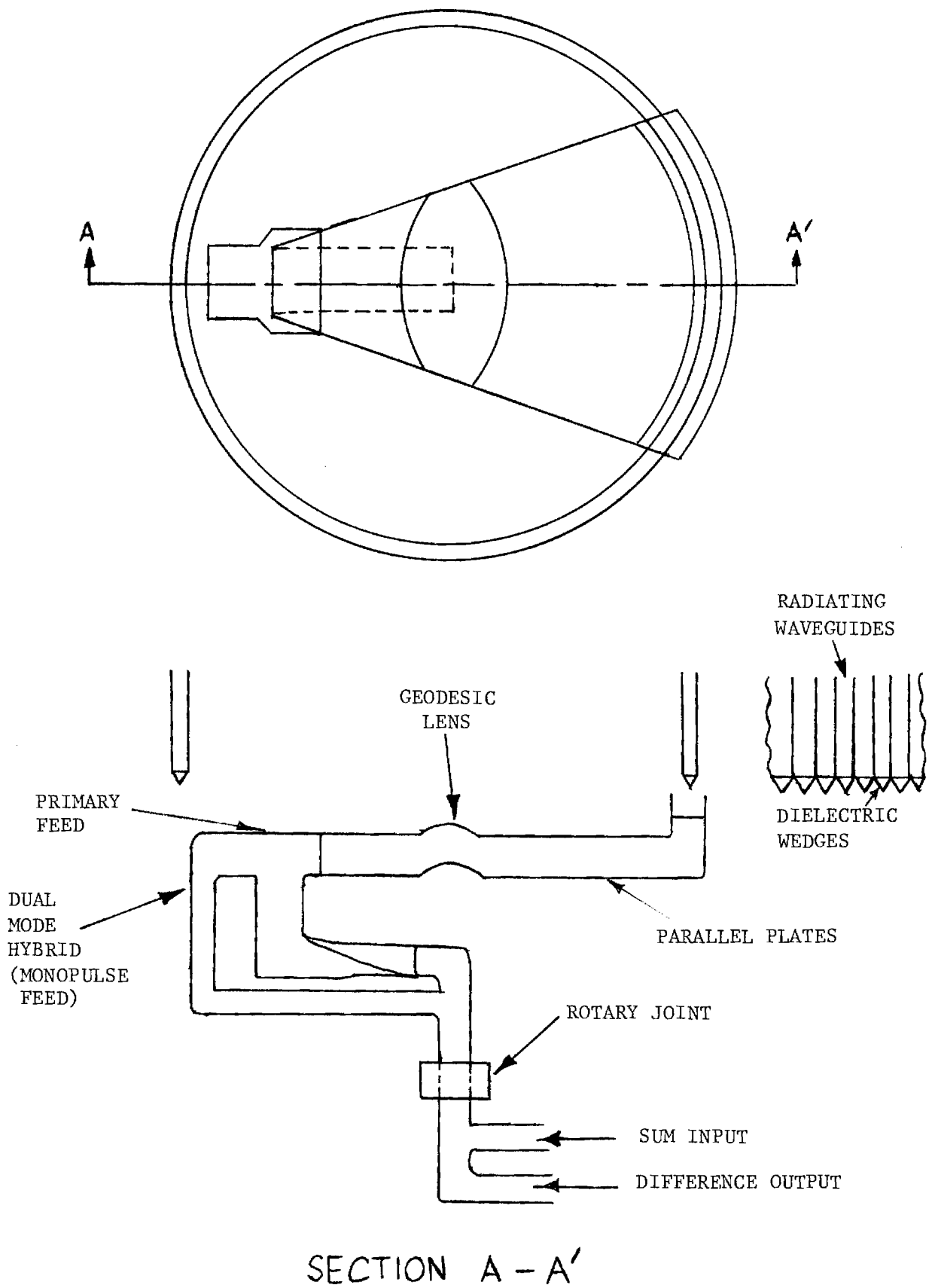


Figure 11. Antenna Feed System.

A. Rotary Joint

The rotary joint will be a dual-channel Ku-band joint specifically tuned for the frequency band of 16.3 to 16.9 GHz. It must handle full waveguide power while rotating at speeds up to 600 rpm. The two outputs of the rotary joint are connected by waveguide runs to an H-Plane Folded Hybrid Tee which forms the azimuth-plane monopulse sum and difference patterns.

B. Feed Horn and Azimuth-Plane Collimation

The H-Plane Folded Hybrid Tee feeds a flat, H-plane, sectoral horn as shown in Figure 12. The horn consists of parallel plates spaced 0.311 inches apart in the vertical plane and extending approximately 19.5 inches out from the tee. The side walls of the horn diverge from the center of the tee to the aperture at which they are approximately 16.5 inches apart. Located in the horn flare region is a geodesic fold (or lens) which will collimate the energy coming out of the sectoral horn. This type of lens has been built previously by EES and therefore poses no special problems in design or fabrication.

C. Transitions

The transfer of energy from the sectoral horn to each waveguide in the circular array is a significant problem. One method for accomplishing this transfer is with coaxial probes and cables. A set of coaxial probes could be equally spaced around the circumference of the parallel-plate structure which is fed by the rotating sectoral horn. The probes would couple energy from the sectoral horn into coaxial lines and then to another set of probes which would feed the waveguide array elements. Energy would thus be fed from the horn, through a probe in the parallel plates, into a coaxial cable, and then through a probe into the desired waveguide. This approach is conceptually simple but requires a large number of parts, all of which have to be carefully matched.

Another approach would be to couple the energy for the sectoral horn into each waveguide. Since each waveguide is filled with a dielectric, a transition could be made by extending the dielectric out of the bottom of each waveguide and into the parallel plate region of the

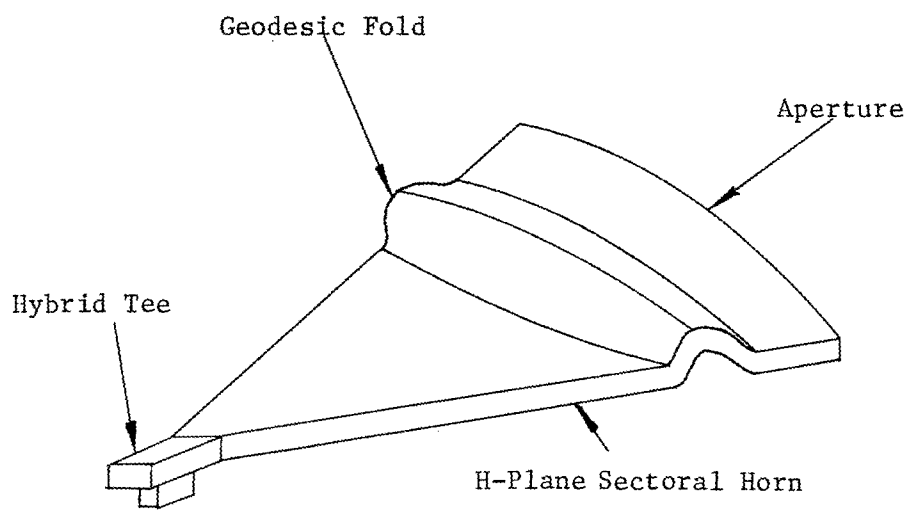


Figure 12. Feed Horn

sectoral horn (similar to a poly-rod antenna). The energy from the horn would then be coupled into the extended dielectric and thence into the waveguide. The primary problem with this method is that very little information about such a probe arrangement is available in the literature.

After considering both possibilities, the dielectric transition method was chosen to couple energy from the sectoral horn into the waveguides. These transitions should be simpler to design and fabricate in quantity and should result in a reduction in cost and weight.

D. Waveguide Arrays

Waveguide arrays can be either traveling or standing wave arrays. A traveling wave array is dictated for this application since frequency scanning will be used to move the antenna beam in elevation. As discussed in Section I, broadwall slots are required for this application. Wide slots should be used to improve the bandwidth of the antenna.

The waveguides must be dielectrically loaded in order to reduce their size and thus reduce grating lobes (see Chapter III). Special size waveguide can be extruded for the final array; however, it is more cost effective to use conventional size waveguide for the demonstration purposes of the study.

E. Termination

A small portion of the energy in the waveguide arrays must be dissipated in a load at the end of the waveguide (this is the case in all traveling wave arrays). This prevents a secondary beam from being formed due to reflection from the end of the waveguide. Two types of loads can be used: a waveguide load inside the waveguide itself or an external coaxial load connected by a coax-to-waveguide adapter to the waveguide. The waveguide load has the advantage of being made integrally with the waveguide while the coaxial load must be attached separately. Each requires a special design due to the dielectric loading used in the waveguide.

F. Characteristics of Cylindrical Arrays

A great deal of theoretical analysis and experimental study has been performed on planar array antennas. Some of this work can be directly applied to the study of cylindrical arrays; however, there are some special phenomena that must be considered in the design of cylindrical arrays that have no counterpart in planar array analysis. These special problems will be discussed in this section.

1. Element Pattern Nulls

As is the case with planar arrays, the radiation pattern of one element of the array operating in the array environment is the basic building block of the cylindrical array analysis (see Figure 13). If the pattern of an element in the array environment can be determined, all effects of mutual coupling and interference between elements are accounted for automatically. The shape of the element pattern is of particular importance in cylindrical arrays because, unlike the planar array case, each element of the cylindrical array contributes energy to a given far-field point from a different direction in its pattern. As an example, three elements of a cylindrical array and their element patterns are illustrated in Figure 14. Elements B and C of Figure 14 cannot contribute as effectively as element A to formation of a main beam in the direction shown since not as much energy is radiated in that direction from these elements. Therefore, if the far-field pattern of a cylindrical array is to be accurately determined, the element pattern for an element in that particular array environment must be accurately known.

Figure 15 shows the calculated element pattern of an isolated element on a conducting cylinder. This pattern radiates energy with essentially equal efficiency to angles up to $+70^\circ$ and would be ideally suited for use in cylindrical array. Unfortunately, the shape of the element pattern changes considerably when the element of this figure is placed in the array environment. Figure 16 shows the effect of the other elements in the array on the element pattern for three different values of element spacings. The characteristic features of these active element patterns are the deep nulls

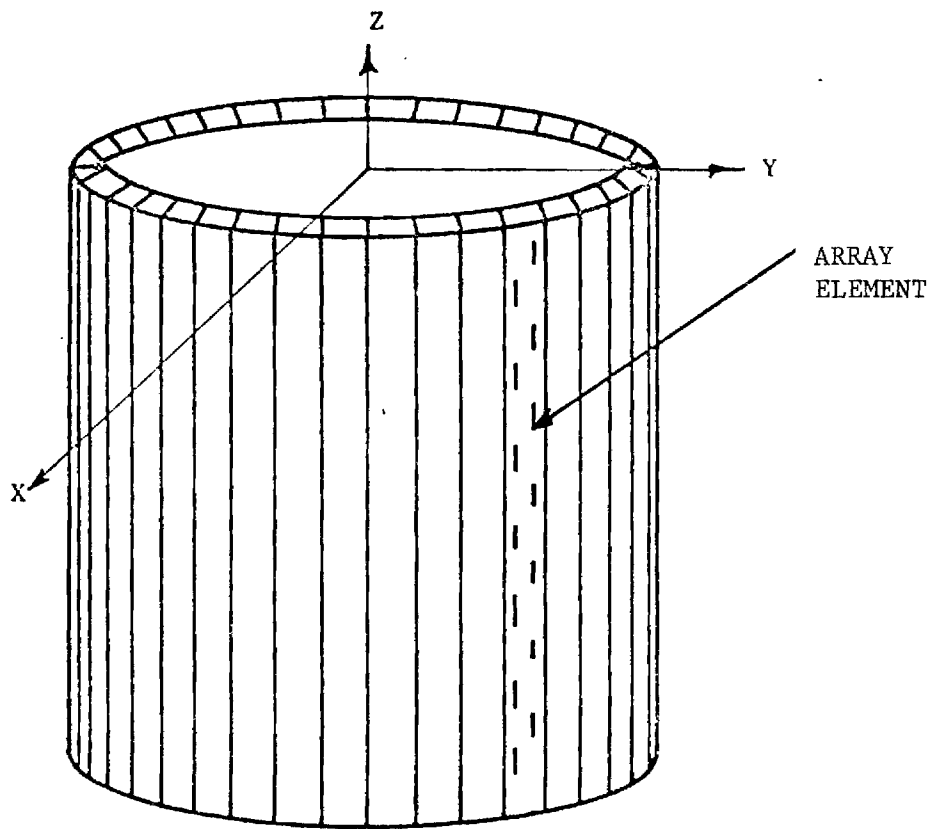


Figure 13. Cylindrical Waveguide Slot Array Antenna.

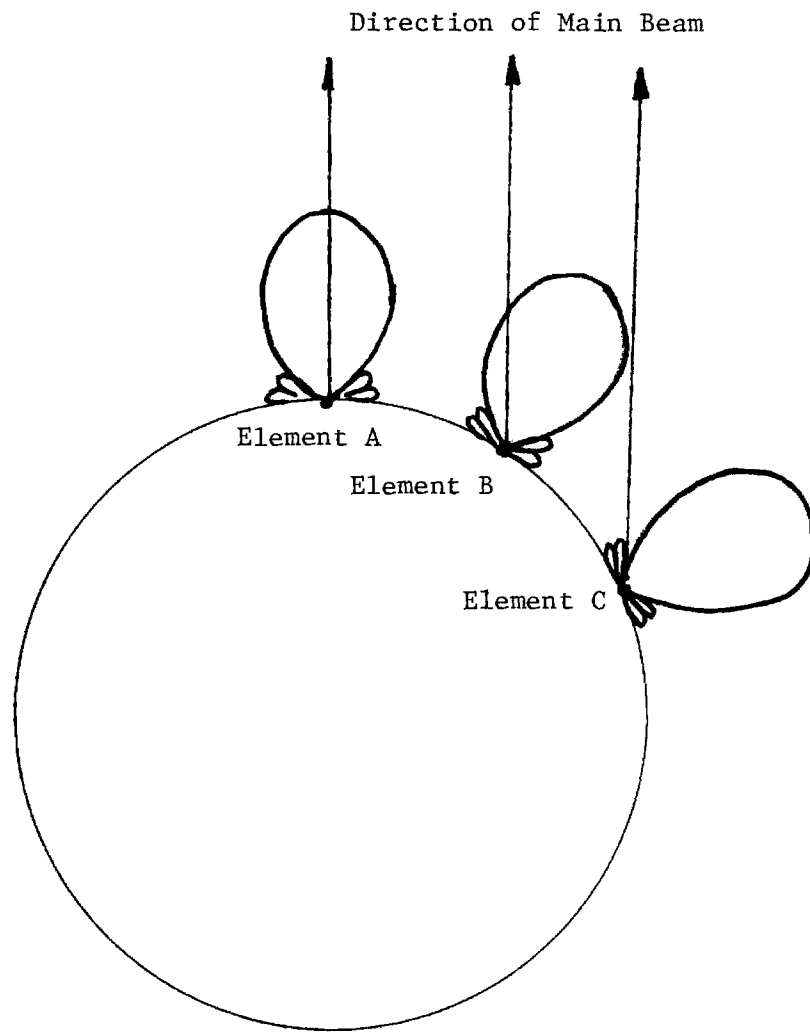


Figure 14. Illustration of Element Patterns on a Cylindrical Surface.

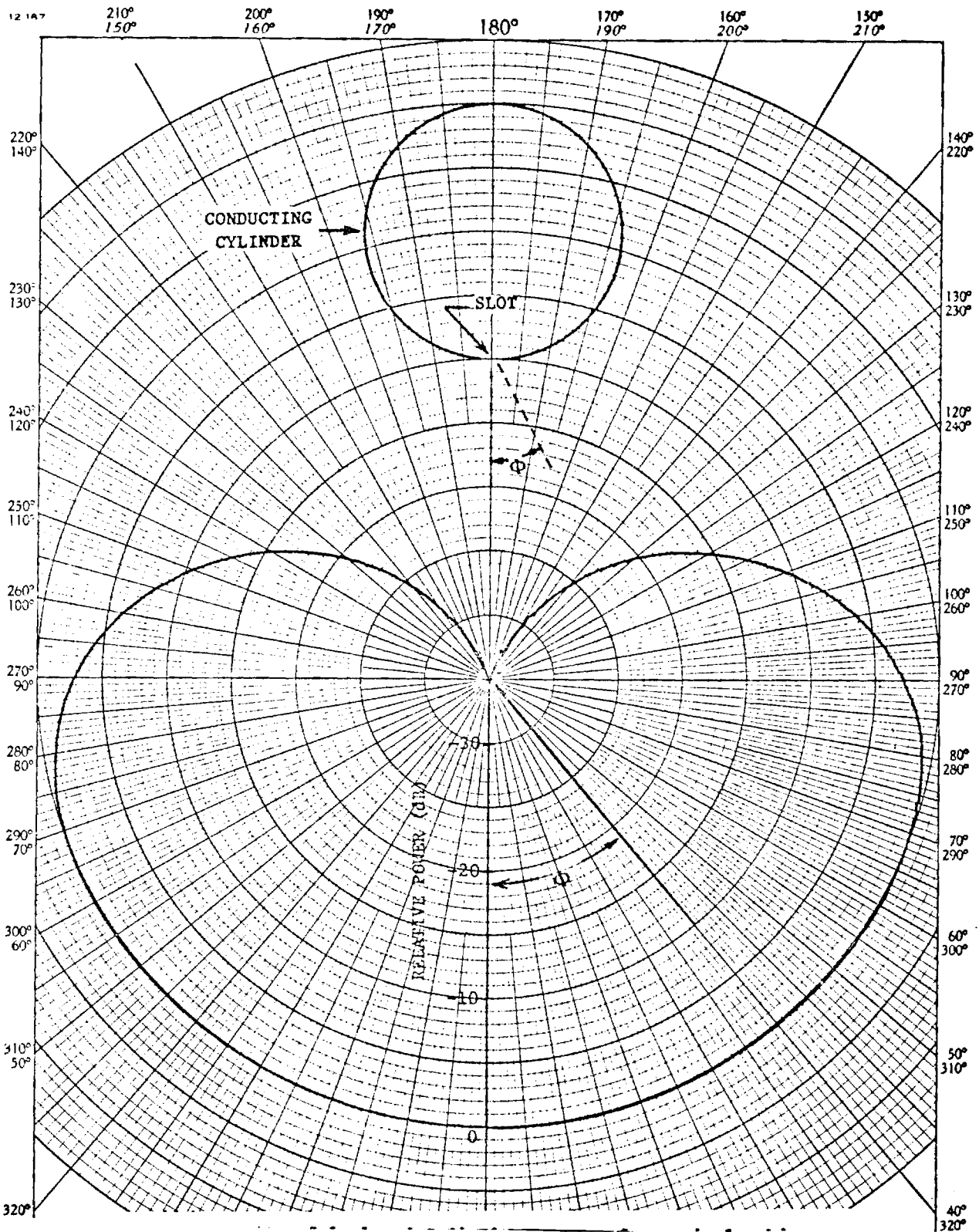
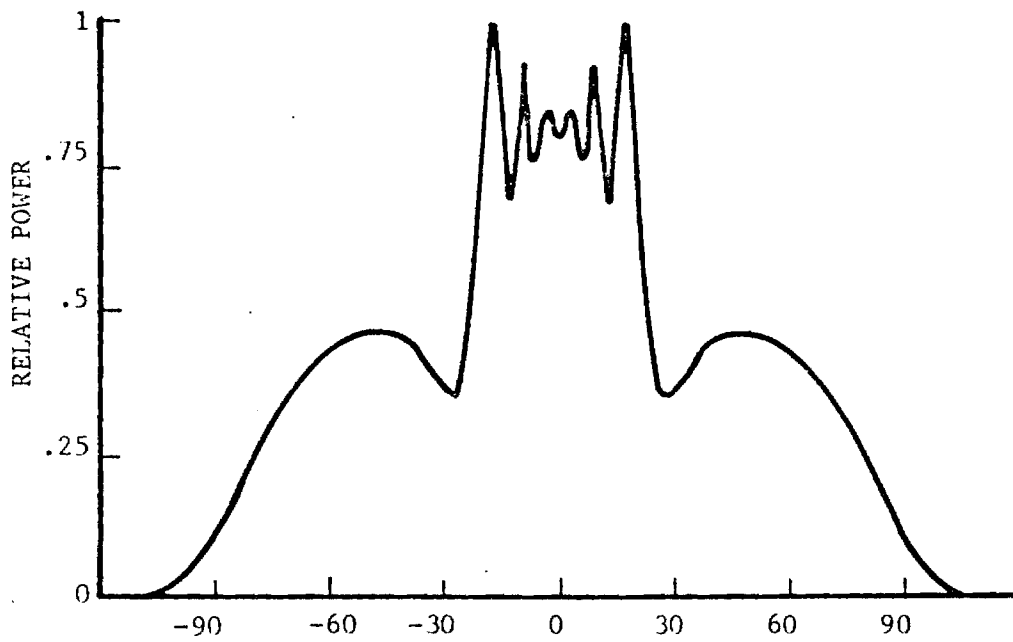
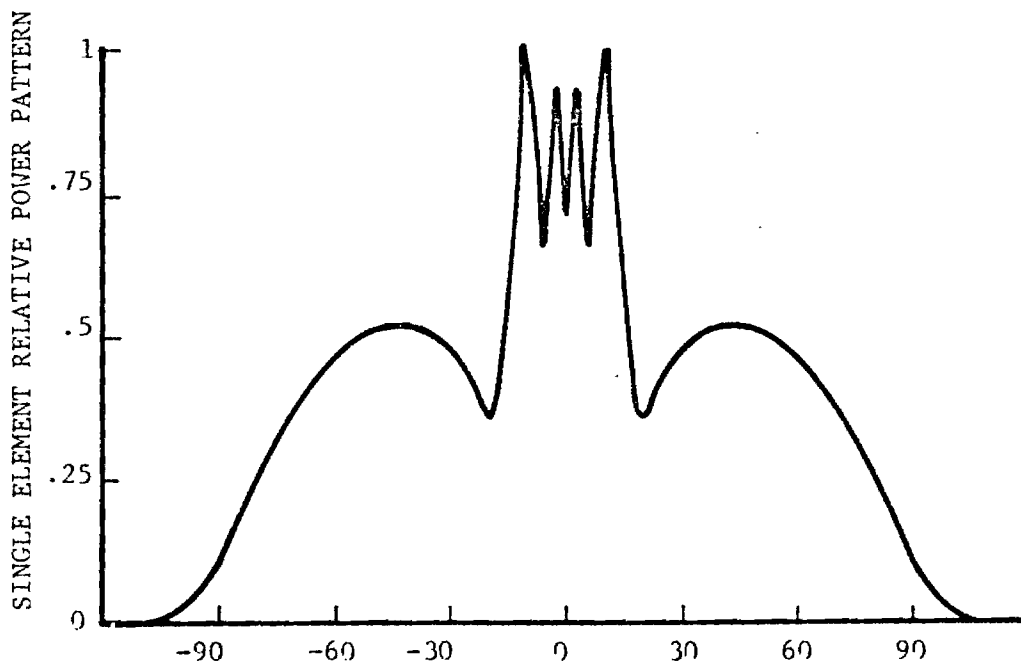


Figure 15. Calculated radiation pattern for a single thin axial slot in a 36-inch diameter perfectly conducting right circular cylinder.



(a) SLOT SPACING = 0.67λ



(b) SLOT SPACING = 0.73λ

Figure 16. Computed (by NELC) power patterns of a single energized element in an equally spaced array of slots on a conducting cylinder. Element spacings are indicated.

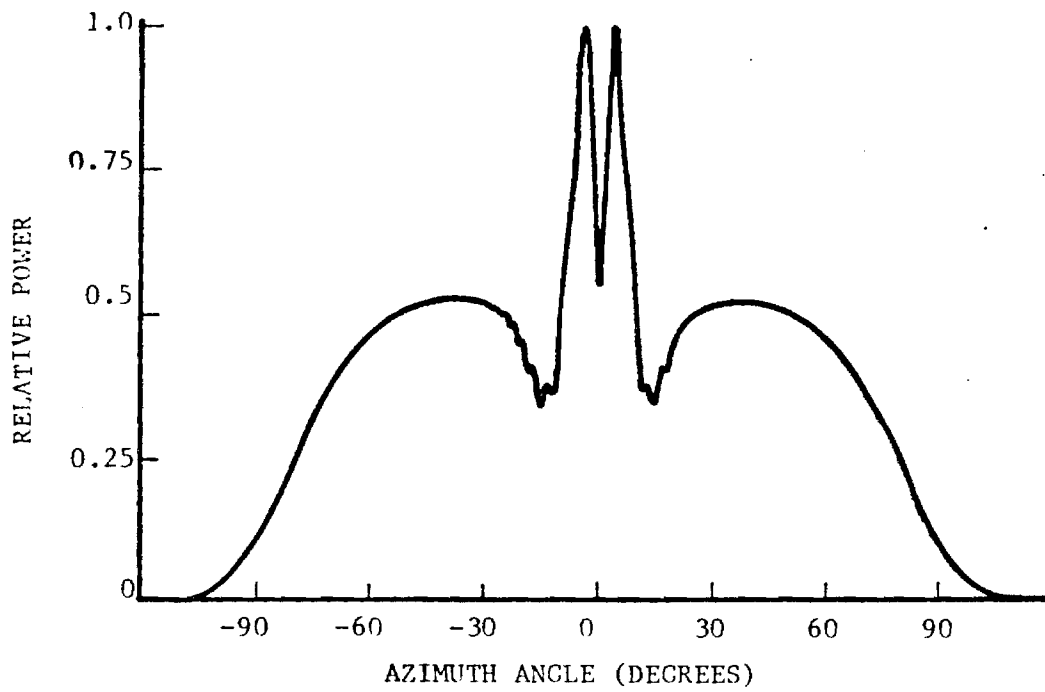


Figure 16. (c) SLOT SPACING = 0.79λ

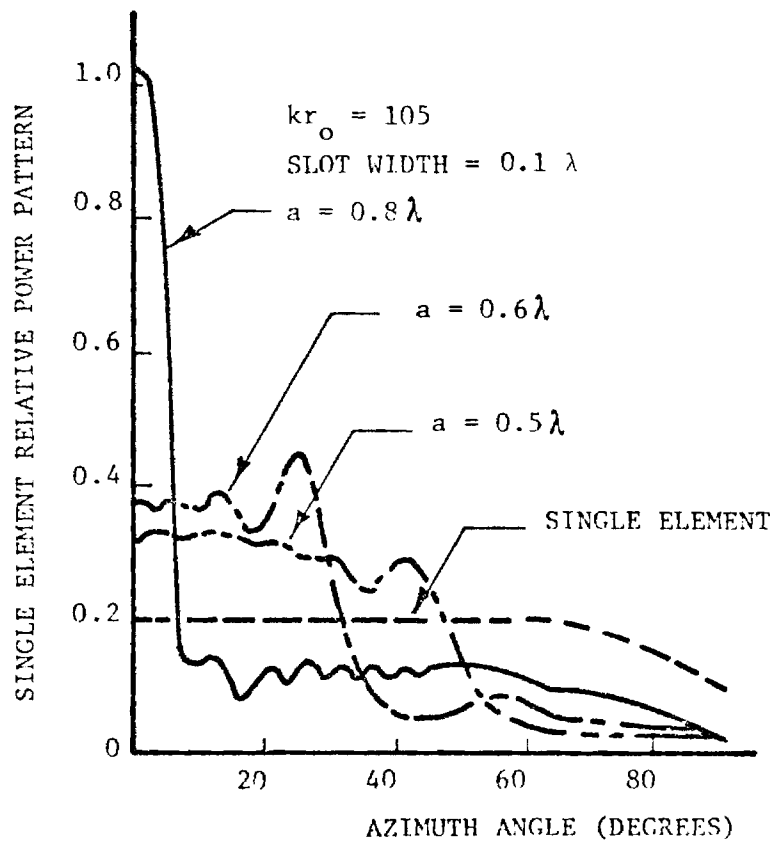


Figure 17. Comparison of computed (by NELC) element patterns for different slot spacings on a conducting cylinder.

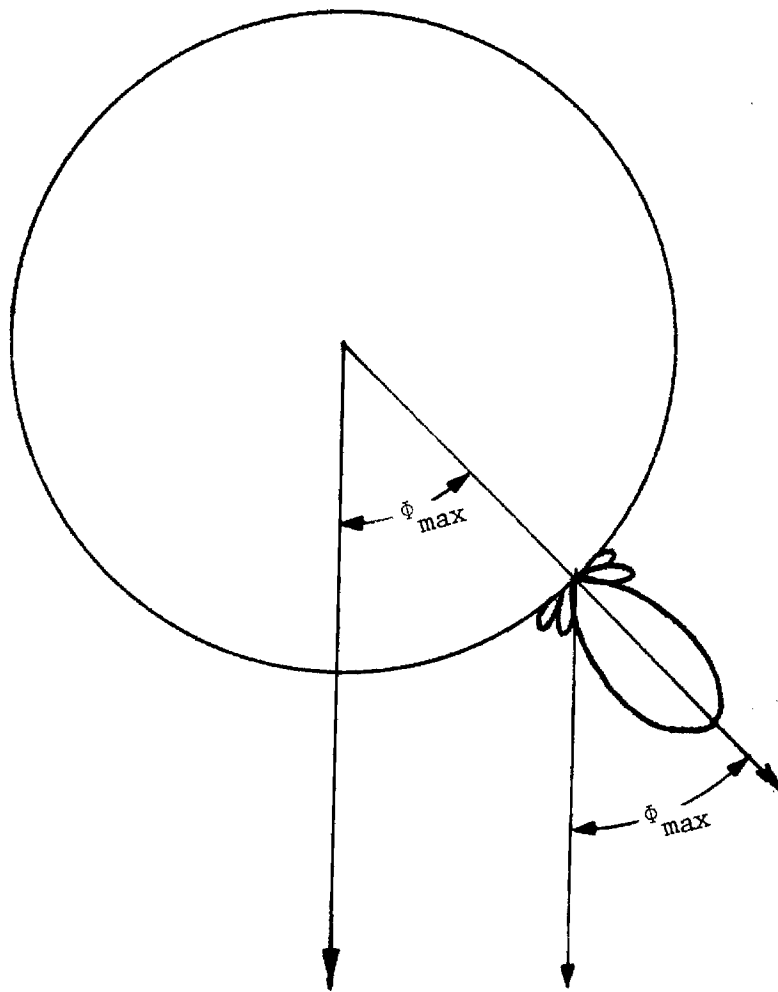
occurring between 20 and 30 degrees from boresight and ripples in the main beam area. It can be seen from Figure 17 that the location of the nulls moves toward the beam center as the element spacing is increased. Also, the depth of the ripples in the main beam area increases with increased element spacing.

The element pattern nulls are caused by the interference between the radiating fields from the elements of the array with those of a creeping wave that propagates around the cylinder and radiates energy in a direction tangent to the cylinder [3]. When periodically spaced elements are present on the cylinder, grating lobes that are created in the creeping wave interfere with the fields radiated from the elements. The element pattern nulls have a serious effect on the performance of the array. As seen from Figure 18 the nulls limit the portion of the cylinder that can be effectively used at any one time. Elements having nulls pointing in the direction of the main beam cannot contribute energy into the main beam area even if they are properly phased. Therefore, all the energy radiated by elements beyond ϕ_{\max} of Figure 18 go into forming undesirable sidelobes.

It was seen from Figure 17 that the location of the element pattern nulls can be controlled by the spacing between elements. It is very important in the design of a cylindrical array that the sector of the cylinder which is illuminated and the element spacing be chosen so that the maximum illumination angle ϕ_{\max} of Figure 18 is not exceeded.

2. Aperture Projection

Many techniques are available for determining the aperture size and amplitude distribution (taper) required to obtain a certain far-field pattern from an antenna. These techniques can be applied to cylindrical array antennas; however, the aperture with the desired size and taper is not on the surface of the cylinder, but is the aperture projected on a plane in front of the cylinder. Figure 19 illustrates the projected aperture from a cylindrical array.



Direction of Main Beam

Figure 18. Maximum Illumination Sector of Cylindrical Array Antenna.

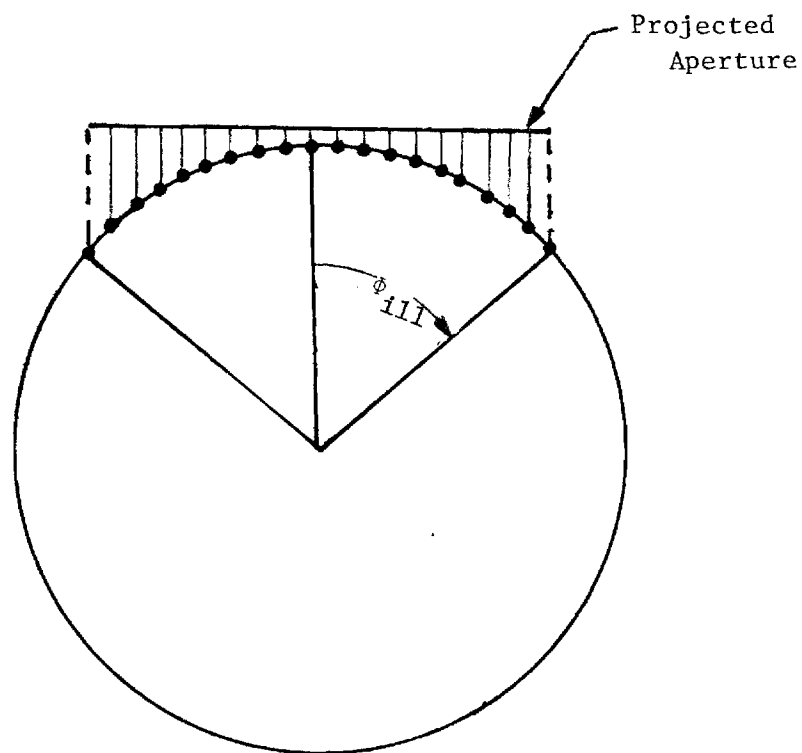


Figure 19. Projected Aperture from Cylindrical Array.

In designing a cylindrical array to have a particular beamwidth and sidelobe level, the following factors must be considered before the proper cylindrical aperture size and amplitude tapers can be determined:

- 1) A given area on the surface of a cylinder projects a smaller area on a planar surface.
- 2) A given amplitude taper on the surface of a cylinder does not map into the same taper on a plane.
- 3) Uniformly spaced elements on a cylinder do not project as uniformly spaced elements on a plane. The elements appear as if they are bunched toward the edges.
- 4) The shape of the element pattern affects the amplitude taper since each element radiates with a different efficiency in the direction of the main beam.

3. Grating Lobes

It has been observed both theoretically and experimentally that grating lobes can appear in cylindrical arrays if the proper relationship between the element spacing and illumination sector is not maintained. There are two causes for this phenomenon.

First, as was discussed in Section II-B, if the illumination sector is so large that elements are excited beyond ϕ_{\max} , the energy from these elements can only contribute to increasing the sidelobe levels.

Second, a grating load situation can occur as seen in Figure 20, due to the formation of locally planar array grating lobes. The elements near the edge of the array behave much like locally planar arrays. They must be phase scanned away from their local boresight to contribute to the main beam as shown. If the spacing between elements is greater than $.5 \lambda$, grating lobes in these locally planar arrays will occur when the steering angle becomes large enough (that is, when the illuminated sector is too large). These local grating lobes will contribute to the formation of high sidelobes at large angles in the array far-field pattern. Therefore, careful consideration of the maximum illumination sector and element spacing is required to prevent high grating lobes.

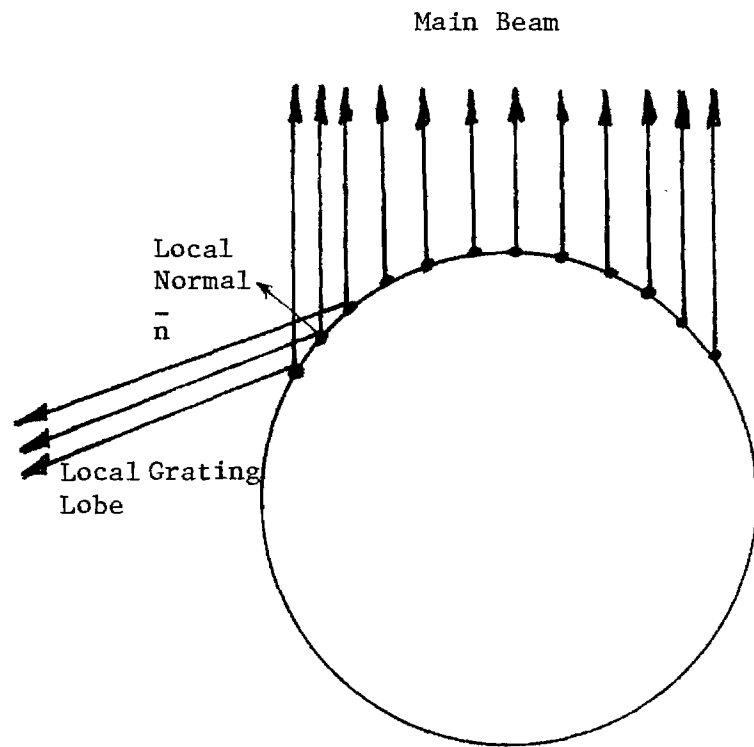


Figure 20. Local Grating Lobes on a Cylindrical Array.

4. Defocus of Main Beam with Elevation Steering

A planar phased array antenna can be scanned in elevation by changing the relative phase between adjacent rows of elements in the array. In contrast, to scan a cylindrical array antenna in elevation requires that both the relative phasing between adjacent rings of elements and the relative phase between individual elements on a ring to be changed (see Figure 21).

The feed system for the cylindrical array discussed in this report will be geodesic lens which has a fixed amplitude taper. The individual slotted waveguide arrays which constitute the cylindrical radiating structure will be designed to focus the main beam at one fixed elevation angle, θ_0 . If the beam is frequency scanned to another elevation angle, θ_1 , a phase error in the excitation of the elements will result. This is not a problem for small scan angles away from the boresight angle θ_0 . However, if the beam is scanned several beamwidths away from θ_0 , the main beam will become defocused because of the phase excitation error. A more complete analysis of this phenomenon can be found in the Appendix.

G. Design Procedure for Cylindrical Arrays

An investigation of cylindrical phased array antennas has revealed a number of interesting problems which must be considered (see Chapters II-A through II-F). These problems fall primarily into two categories: those amenable to experimental analysis and those amenable to theoretical analysis. Many of the problems discussed in Chapter II-A through II-B are more easily addressed from an experimental standpoint.

The problems discussed in Chapters II-A through II-E deal with the individual parts of the array. Consider for example the waveguide terminations. The assumption is made that the waveguides are perfectly matched resulting in no reflections from the termination. If this is to be true, the termination mismatch problem must be individually analyzed. The most direct approach in analyzing the problem is to build and test a termination and then vary its physical parameters until an acceptable match is achieved. Once this is accomplished, the termination can then be placed

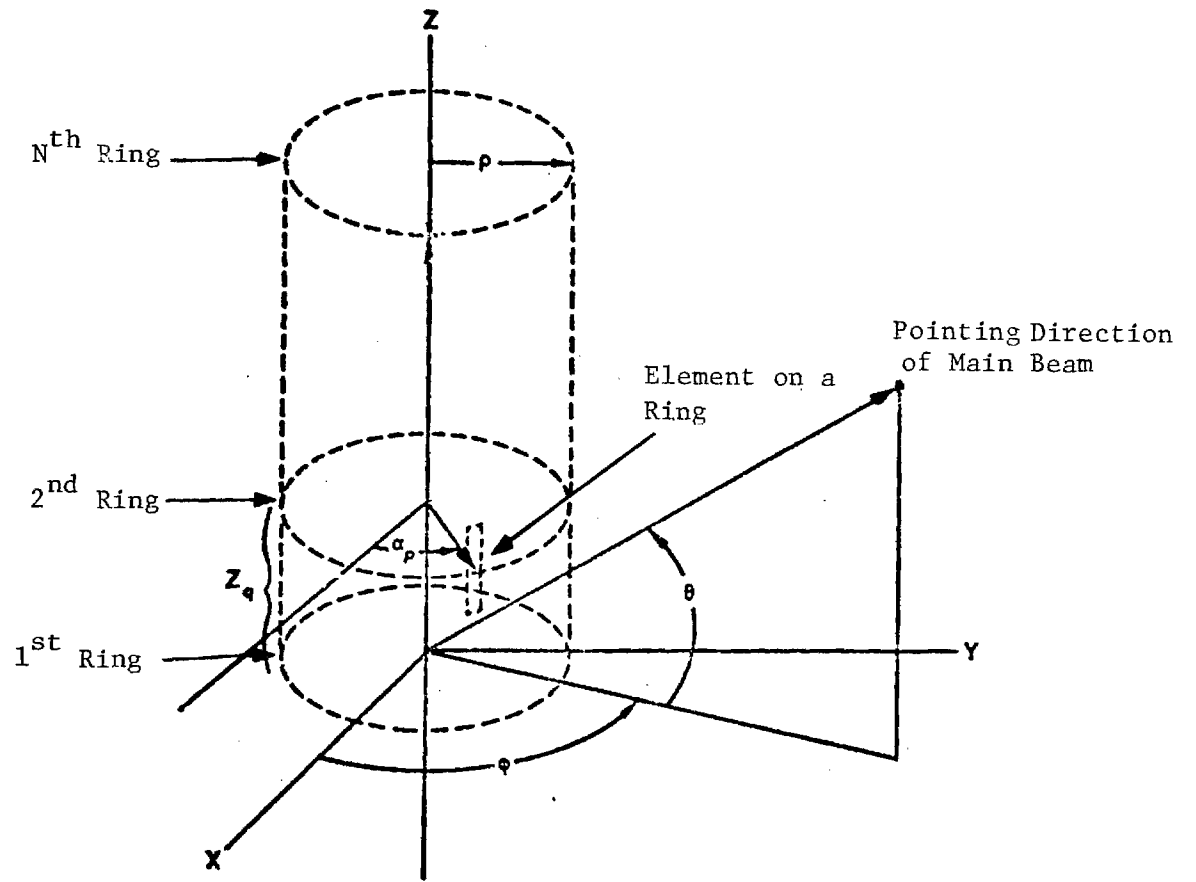


Figure 21. Coordinate System for Beam Steering of Main Beam.

into the overall array design as a functioning part of the system. Since many other parts of the array require similar experimental analysis techniques, a separate chapter has been included in which these problems are discussed and analyzed (see Chapter IV).

In Chapter II-F are discussed problems which are more easily addressed from a theoretical viewpoint. These problems deal with such things as the optimum number of elements, the radius of the cylindrical array, the taper of the excitations and the defocus of the main beam. The cost effective approach in analyzing these problems is by mathematical modeling. Each individual part of the array is modeled. Assumptions are made that each part of the array has been accurately designed and that it is functioning properly (i.e., transitions and termination are perfectly matched, waveguide lens and radiating slots are generating exact tapers, etc.). The individual models are then put together to form a complete mathematical model of the array. Since this model assumes ideal conditions, it must be calibrated. Figure 22 shows an outline of the design and calibration procedure which is used to calibrate the mathematical array model.

The first step of the design and calibration procedure shows theoretical data which is fed into the Mathematical Array Model. The input data includes the following: the total number of array elements; the location of each element; the excitation of each element; and the far-field pattern for a single element embedded in the array environment. The mathematical model processes the input data and produces a far-field pattern. By studying the far-field pattern as a function of variations in the input parameters, a set of design curves can be generated. The next step is to build a prototype of the partial array (Experimental Array Model) from the design curves. This simply entails putting the individual parts together to meet the mathematical design requirements. Once built, the prototype is then used to generate experimental far-field data to compare with the theoretical far-field data generated by the mathematical model. This comparison allows the mathematical model to be calibrated to increase its accuracy. With this complete, the mathematical model is then ready to be used as a tool in the final array design. Development of the Mathematical Array Model is discussed in Chapter III.

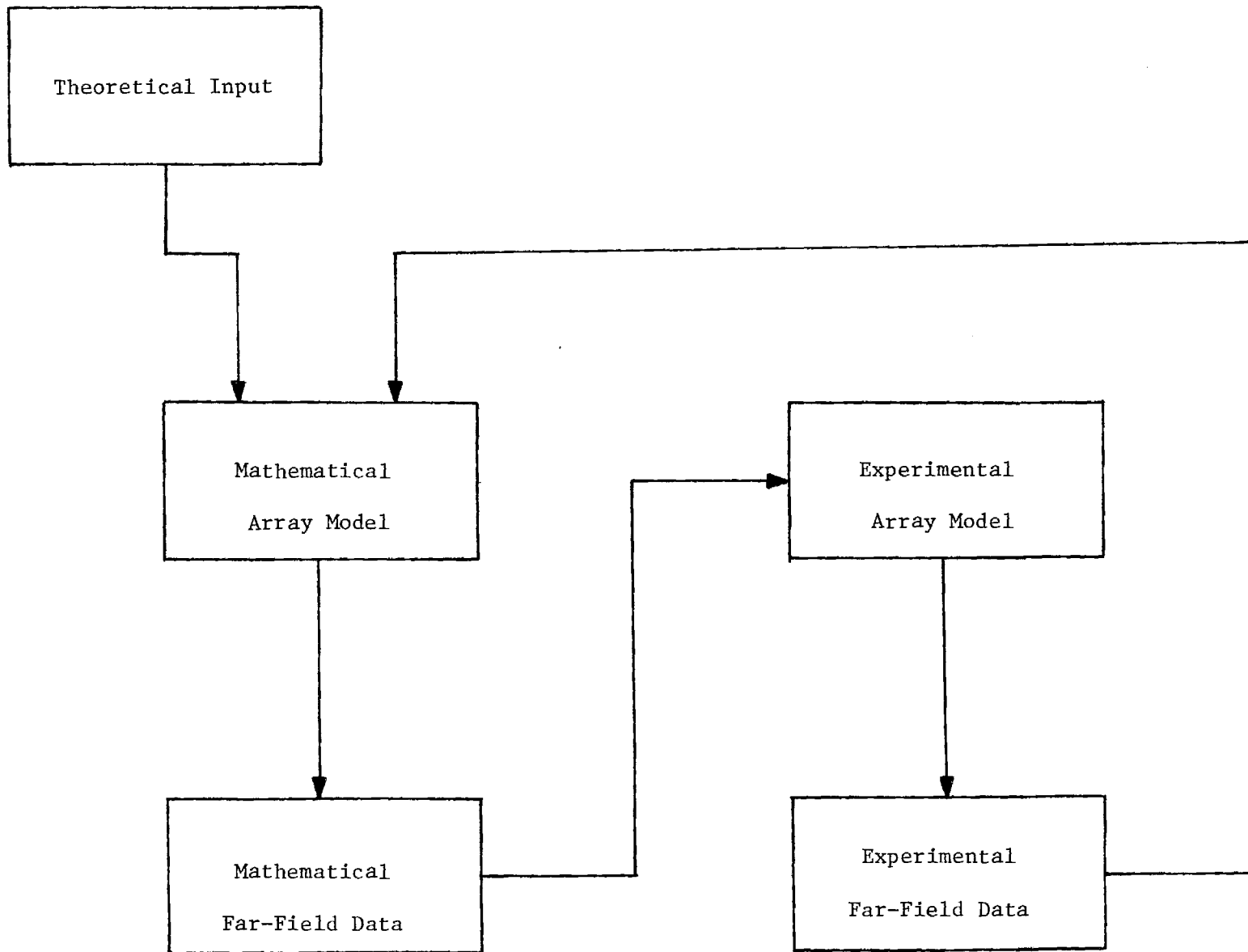


Figure 22. Outline of Mathematical Model Calibration Procedure.

III. MATHEMATICAL ARRAY MODEL

The design procedure of Chapter II requires an array model which is capable of accepting either theoretical or experimental input data. The model must then process the input data to produce a far-field pattern. In this chapter the mathematical model is described and then is used to study the problems discussed in Chapter II.

A. Description of Mathematical Array Model

The block diagram of Figure 23 shows a mathematical array model with three inputs and one output. Two of the inputs - the element locations and element excitations - are determined from specifications imposed on such parameters as the steering angle, beamwidth, sidelobe level, and grating lobe level. In order to study changes in the latter parameters, both the element locations and element excitations must be varied. To vary the element location entails only changing the element spacing in either the azimuth or elevation direction (or both). Varying the element excitation requires changing the excitation taper (linear, cos, \cos^2 , etc.). Both of these inputs are simple to change. The third input is the far-field pattern of a single element embedded in the array environment. This input is not as simple to change and, therefore, will be investigated in more detail in the next section.

1. Element Pattern Model

As discussed in Chapter II, the radiation pattern of an element in a large cylindrical array is very different from that of an isolated element on a conducting cylinder. The pattern varies as a function of the spacing between elements, radius of the cylinder, and operating wavelength. To develop an accurate model of the complete array it is necessary to be able to determine accurately the radiation pattern of an individual element.

Two techniques are available in the literature to model element patterns in cylindrical arrays. One model uses an eigenpattern expansion technique developed by Borgiotti [4]. Another model uses a phase sequence excitation technique developed by Sureau [5]. Both models predict the same element patterns. The Sureau model provides more physical insight into the various phenomena causing the variation in the element patterns. However, the Borgiotti model could be more directly adapted to the problem

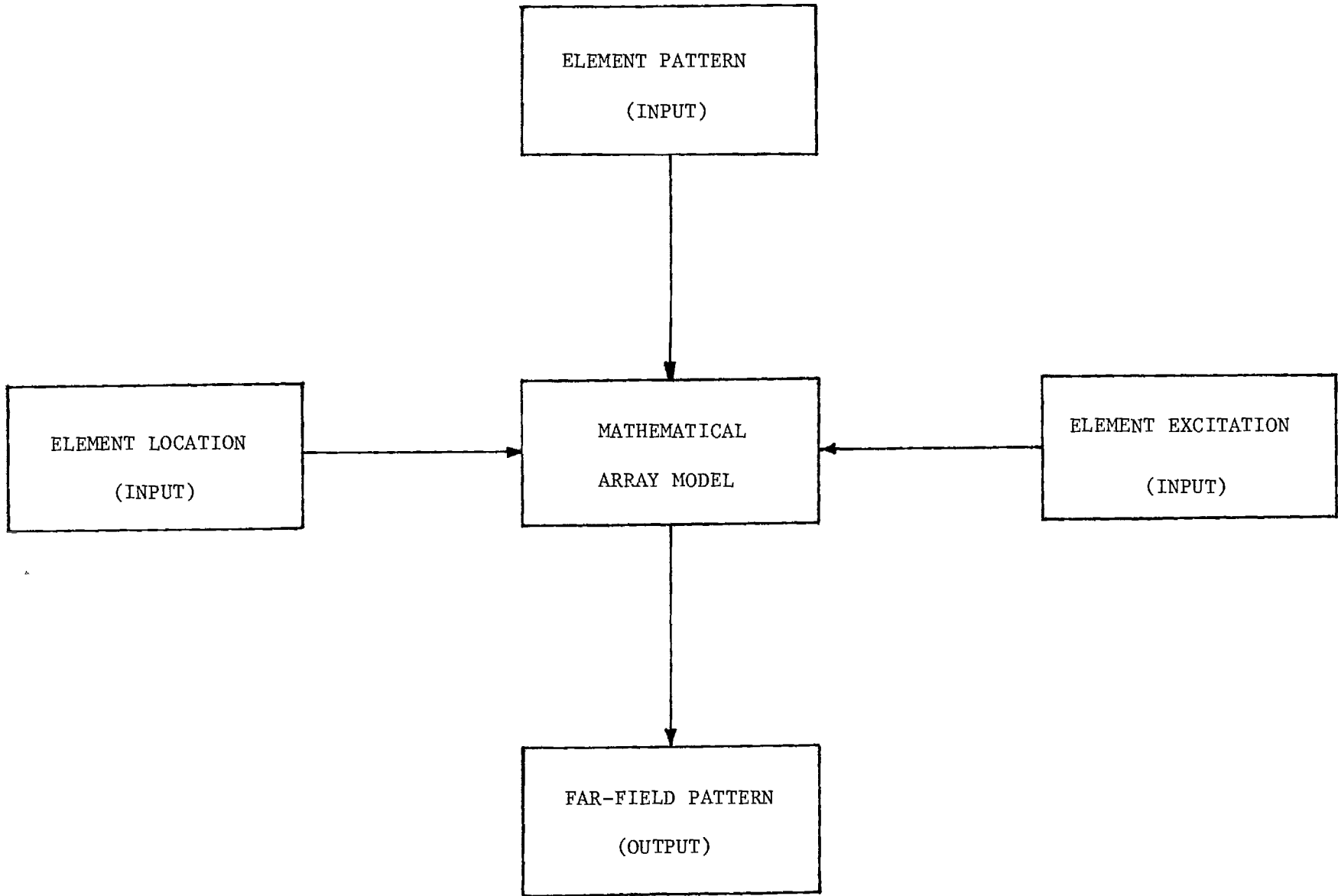


Figure 23. Block Diagram of Mathematical Array Model.

of interest in this study and was easier to implement on the computer. Therefore, the Borgiotti model was chosen for the study. A brief discussion of the Borgiotti model will now be presented. The reader interested in a detailed description of this model is referred to Reference [4].

A ring of equally spaced elements around a cylinder forms a periodic structure in the ϕ direction with period 2π (see Figure 24). Because of the periodicity, the mutual admittance between any two elements on this ring depends only on the angular distance between elements and not their locations. Therefore, the admittance matrix for these elements is symmetric and circulant, i.e., every column of the matrix is obtained from the previous one through a cyclic permutation. These special properties of the admittance matrix make it easy to determine the corresponding eigenvectors and eigenvalues.

The eigenvectors of the admittance matrix are used as a set of basic excitation vectors from which any arbitrary array excitation can be expanded. The eigenvalue corresponding to each eigen excitation is then the active admittance of each element of the array for that eigen excitation. The far-field radiation pattern corresponding to each eigen excitation is called an eigen pattern. The far-field pattern for any excitation of the array elements can be determined by first expanding that excitation into the eigenvector space to determine the coefficients of the eigen excitation expansion and then superimposing the eigen patterns, weighing each one by the coefficient of the eigen excitation expansion. To determine the element pattern of one element in the array environment, the eigen excitation expansion is done for the case where the element excitation is zero for all elements of the array except for one element which has an excitation of one. The superposition for eigen patterns is carried out as before to determine the total element pattern.

2. Model of Complete Cylindrical Array

Figure 25 is a drawing of a cylindrical array structure. Note that each array element has its own unique physical location, element excitation,

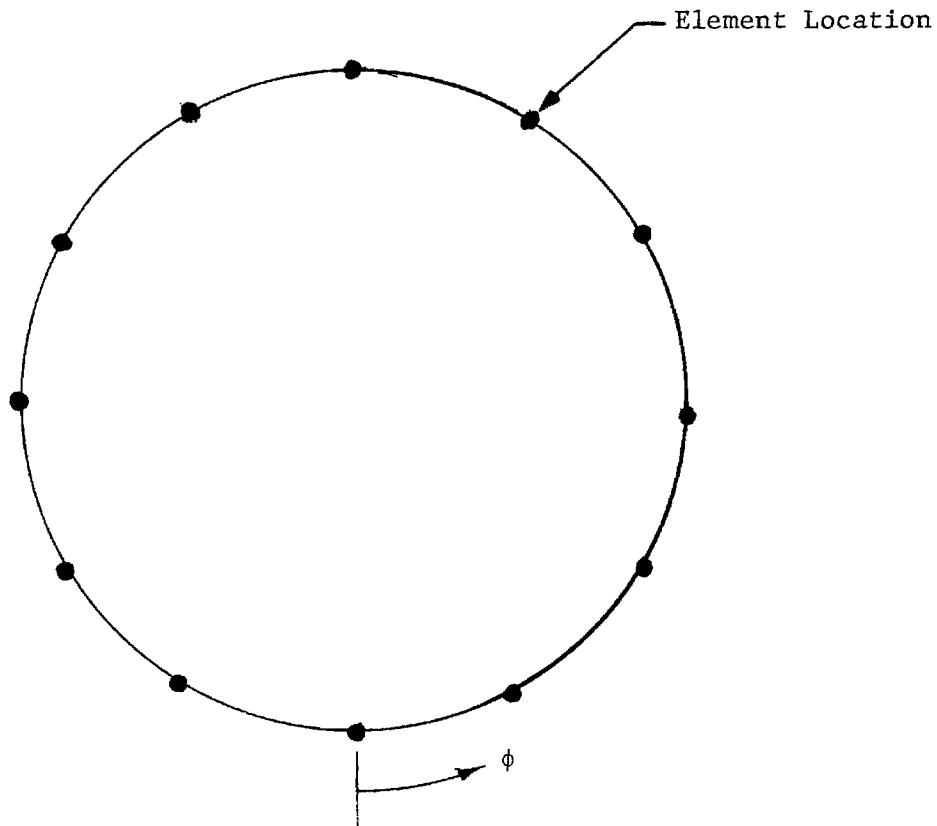


Figure 24. Ring of Equally Spaced Elements.

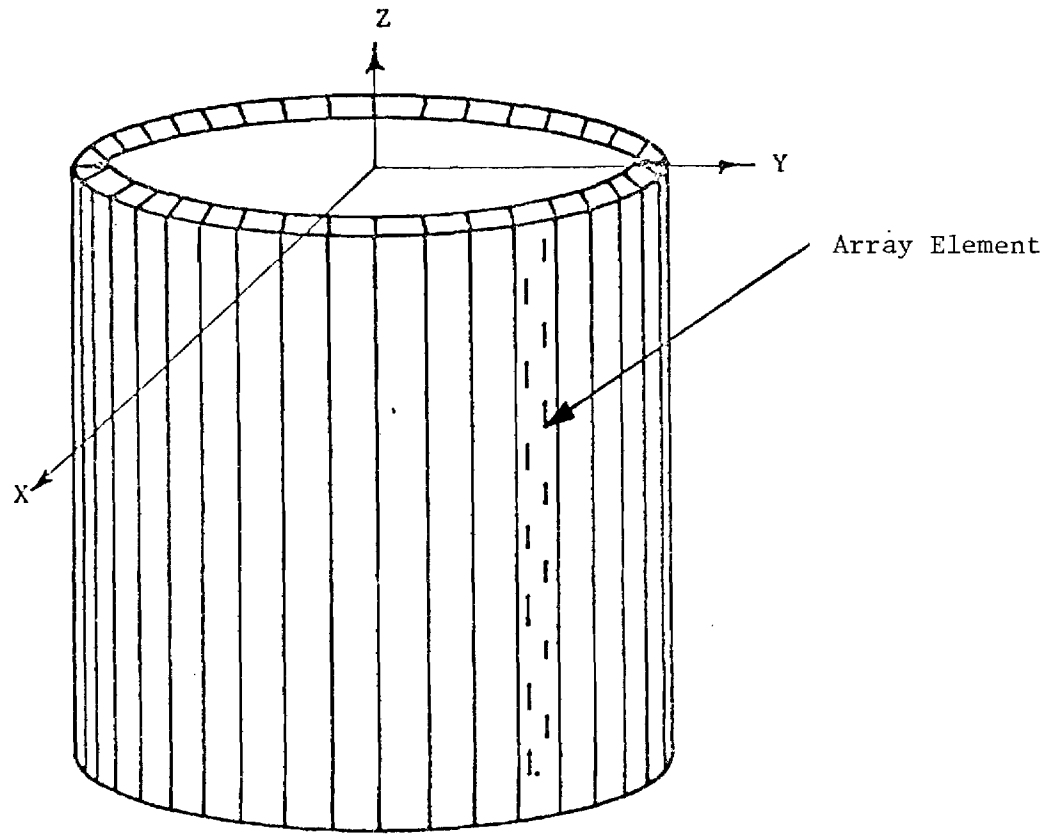


Figure 25. Diagram of Cylindrical Array Structure.

and far-field element pattern. Figure 26 shows a single element located at the origin of a coordinate system. To determine the far-field pattern, the angle ϕ is determined and the value of the element pattern read directly from the pattern. However, for the structure of Figure 27, the problem is not as straightforward.

Figure 27 shows an element located on the surface of a cylinder. In order to determine the far field at point P due to the element, the angle ϕ must be determined (note that $\phi \neq \phi'$). Should another element be added to the cylinder, the field at point P would be the sum of the individual fields generated by the two elements. The angle from the second element to point P is defined as ϕ'' . Since $\phi \neq \phi' \neq \phi''$, it becomes apparent that the superposition of each element field defined in its own coordinate system is non-trivial. As the number of elements increase, so will the complexity of the problem. Therefore, in order to reduce this complexity, each element will be referred to a reference coordinate system located at the center of the cylinder.

Figure 28 shows the n^{th} element and the reference coordinate system. The field at point P due to N elements can be expressed as

$$F(\theta, \phi) = \sum_{n=1}^N A_n E(\theta'_n, \phi'_n) \quad (1)$$

where

- (θ, ϕ) = the spherical coordinate location of P in terms of the reference coordinate system
- (θ'_n, ϕ'_n) = the location of P in terms of the coordinate system of n^{th} element
- $E(\theta'_n, \phi'_n)$ = the field pattern for the n^{th} element in terms of n^{th} element coordinate system
- A_n = the excitation coefficient for the n^{th} element.

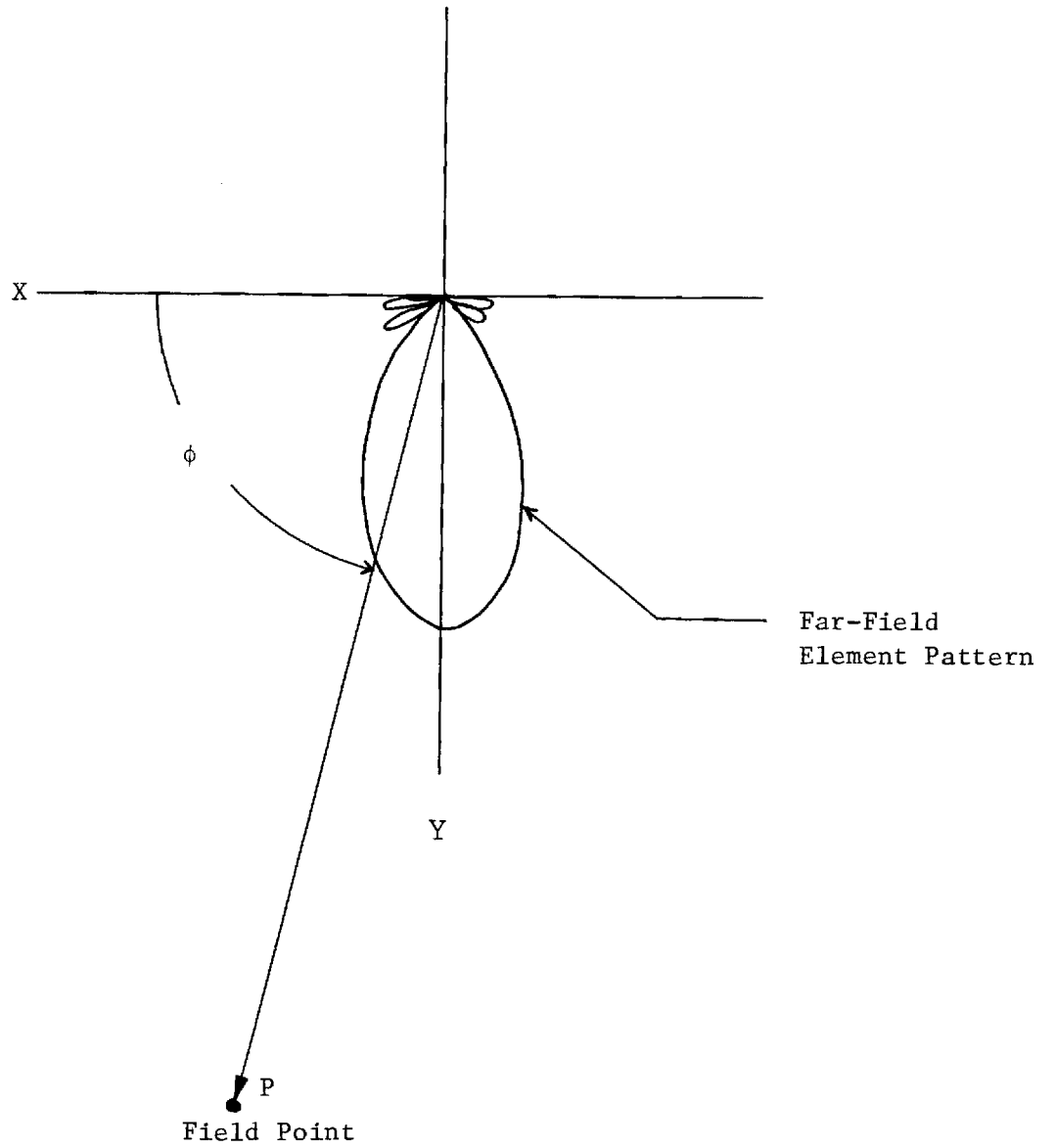


Figure 26. Diagram of the Far-Field Pattern of an Array Element With the Element Located at the Origin of a Coordinate System.

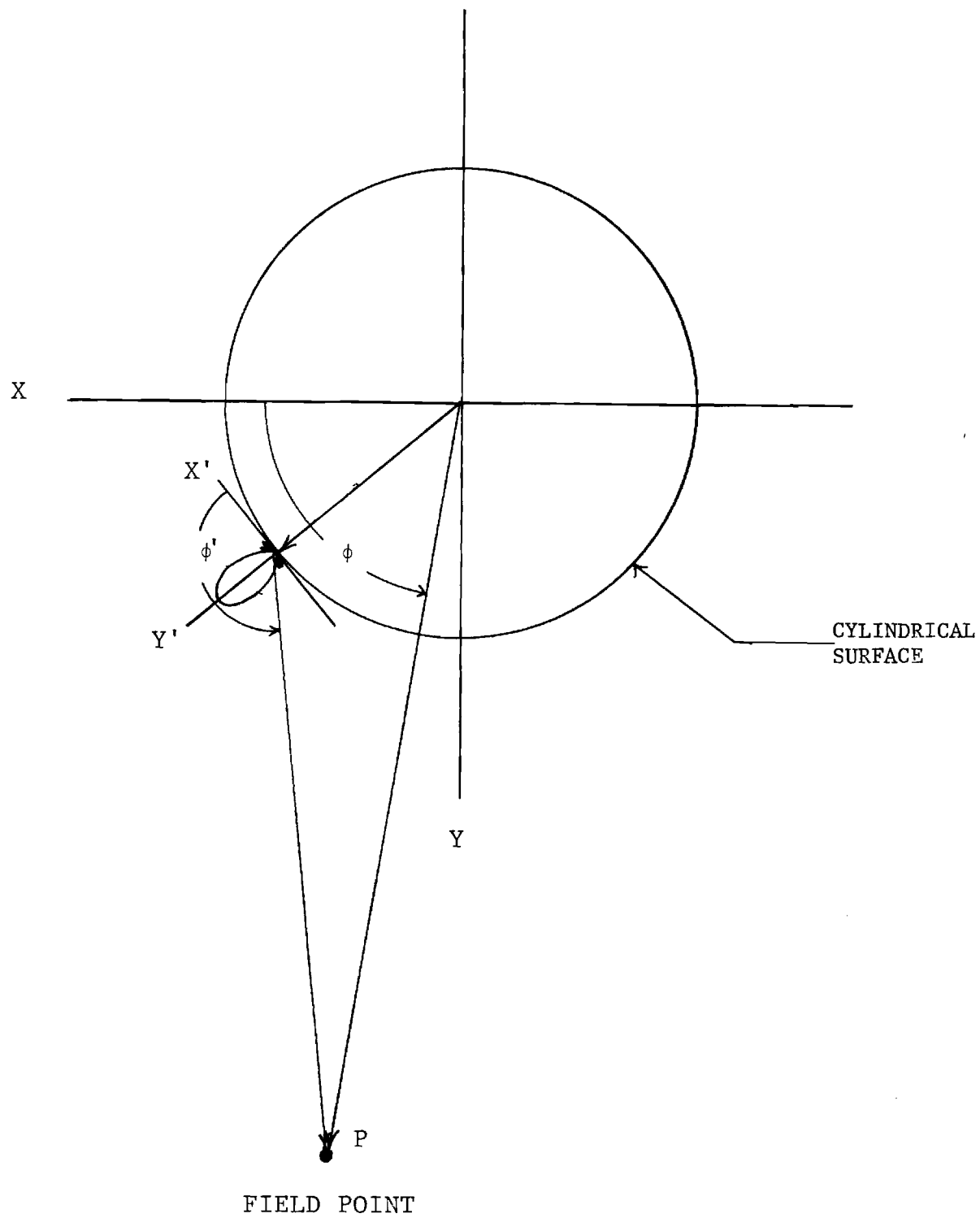


Figure 27. Diagram of the Far-Field Pattern of an Array Element With the Element Located on a Cylindrical Surface.

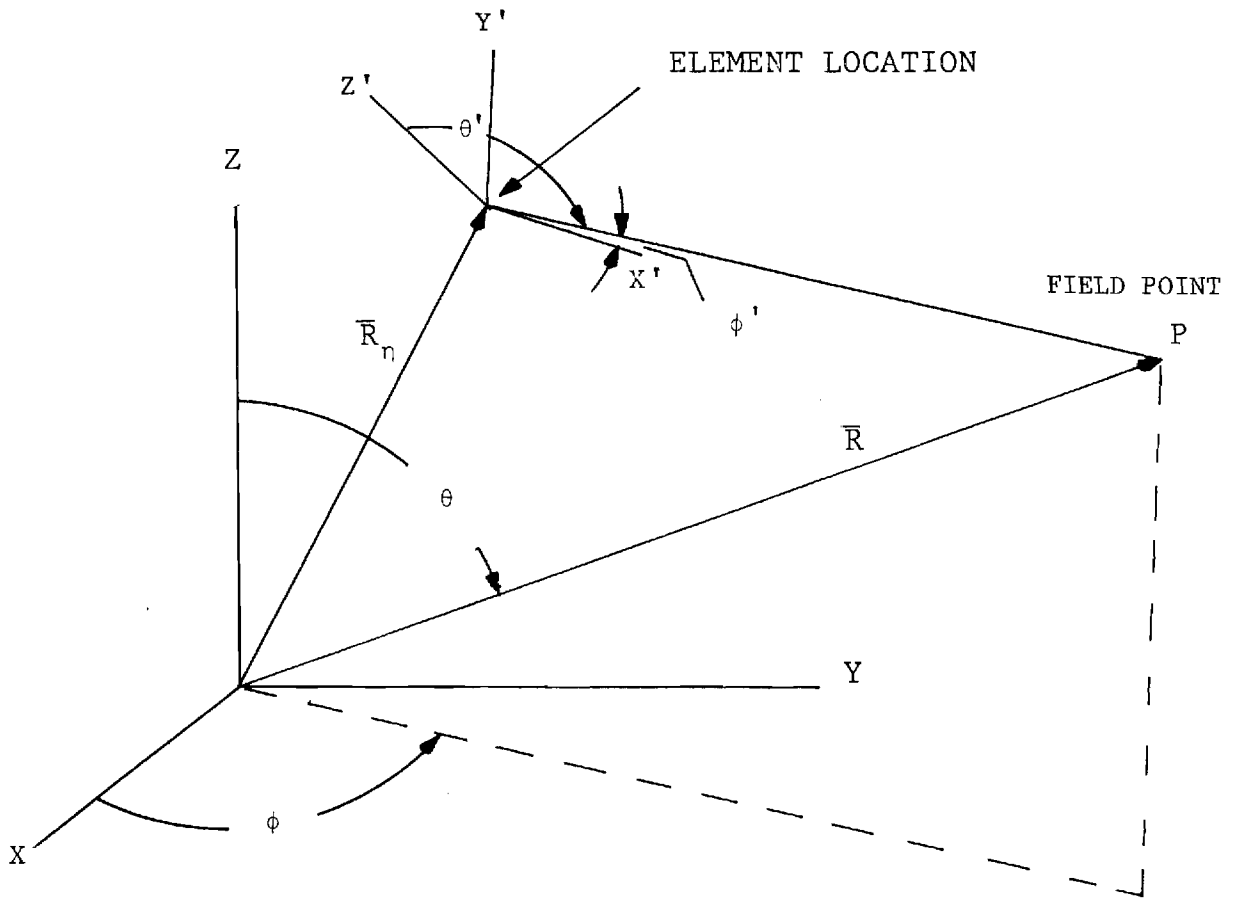


Figure 28. Coordinate System for N^{th} Array Element.

Note that the field expression $E(\theta'_n, \phi'_n)$ is not defined in terms of the reference coordinate system. A coordinate transformation must be made since E must be defined in terms of the reference coordinate system in order to apply superposition directly to each element.

Reference to Figure 28 shows that the origin of the coordinate system for n^{th} element is not located at the same point as the origin of the reference coordinate system. Also it can be seen that the axes of the two coordinate systems are not oriented in the same direction. In order to reference the two coordinate systems, a translation and rotation of axes must be performed. The translation term can be accounted for by multiplying (1) by

$$e^{jk\bar{R}_n \cdot \hat{R}}$$

where

k = propagation constant in free space

\bar{R}_n = radius vector from the origin of the unprimed coordinate system to the primed coordinate system

\hat{R} = unit vector in the direction of \bar{R} which is from the origin of the unprimed coordinate system to the field point P.

This term accounts for the difference in phase between a signal propagating from the origin of the n^{th} element coordinate system (primed) and the origin of the reference coordinate system (unprimed). Note that $\bar{R}_n \cdot \hat{R}$ is the projection of \bar{R}_n in the direction of \hat{R} . This allows the origin of the n^{th} element coordinate system to be translated back to the reference coordinate system without changing the phase in the far-field.

At this point the origins of the primed and unprimed coordinate systems are located at the same point. However, their orientations are not the same. To align the coordinate systems, a rotation of axis must be performed.

The rotation of the n^{th} coordinate system is accomplished by converting the fields in the primed coordinate system to fields in the unprimed coordinate system. Since the far-field of the element is a function of θ'_n and ϕ'_n only, it can be transformed to the unprimed coordinate system by the following equation:

$$\begin{vmatrix} E_r(\theta, \phi) \\ E_\theta(\theta, \phi) \\ E_\phi(\theta, \phi) \end{vmatrix} = \begin{vmatrix} D_{rp} \\ R_m \\ D'_{pr} \end{vmatrix} \begin{vmatrix} 0 \\ E'_\theta(\theta'_n, \phi'_n) \\ E'_\phi(\theta'_n, \phi'_n) \end{vmatrix} \quad (3)$$

where

- D'_{pr} = matrix transform of primed spherical to primed rectangular coordinates
- R_m = matrix transform of primed rectangular to unprimed rectangular coordinates
- D_{rp} = matrix transform of unprimed rectangular to unprimed spherical coordinates

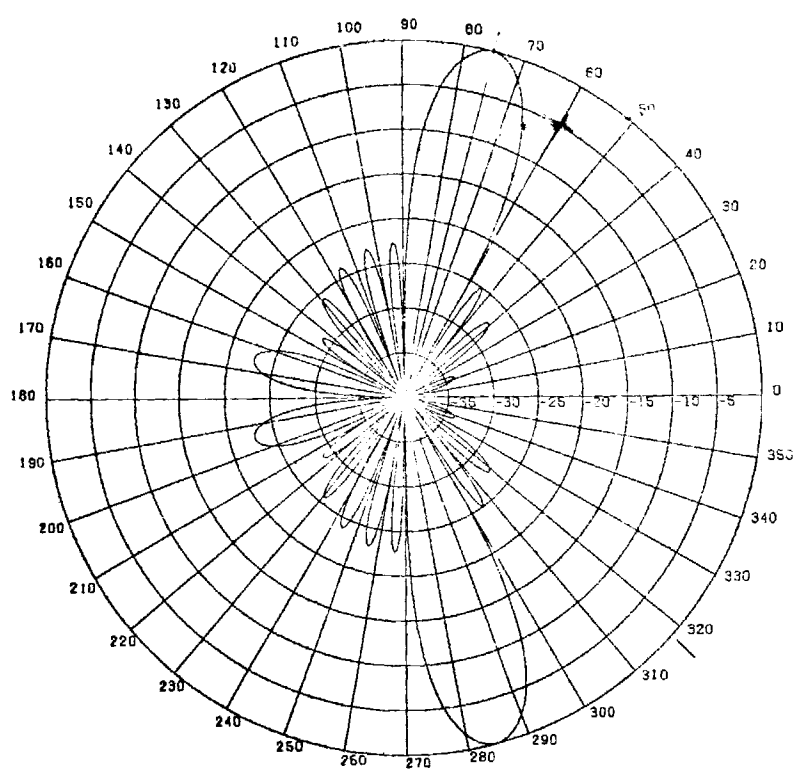
Replacing $E(\theta'_n, \phi'_n)$ in Equation 1 with Equations 2 and 3 yields the cylindrical array model equation [6].

$$\begin{vmatrix} F_r(\theta, \phi) \\ F_\theta(\theta, \phi) \\ F_\phi(\theta, \phi) \end{vmatrix} = \sum_{n=1}^N A_n e^{jk\bar{R}_n \cdot \hat{R}} \begin{vmatrix} D_{rp} \\ R_m \\ D'_{pr} \end{vmatrix} \begin{vmatrix} 0 \\ E'_\theta(\theta'_n, \phi'_n) \\ E'_\phi(\theta'_n, \phi'_n) \end{vmatrix} \quad (4)$$

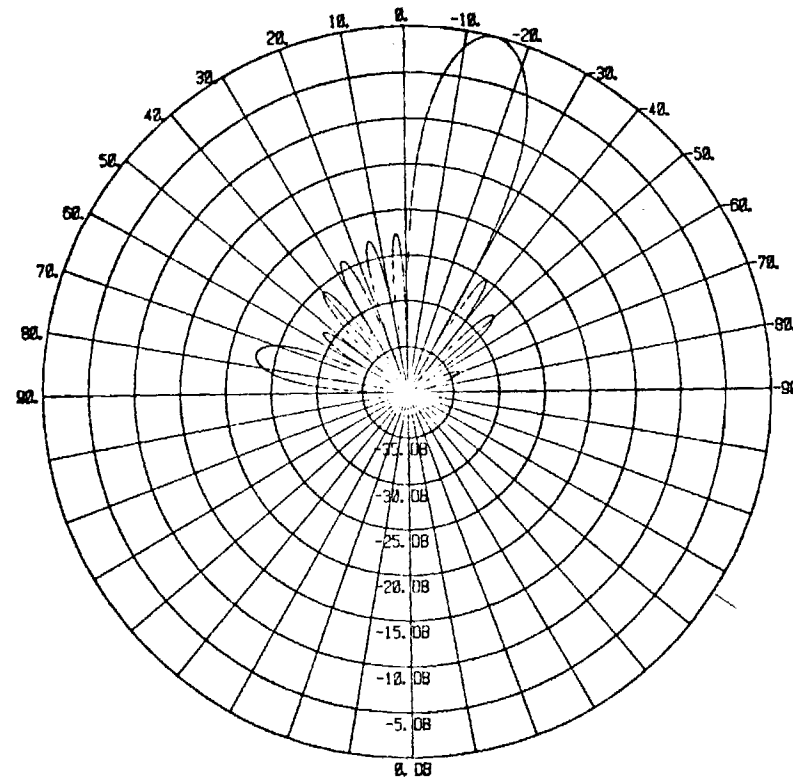
Implementing this equation on the digital computer yields an accurate model for the cylindrical phased array as will be shown in the next section.

3. Verification of Array Model

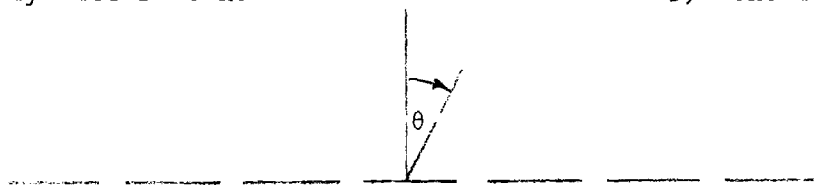
The verification of the array model was performed by comparing the results generated by the array model with results found in the literature as well as results generated by other methods. Figure 29 shows the pattern of a 7-element linear array of half wave horizontal dipoles. The array was designed for a main beam steering angle of 74° referenced to a line tangent to the array. Using the equation for a half wave dipole and the array factor generated from the array geometry will yield the polar plot shown in Figure 29a. Using the cylindrical array model and the geometry shown in Figure 29c yields the plot of Figure 29b. The plots are identical, with the only difference noted in the definition of the angle θ (referenced for cylindrical model is shown in Figure 29c).



a) Generated by array factor method



b) Generated by cylindrical array model



c) Array geometry

Figure 29. Polar Plot of a 7 Element Horizontal Dipole Linear Array Steered to 75 Degrees. (Note that for coordinate system of b) and c) steering angle is 15°)

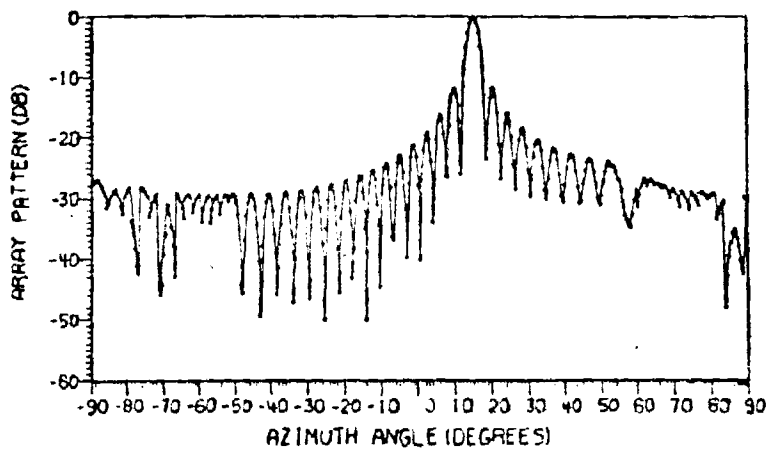
Next, a circular array was investigated and the data are shown in Figure 30. The array was made up of 32 uniformly spaced, vertical dipole elements. The excitations were designed to steer the main beam to an angle of 15° off boresight. Data generated by Hsiao [6] are shown in Figure 30a, and the result of the mathematical array model is shown in Figure 30b. There appears to be no appreciable difference between the outputs.

A two-dimensional array was also investigated and the results are shown in Figure 31. The array is a 7×13 cylindrical array of vertical dipoles. Again comparing the results generated by the mathematical array model and that generated by Hsiao shows no appreciable difference.

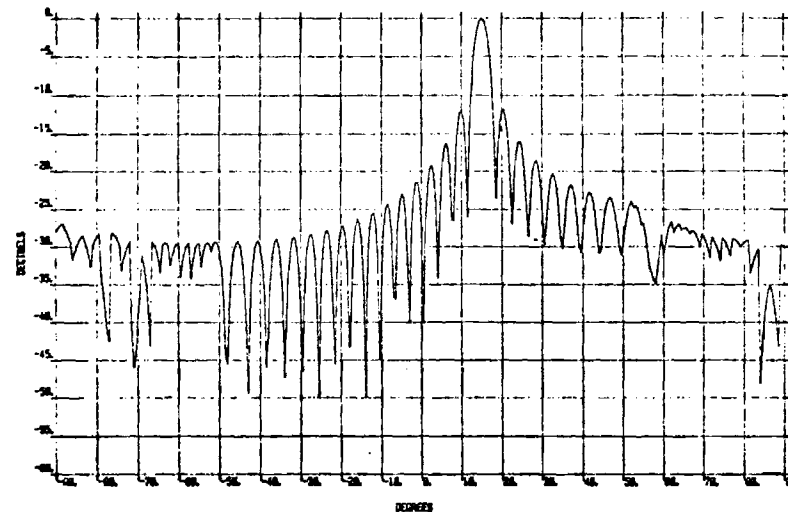
An experimental check of the model is shown in Figure 32. The plot compares theoretical data generated by the mathematical array model (solid line) with experimental data (dots) generated by Cofer and Goodman [1]. The theoretical input excitation data used in the array model were generated by measuring the actual input excitations used by Cofer and Goodman for a feed offset of 0.34 inch and a frequency of 9.3 GHz. The theoretical input element pattern data were taken from Figure 60 of Cofer and Goodman. The vertical element spacing in the mathematical model was set for a vertical steering angle of $\theta = 60^\circ$. This was necessary since the array used by Cofer and Goodman utilized continuous slots whereas the cylindrical array model utilizes discrete slots. Since experimental data were not available for feed offset of 0.34 inch, the experimental data of Figure 32 were generated by interpolating between the data presented in Figures 57 and 58 of Cofer and Goodman. These interpolated data show a close correlation to the theoretical data and again indicate the usefulness of the mathematical array model as an accurate means of analyzing cylindrical array structures.

B. Computer Model Results

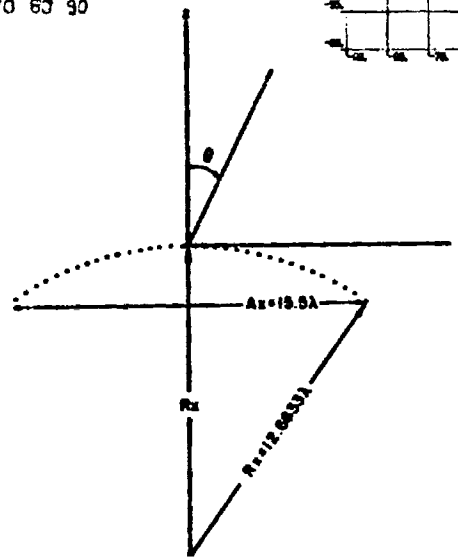
The special problems associated with cylindrical array antennas were discussed in Chapter II. The mathematical model used to study these problems was described in the preceding section. In this section the results of the computer study will be presented which show how beamwidths and grating lobe levels are affected by varying the illumination sector, element spacing and radius of the cylindrical array. In all cases shown below a cosine excitation taper in azimuth was used.



a) Generated by Hsiao [6].

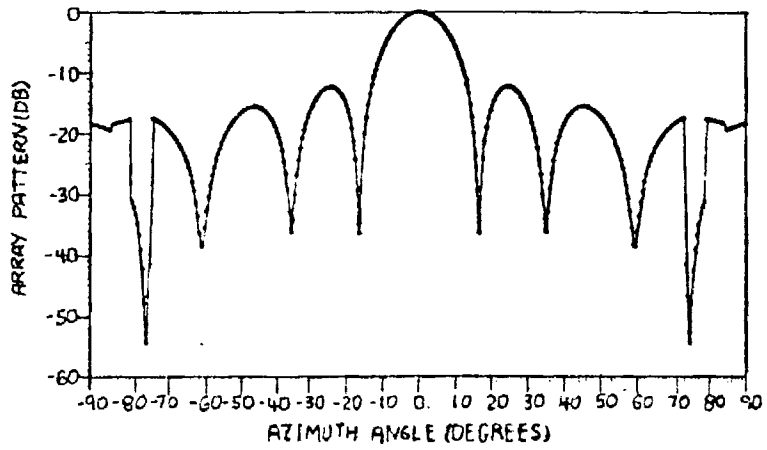


b) Generated by cylindrical array model.

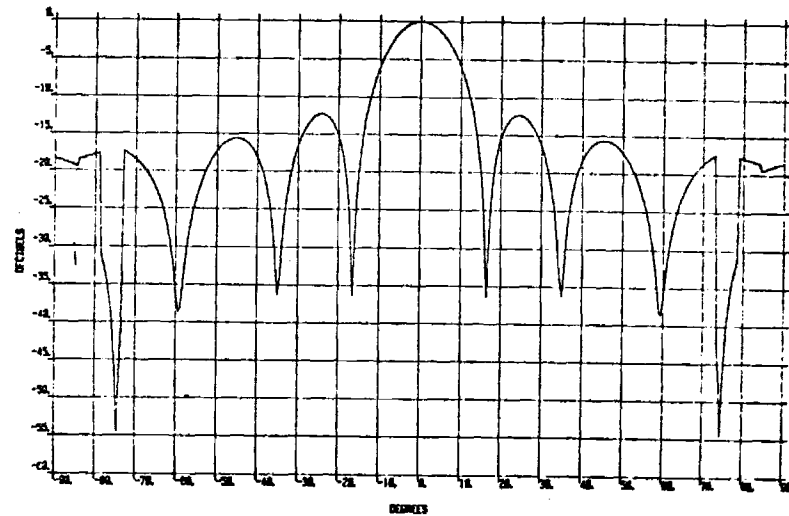


c) Geometry

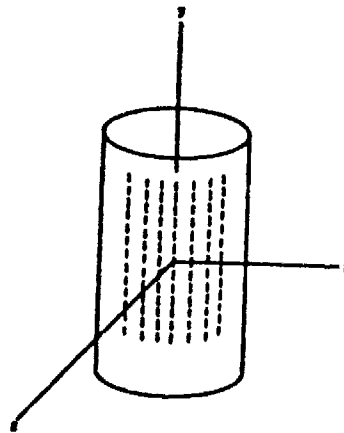
Figure 30. Far-Field Pattern for a 32 Element Uniformly Spaced Circular Array.



a) Generated by Hsiao [6]



b) Generated by cylindrical array model



c) Geometry

Figure 31. Far-Field Pattern For a 7 x 13 Uniformly Spaced Cylindrical Array.

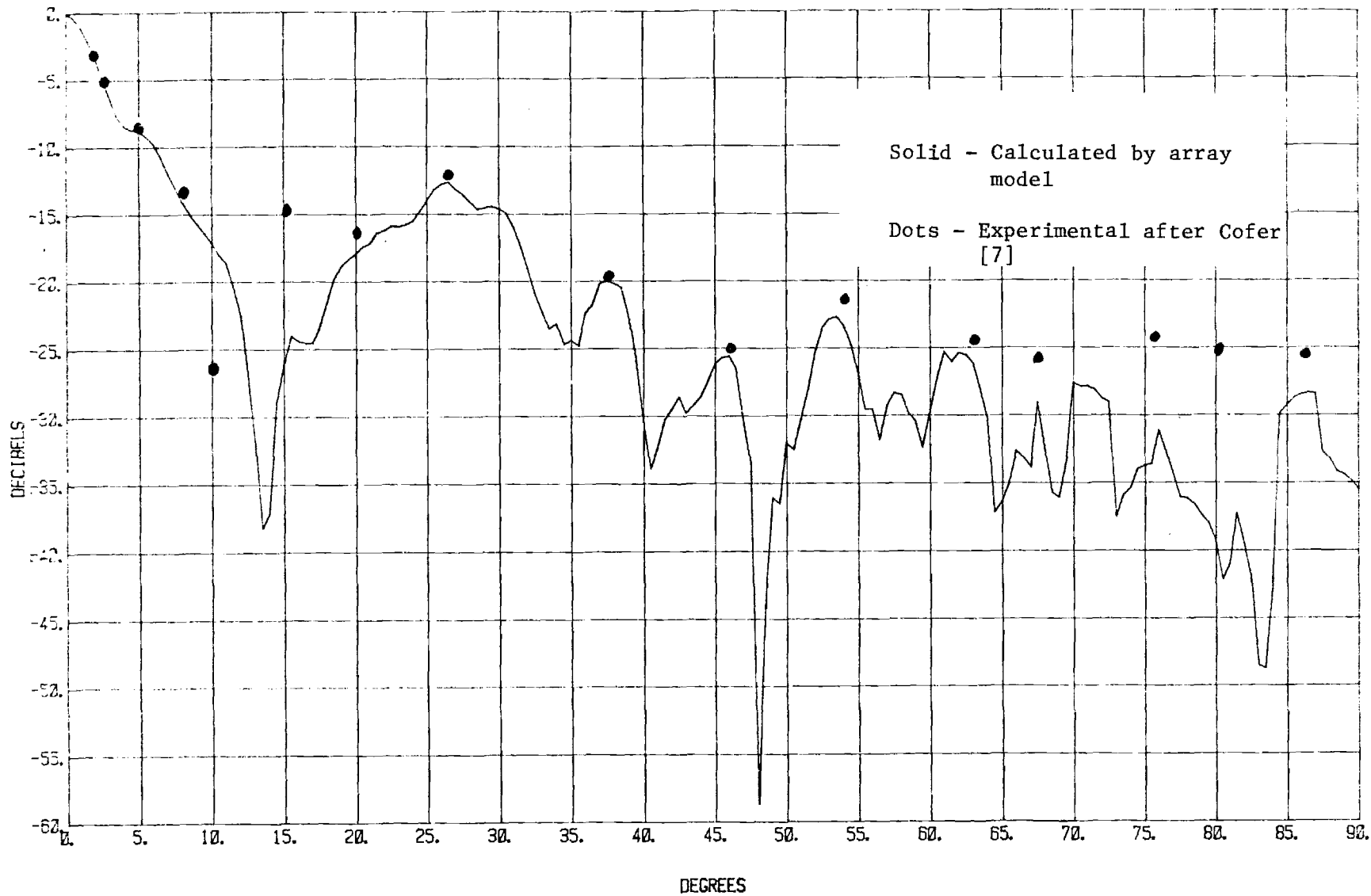


Figure 32. E-Plane (Azimuth) Radiation Pattern of a 47 Element Cylindrical Array of Slotted Waveguides Operating at a Frequency of 9.4 GHz. Conical cut, $\theta = 60^\circ$. Feed Offset, $\Delta = 0.34$ in.

1. Grating Lobes and Beamwidth vs. Illumination Sector

It was shown in Chapter II that there is a relationship between the level of the grating lobes and the sector of the cylinder that is illuminated. Also, it should be apparent that the 3-dB beamwidth of the main beam will be affected by a change in the illumination sector since the size of the projected aperture will also be changed. Figures 33 - 35 show predicted far-field patterns for a cylindrical array with all parameters held constant except, ϕ_{ill} , the illumination sector. In all three figures, the operating wavelength, λ , is 0.72", the radius, R , is 12" (16.98λ), and the element spacing, S , is 0.42" (0.58λ). In Figure 33, $\phi_{ill} = 120^\circ$, the beamwidth is 2.4° , and there is a -17 dB grating lobe at about 93° . The ϕ_{ill} for Figure 34 was reduced to 105° , which caused the beamwidth to increase to 2.6° ; however, the grating lobe level was reduced to -19 dB. In Figure 35, $\phi_{ill} = 75^\circ$, reducing the grating lobe to -28 dB, and increasing the beamwidth to 3.4° .

Many curves like Figures 33 - 35 were produced for different values of ϕ_{ill} and different radii. Figure 36 is a summary of these results. This figure is very useful in designing cylindrical arrays since the radius and illumination sector required to yield a desired beamwidth can be directly determined. For example, a 3° beamwidth could be achieved with $R = 10"$ and $\phi_{ill} = 120^\circ$; $R = 12"$ and $\phi_{ill} = 88^\circ$; or $R = 14"$ and $\phi_{ill} = 75^\circ$.

Although any one of these three designs would yield the same beamwidth, there would be a considerable difference in the grating lobe levels since it was shown that the grating lobes increase with increased ϕ_{ill} . It is desirable to produce a narrow beamwidth with the smallest possible radius in order to achieve a compact antenna design. Therefore, it is necessary to find a way of controlling grating lobe levels without reducing the illumination sector. This problem will be studied in the next section.

2. Grating Lobe Levels vs. Element Spacing

In this section three different predicted element patterns and far-field patterns will be presented with all parameters held constant except S , the spacing (arc length) between elements around the cylinder. In all cases $\lambda = 0.72"$, $R = 12"$, and $\phi = 120^\circ$

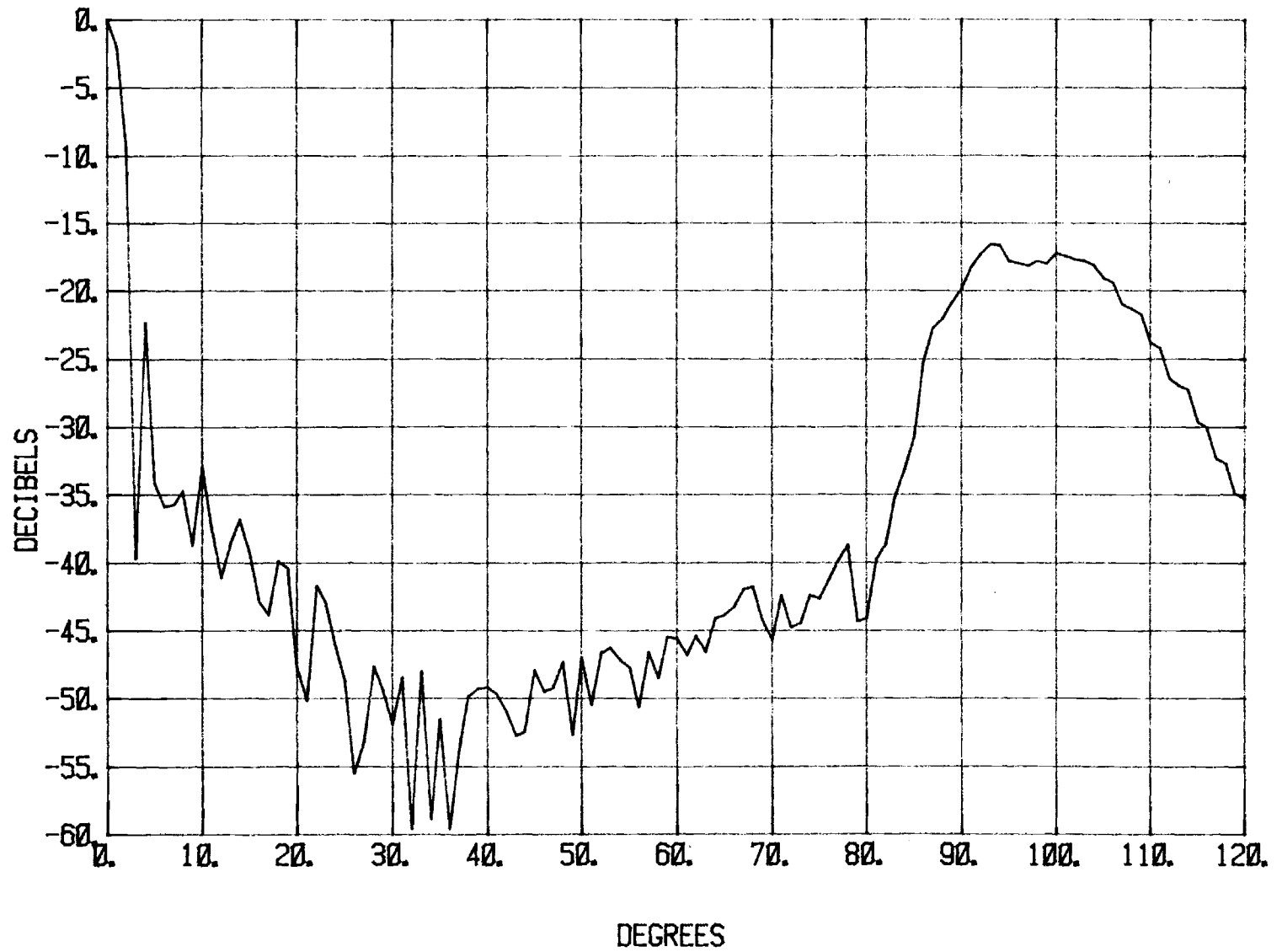


Figure 33. Far-Field Pattern for Cylindrical Array Antenna with $\lambda = 0.72''$, $R = 12''$, $S = 0.42''$ and $\phi_{ill} = 120^\circ$.

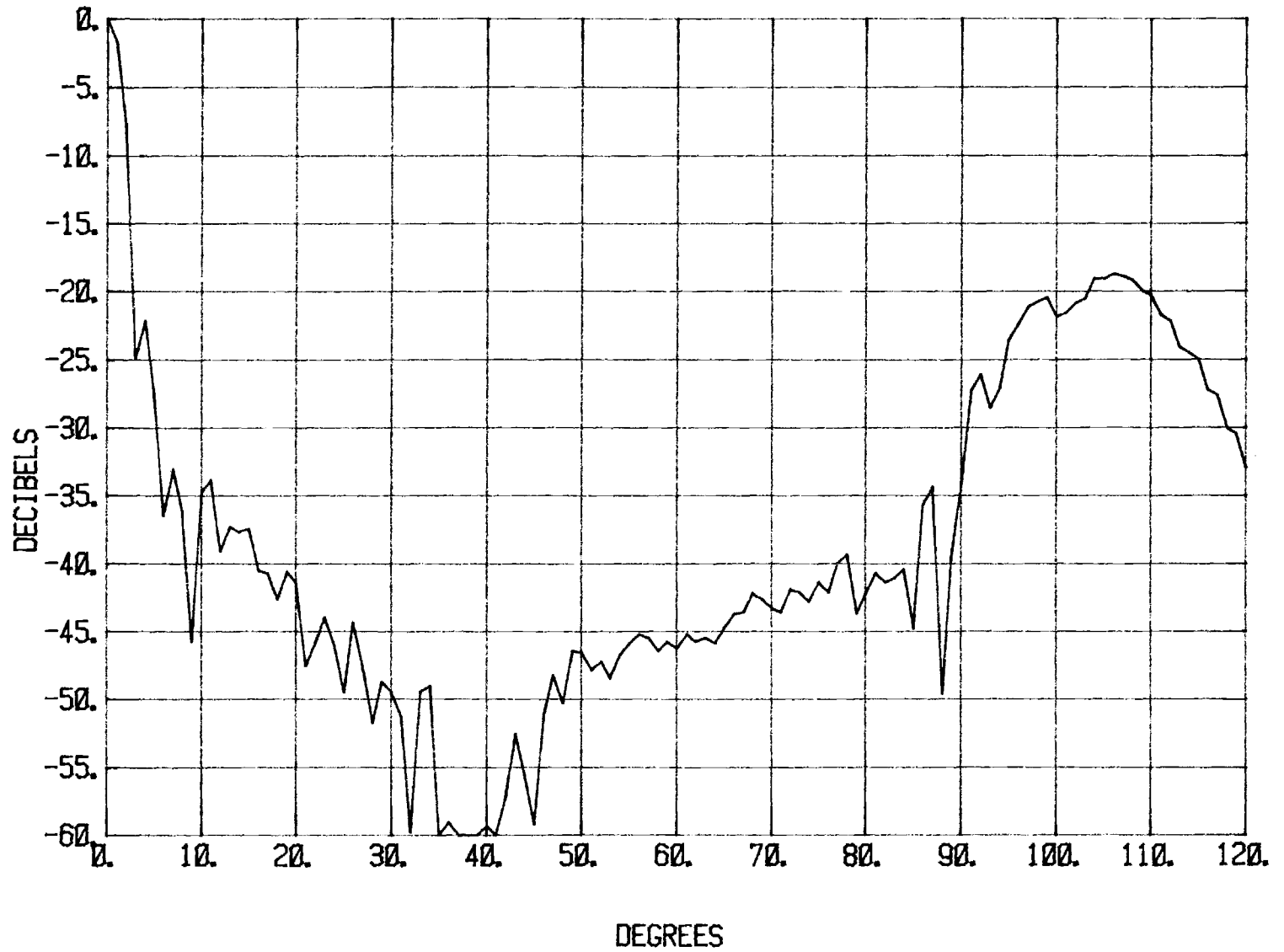


Figure 34. Far-Field Pattern for a Cylindrical Array Antenna with $\lambda = 0.72''$, $R = 12''$, $S = 0.42''$ and $\phi_{ill} = 105^\circ$.

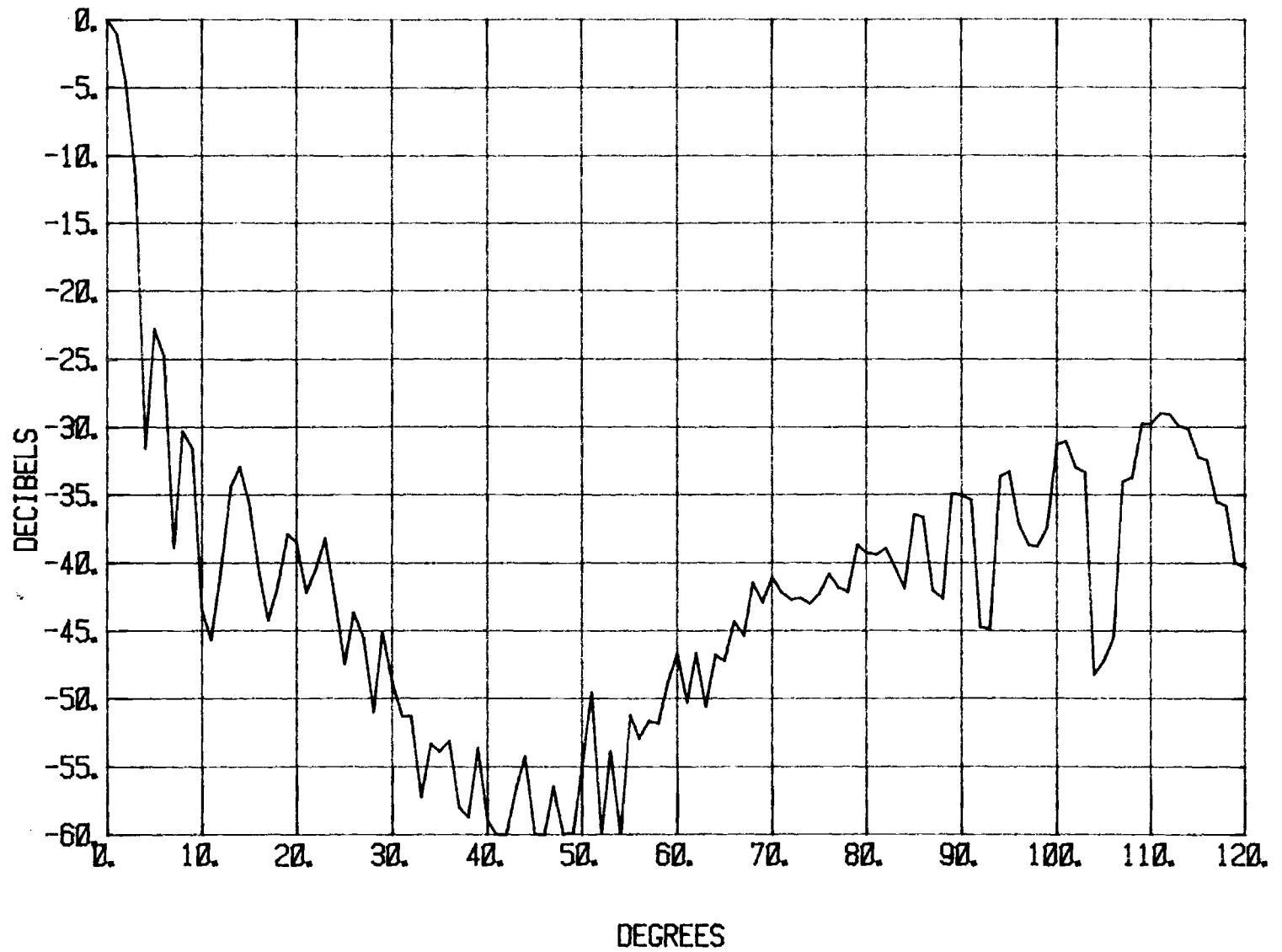


Figure 35. Far-Field Pattern for a Cylindrical Array Antenna with $\lambda = 0.72''$, $R = 12''$, $S = 0.42''$ and $\phi_{ill} = 75^\circ$.

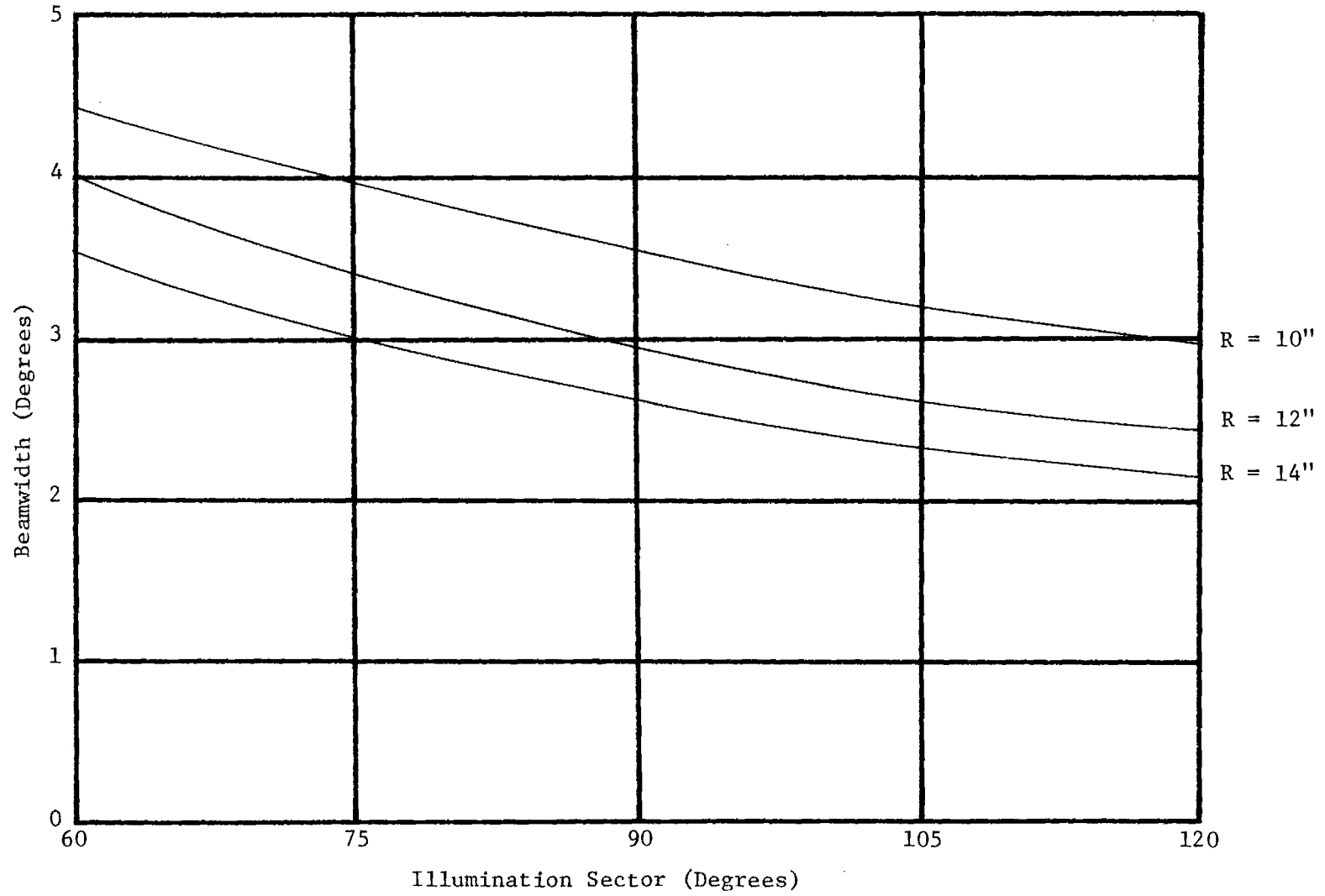


Figure 36. Beamwidth Vs. Illumination Sector (ϕ_{ill}) for $\lambda = 0.72''$ and $S = 0.42''$.

Figure 37 shows the predicted element pattern for an element spacing of 0.48" (0.67λ). This element pattern has "nulls" at $\pm 28^\circ$ and deep ripples in the main beam area. Figure 38 shows the far-field pattern for this element spacing with $\phi_{ill} = 120^\circ$. The grating lobe level is at -12 dB. Therefore, this element spacing would not be suitable for use in a cylindrical array with $\phi_{ill} = 120^\circ$.

When the spacing between elements is reduced to 0.42" (0.58λ) the element pattern is improved as can be seen in Figure 39. Here the nulls have moved out to about $\pm 40^\circ$, and the ripples in the main beam area are smaller than they were in Figure 37. The far-field lobe has been reduced to -17 dB (see Figure 40).

If the element spacing is reduced to 0.36" (0.5λ), the element pattern (Figure 41) begins to look very much like the isolated element pattern of Figure 35. There are no nulls and the ripples are reduced to an insignificant level. Figure 42 shows the far-field pattern for the $S = 0.36$ " case. Now the grating lobe is down to -25 dB, which is an acceptable level since it is below the -23 dB first side lobe.

The computer model was used to predict far-field patterns for many combinations of illumination sector and element spacing. Figure 43 is a composite result of this study. This curve can be used to determine what illumination sector and element spacing are required to keep the grating lobes below any desired level.

3. Grating Lobe and Beamwidth vs. Radius

It was expected that the radius of the cylinder would affect both beamwidth and grating lobe levels. Therefore, the model was used to predict far-field patterns with all parameters fixed except radius. In all cases, $\lambda = 0.72$ " , $S = 0.42$ ' and $\phi_{ill} = 90^\circ$.

Figure 44 shows the far-field pattern where $R = 10$ " (13.89λ). The beamwidth is 3.6° and the grating lobe level is -27 dB. In Figure 45 $R = 12$ " (16.98λ), the beamwidth is reduced to 3.0° , and the grating lobe level is -23.4 dB. When the radius is increased to 14" (19.44λ), Figure 46 shows that the beamwidth is 2.6° and the grating lobe level is -23.4 dB. A composite summary of this study is shown in Figure 47.

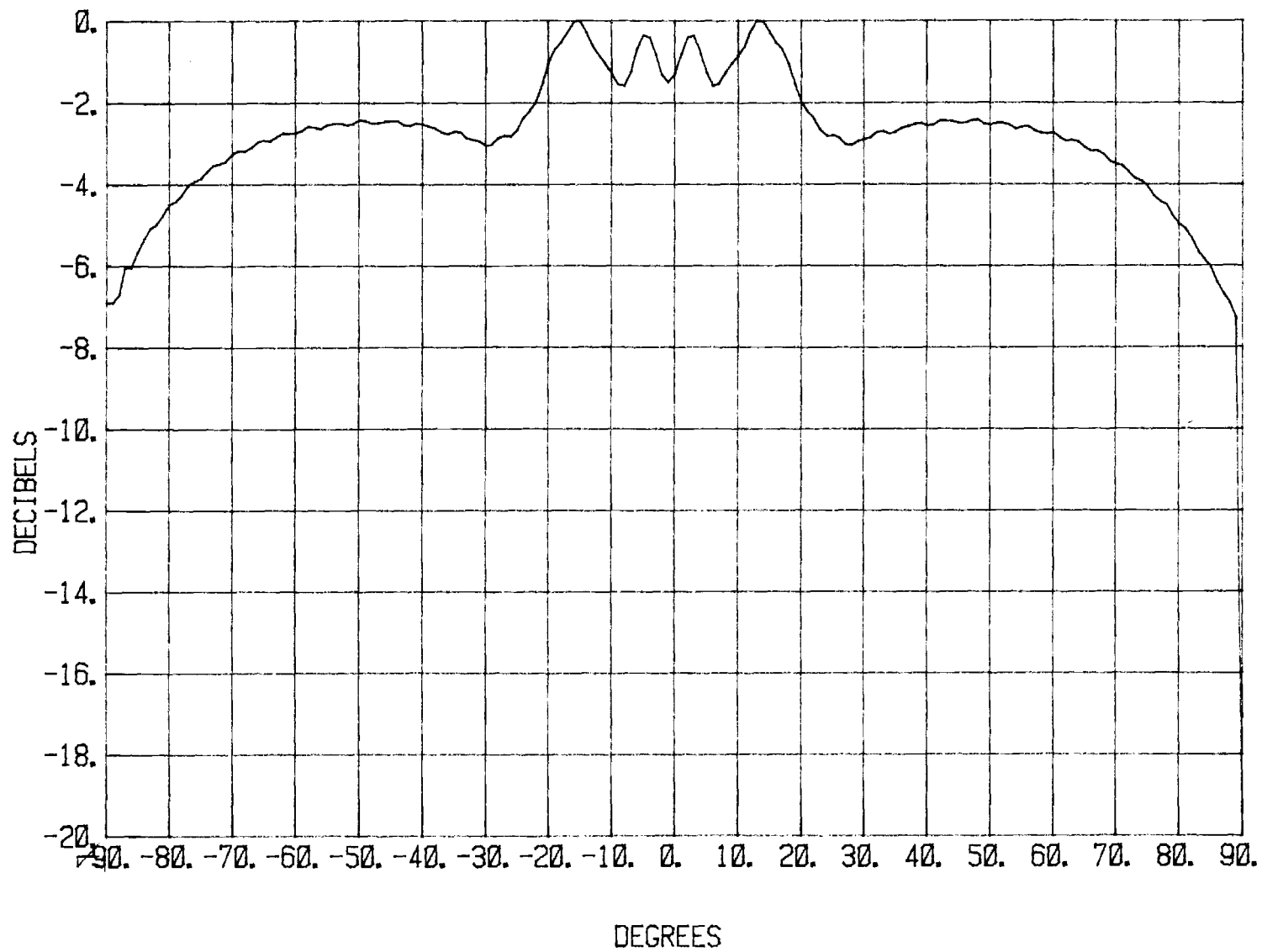


Figure 37. Element Pattern for Element in Cylindrical Array Environment with $S = 0.48''$ (0.67λ).

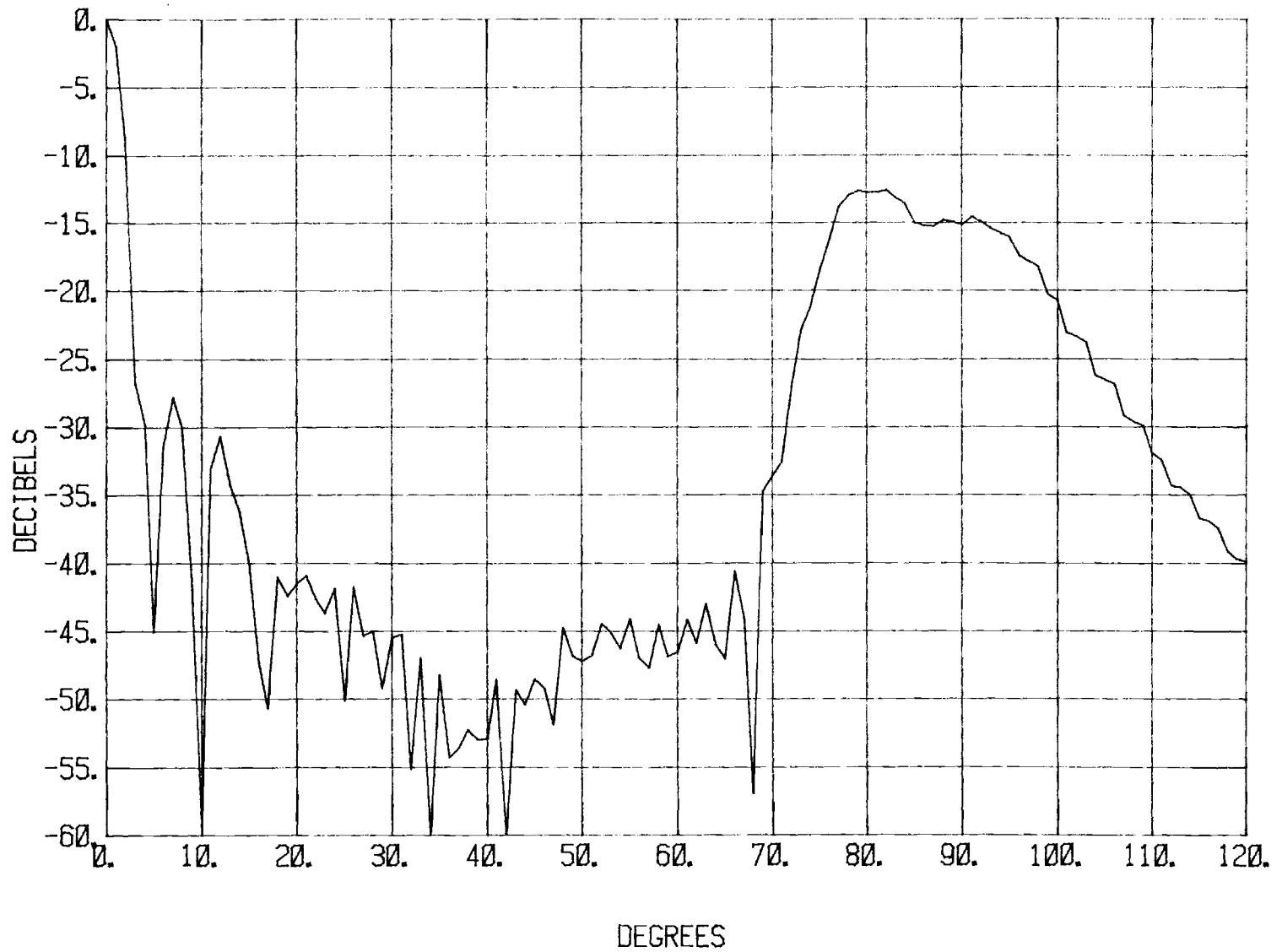


Figure 38.: Far-Field Pattern for a Cylindrical Array Antenna with $\lambda = 0.72''$, $R = 12''$, $S = 0.48''$ and $\phi_{ill} = 120^\circ$.

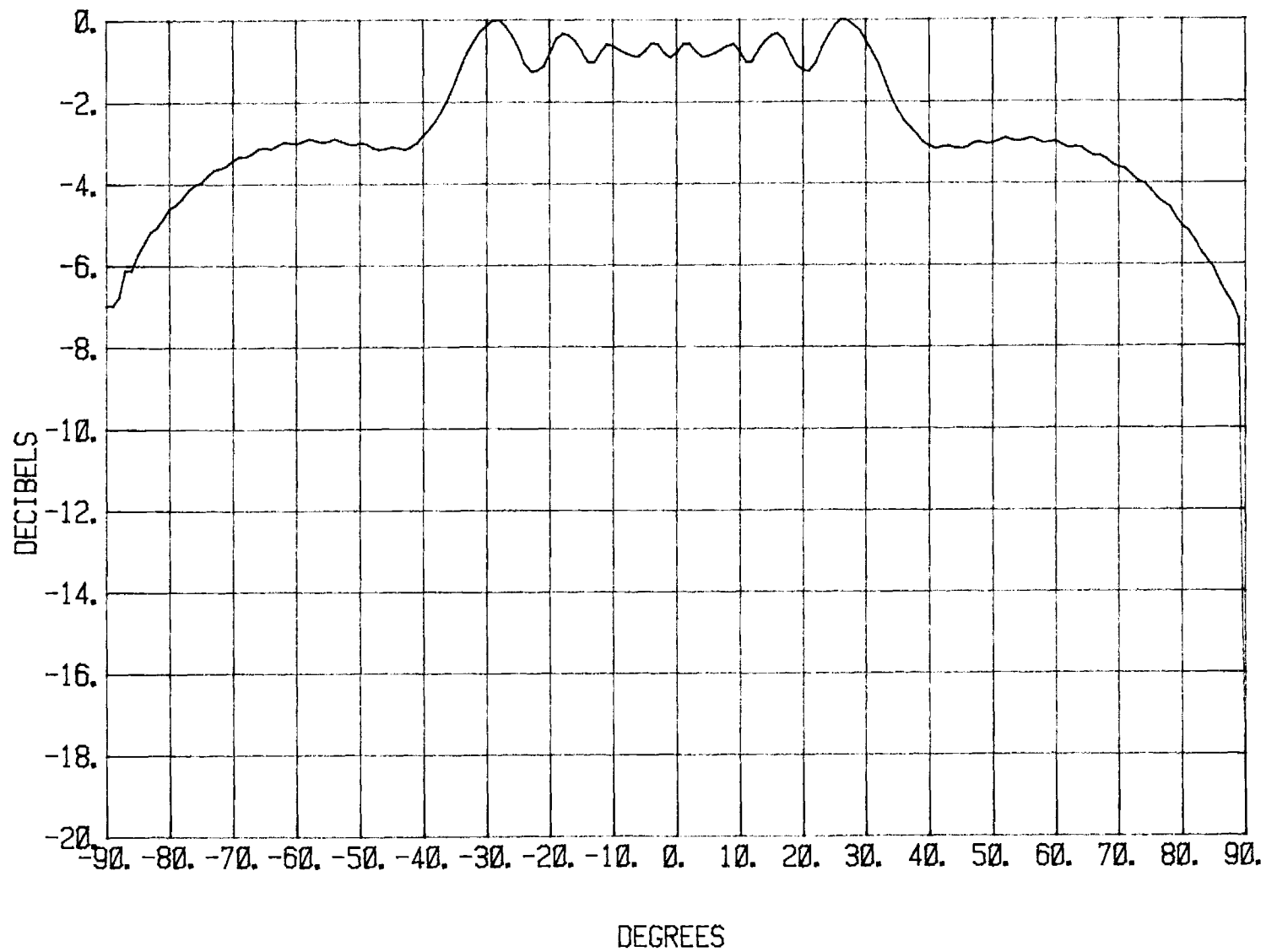


Figure 39. Element Pattern for Element in Cylindrical Array Environment with $S = 0.42'' (.58\lambda)$.

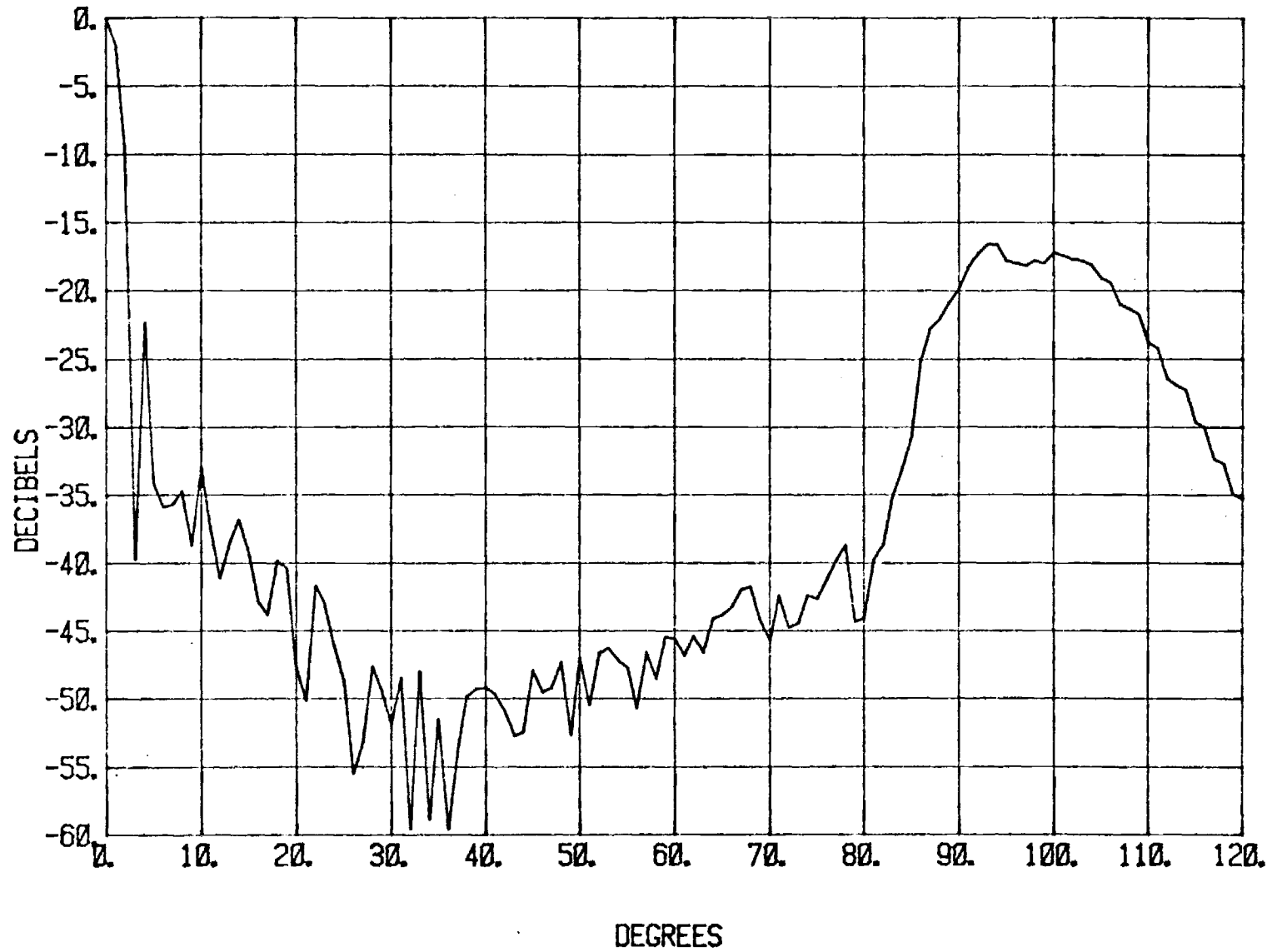


Figure 40. Far-Field Pattern for Cylindrical Array Antenna with $\lambda = 0.72''$, $R = 12''$, $S = 0.42''$ and $\phi_{fill} = 120^\circ$.

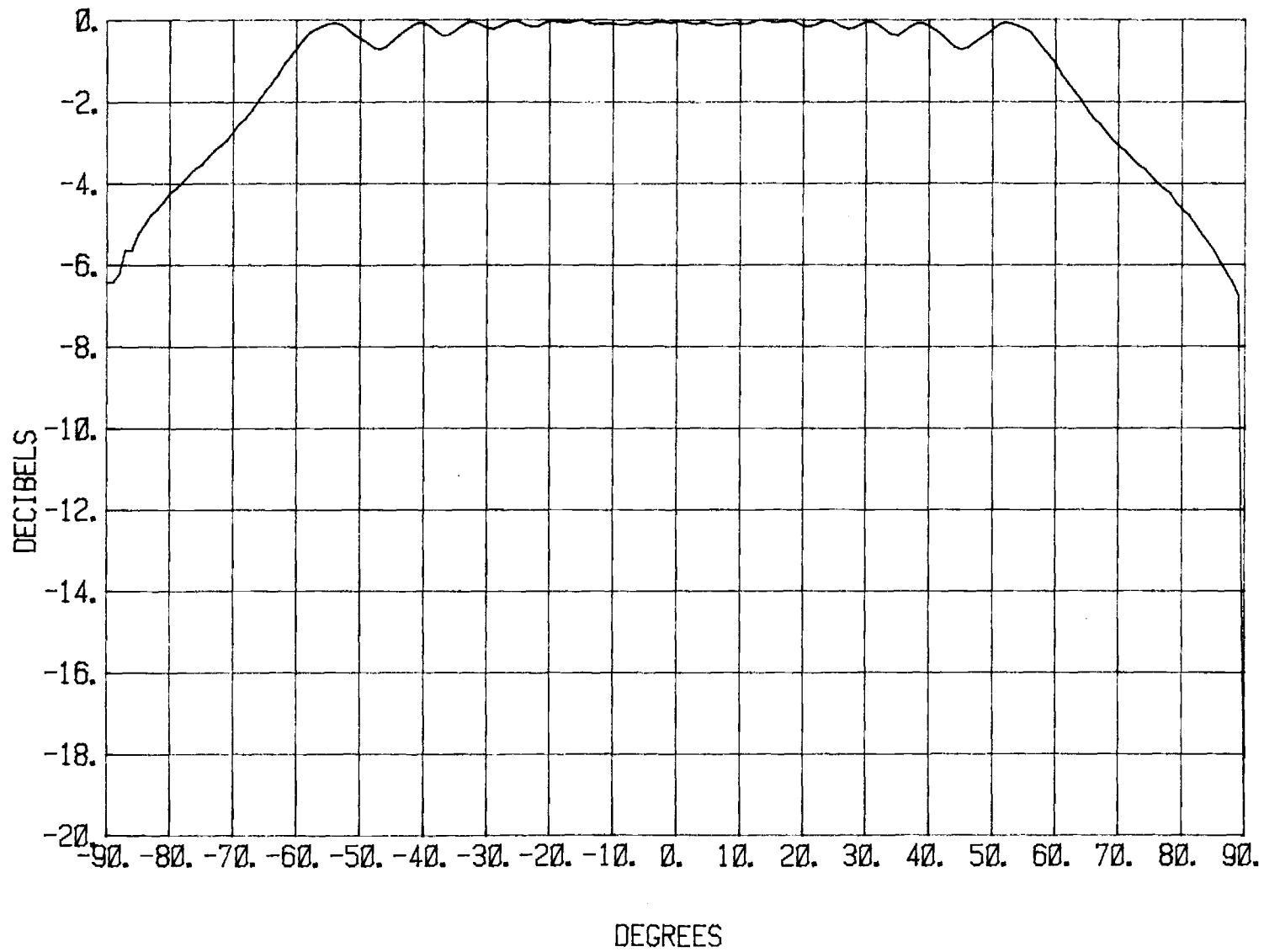


Figure 41. Element Pattern for Element in Cylindrical Array Environment with $S = 0.36'' (0.5\lambda)$.

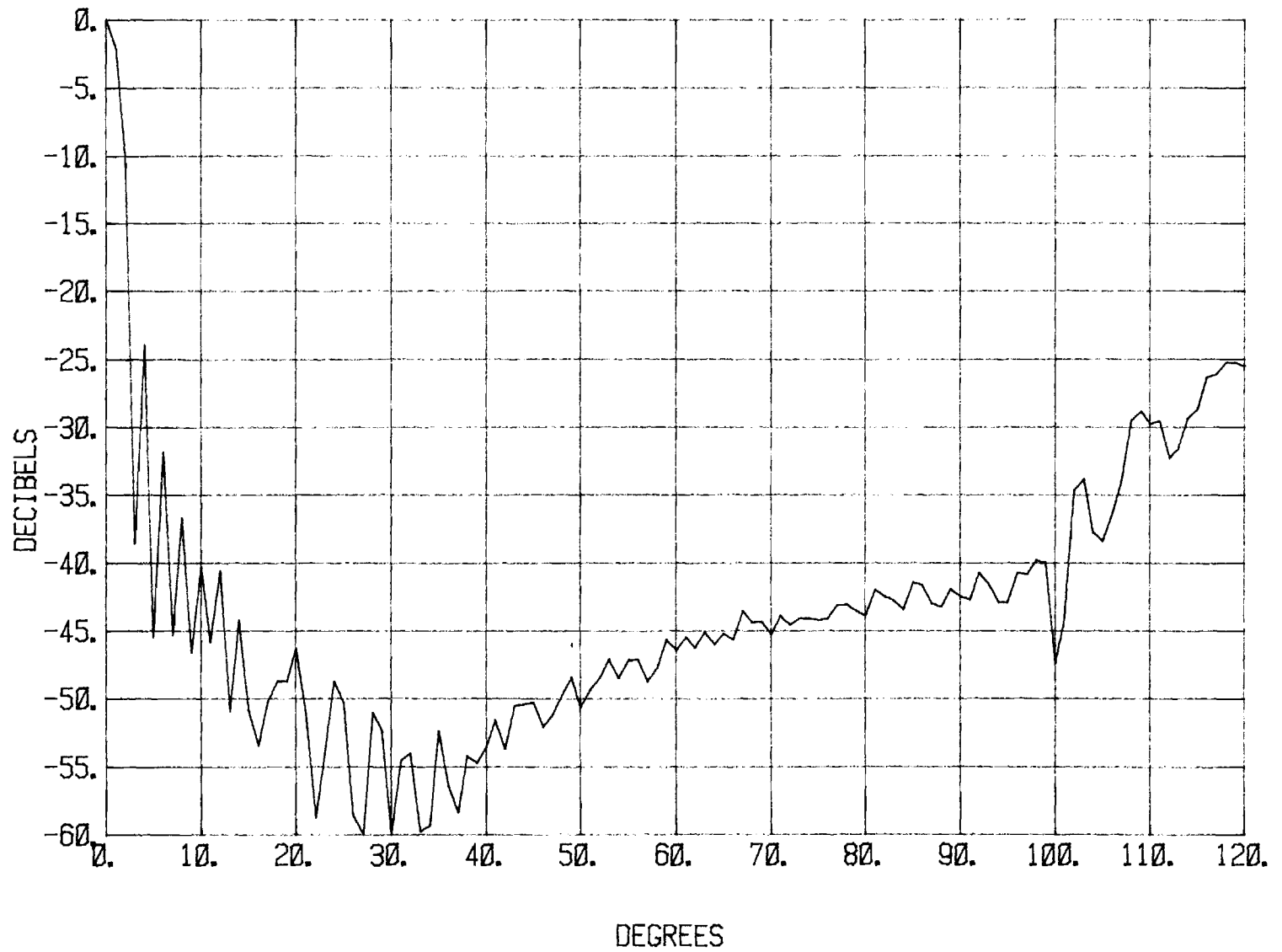


Figure 42. Far-Field Pattern for Cylindrical Array Antenna with $\lambda = 0.72''$, $R = 12''$, $S = 0.36''$ and $\phi_{i11} = 120^\circ$.

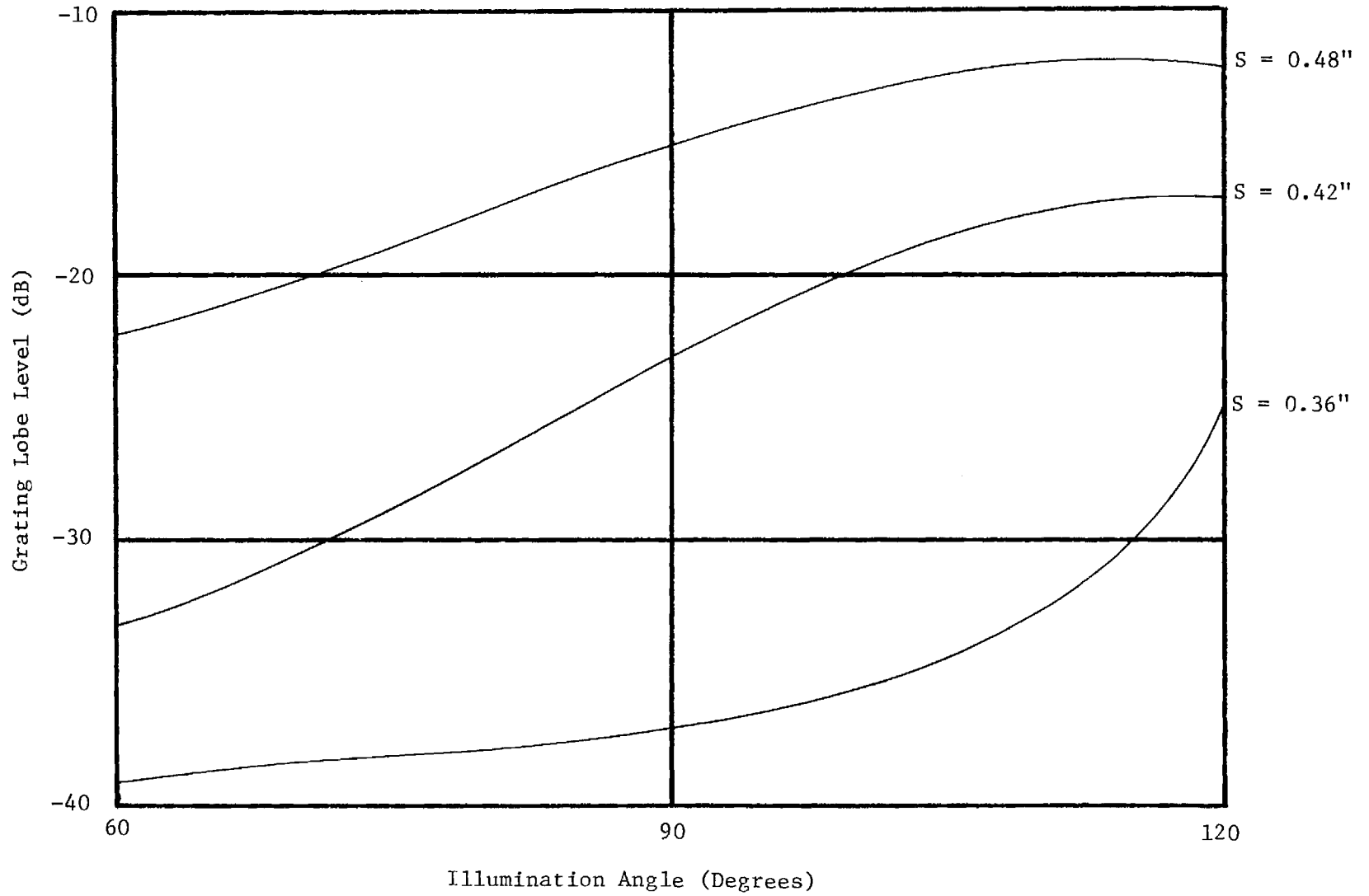


Figure 43. Grating Lobe Level Vs. Illumination Sector (ϕ_{111}) for Element Spacings of $S = 0.48''$, $S = 0.42''$ and $S = 0.36''$ with $R = 12''$ and $\lambda = .72''$.

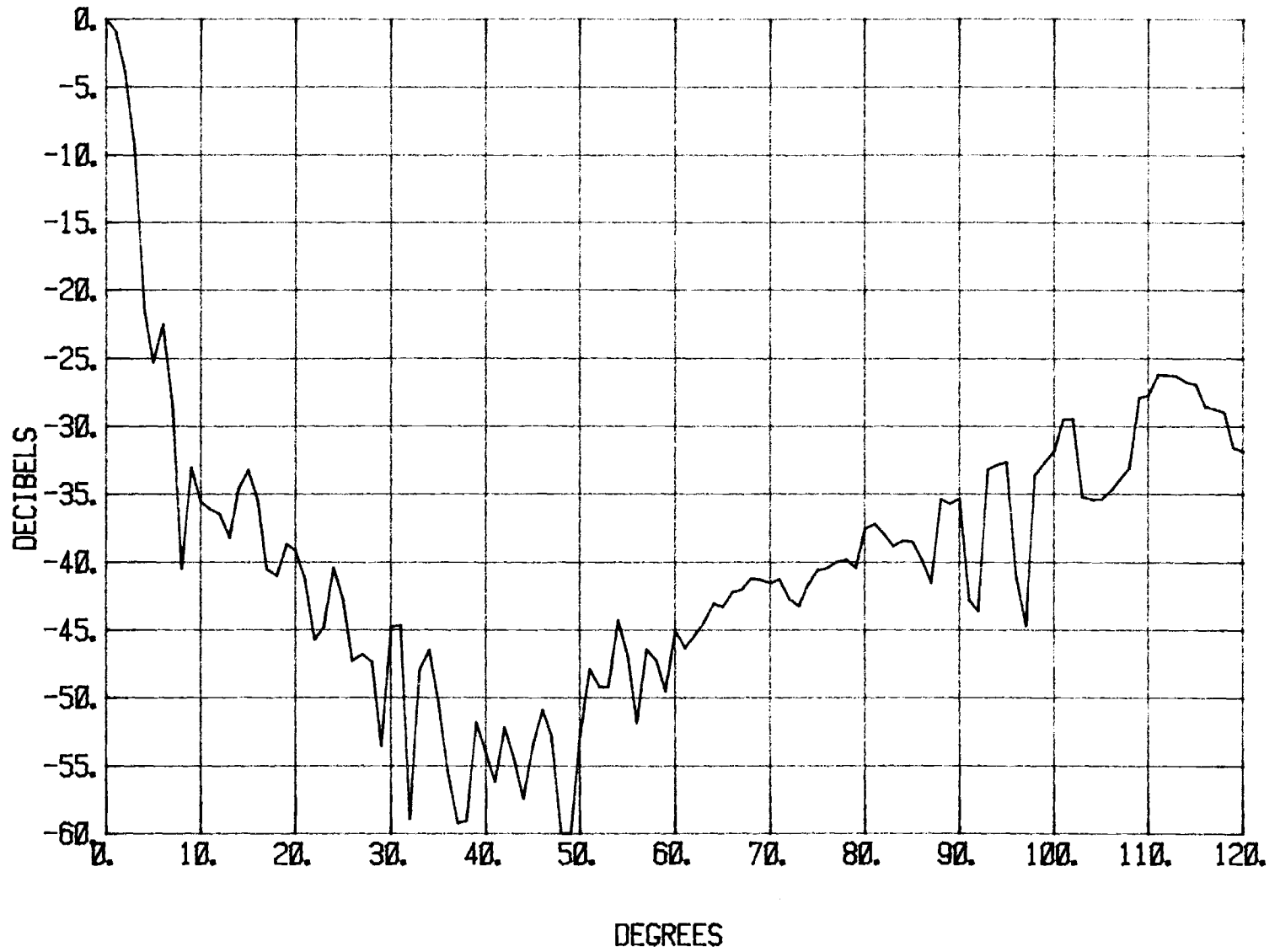


Figure 44. Far-Field Pattern for Cylindrical Array Antenna with $\lambda = 0.72''$, $R = 10''$, $S = 0.42''$ and $\phi_{ill} = 90^\circ$.

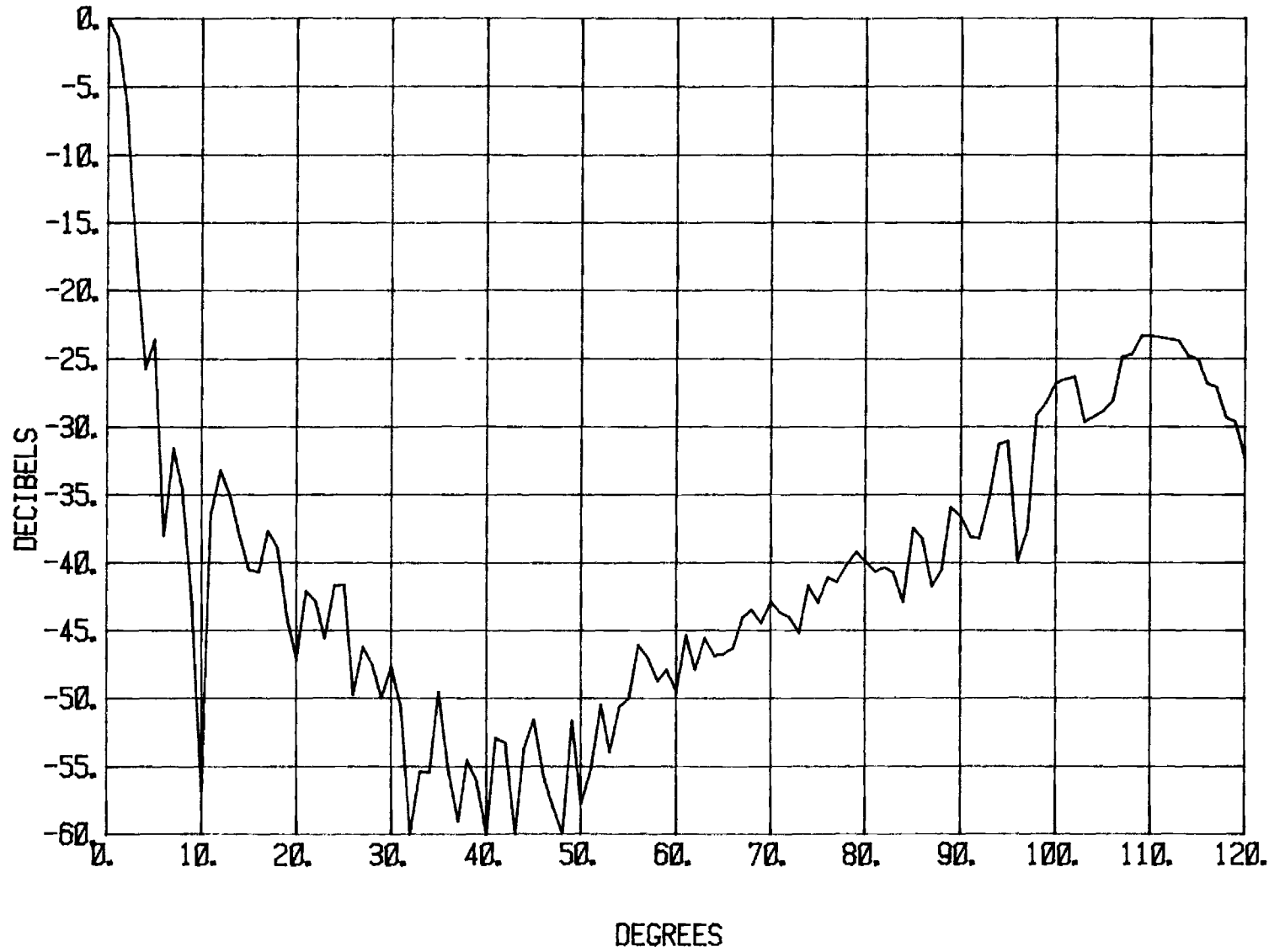


Figure 45. Far-Field Pattern for Cylindrical Array Antenna with $\lambda = 0.72''$, $R = 12''$, $S = .42''$ and $\phi_{111} = 90^\circ$.

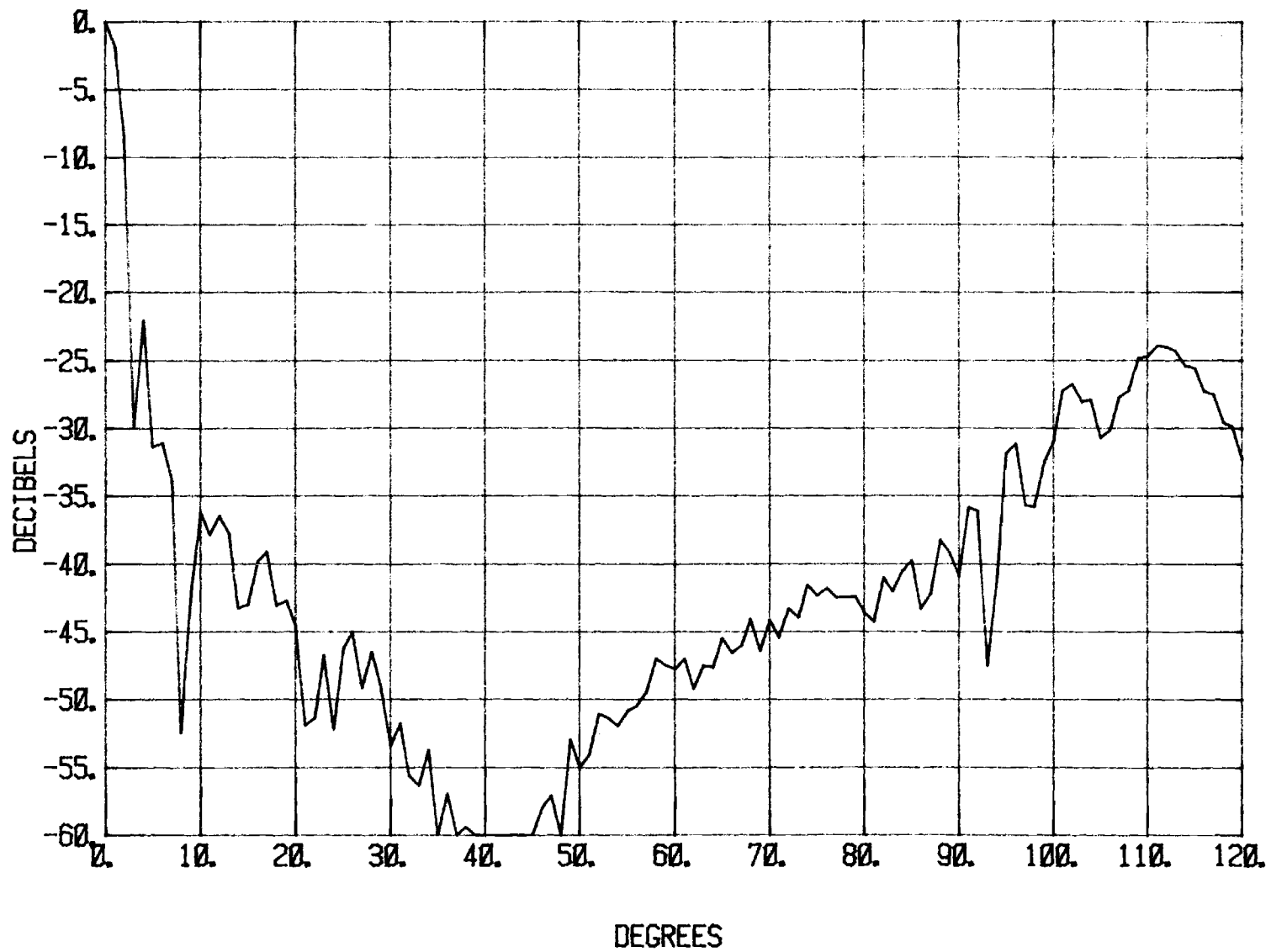


Figure 46. Far-Field Pattern for Cylindrical Array Antenna with $\lambda = 0.72''$, $R = 14''$, $S = 0.42''$ and $\phi_{ill} = 90^\circ$.

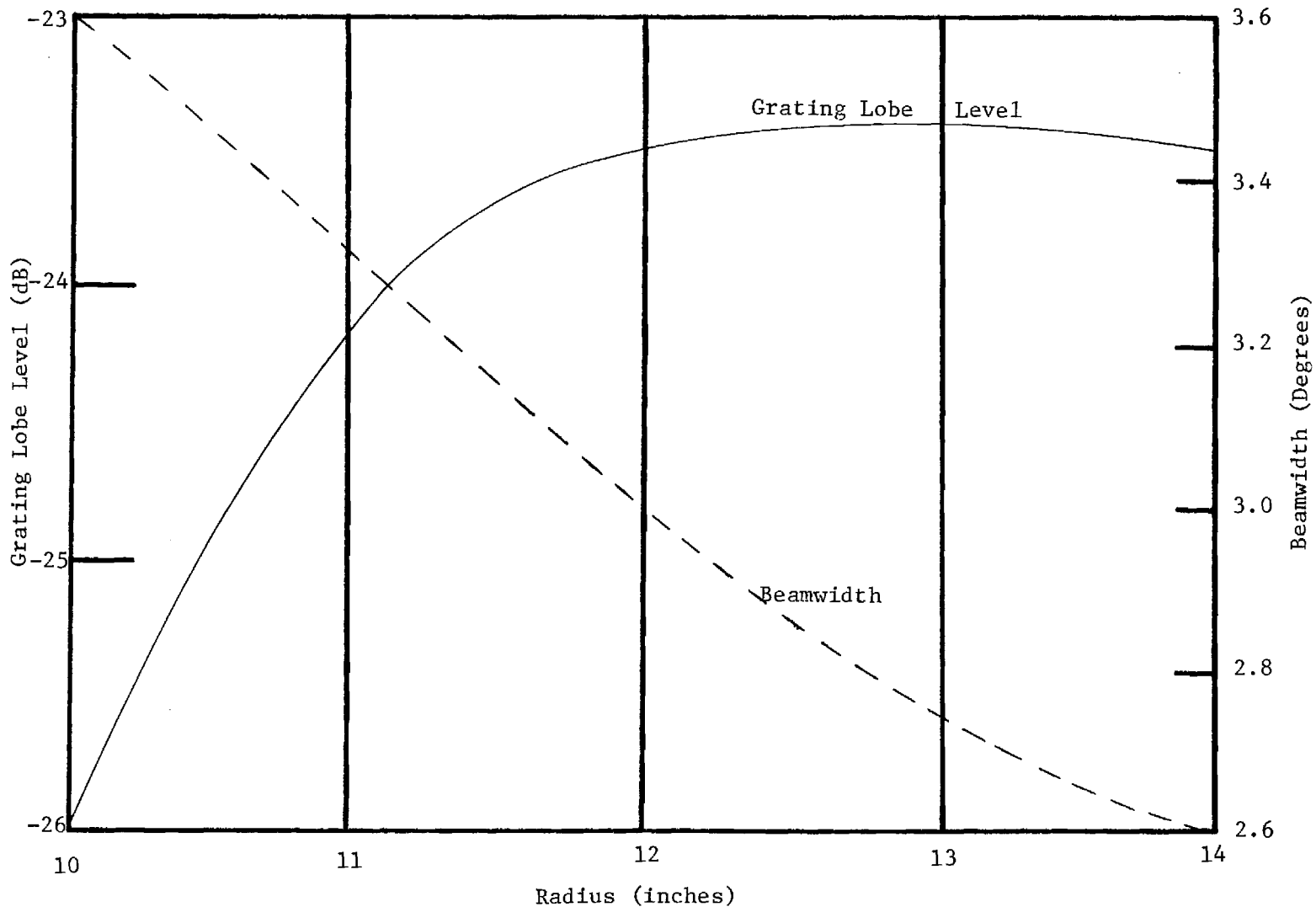


Figure 47. Grating Lobe Level and Beamwidth Vs. Radius With $\lambda = 0.72''$, $S = 0.42''$ and $\phi_{ill} = 90^\circ$.

4. Defocus of Main Beam vs. Steering Angle

As discussed in Section II, the array is designed to focus the main beam at one fixed elevation angle θ_0 . If the beam is frequency scanned to another elevation, θ_1 , a phase error is introduced which results in a defocusing of the main beam. Figures 48 through 53 show the defocusing of the main beam as a function of the elevation angle.

Figures 48 - 50 investigate the defocusing of the main beam as a function of the radius of the array. The array is designed to focus the main beam at a fixed elevation of $\theta_0 = 3^\circ$ at 16.383 GHz. By increasing the frequency to 17.45 GHz and 18.42 GHz, the beams are steered to 9° and 15° , respectively. The result of the steering is that the main beam begins to spread, filling in the nearest nulls. This continues until the nulls, sidelobes, and main beam become one continuous beam as indicated for $\theta_1 = 15^\circ$. As noted previously, the beamwidth is inversely proportional to the radius of the cylinder. Also, the defocusing effect also increases as the radius is increased. This is seen by comparing the three figures for $\theta_1 = 9^\circ$ and $\theta_1 = 15^\circ$.

The design case as noted previously is an array with a radius $R = 12''$. Figures 49, 51, and 52 show the defocusing of the main beam as a function of illumination angle ϕ_{ill} for $R = 12''$. As the illumination increases from 60° to 120° , the defocusing of the main beam also increases. This indicates that the defocusing of the main beam is directly proportional to the illumination sector.

Another possibility for reducing the defocusing effect is to design the system to operate at a frequency which is between the two steering angle frequencies. Since the two steering angles for this array are 3° and 6° respectively, the arithmetic mean is $\theta_0 = 4.5^\circ$. Therefore, the system could be designed to operate at a frequency which would focus the main beam to an elevation of 4.5° . A plot of this information is shown in Figure 53. A comparison of these data shows a decrease in the defocusing of the main beam when the center frequency of operation is chosen as the arithmetic mean frequency. Further information on defocusing is given in the Appendix.

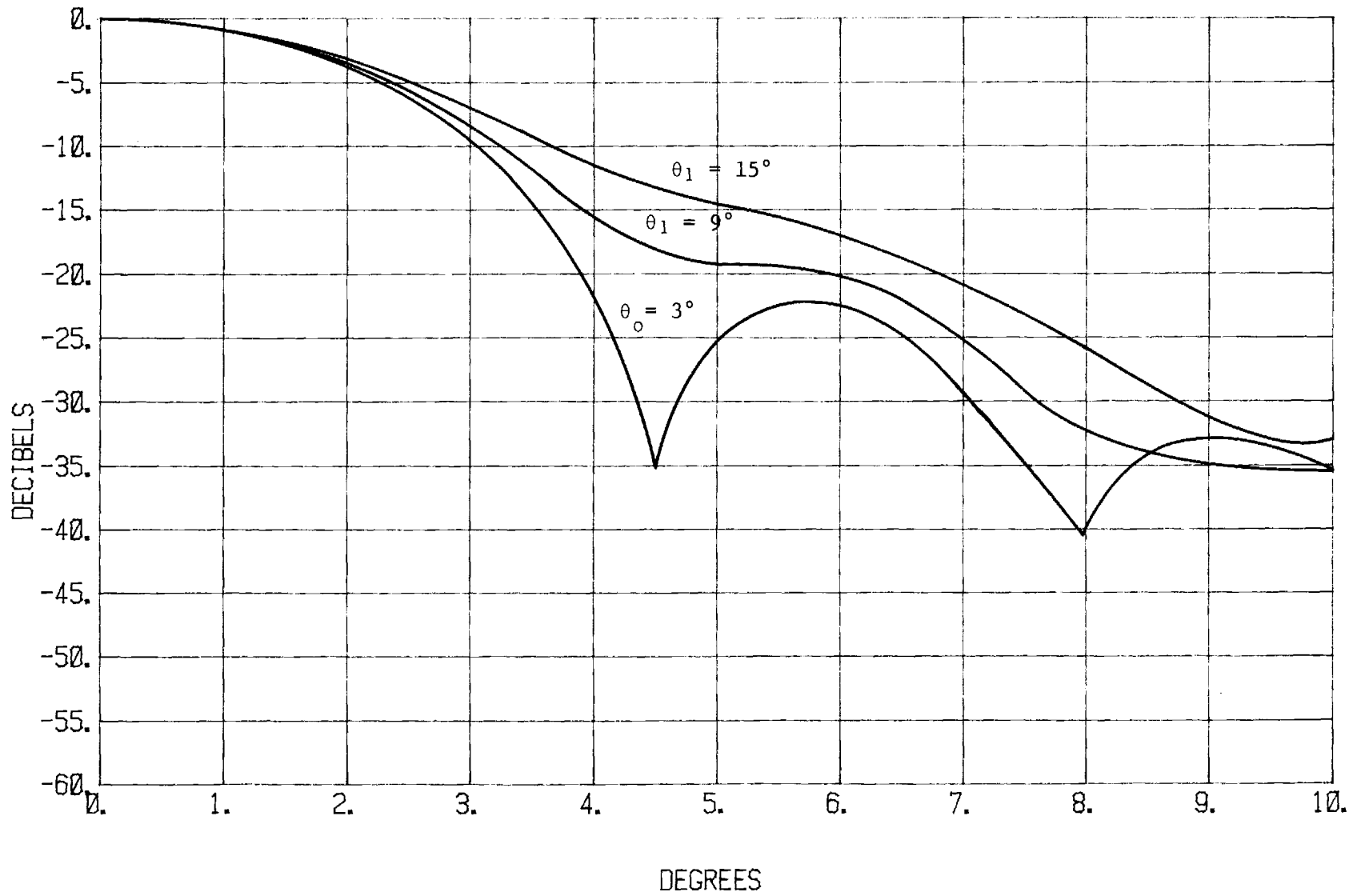


Figure 48. Defocusing of the Main Beam Vs. Steering Angle for $R = 10''$ and $\phi_{ill} = 90^\circ$.

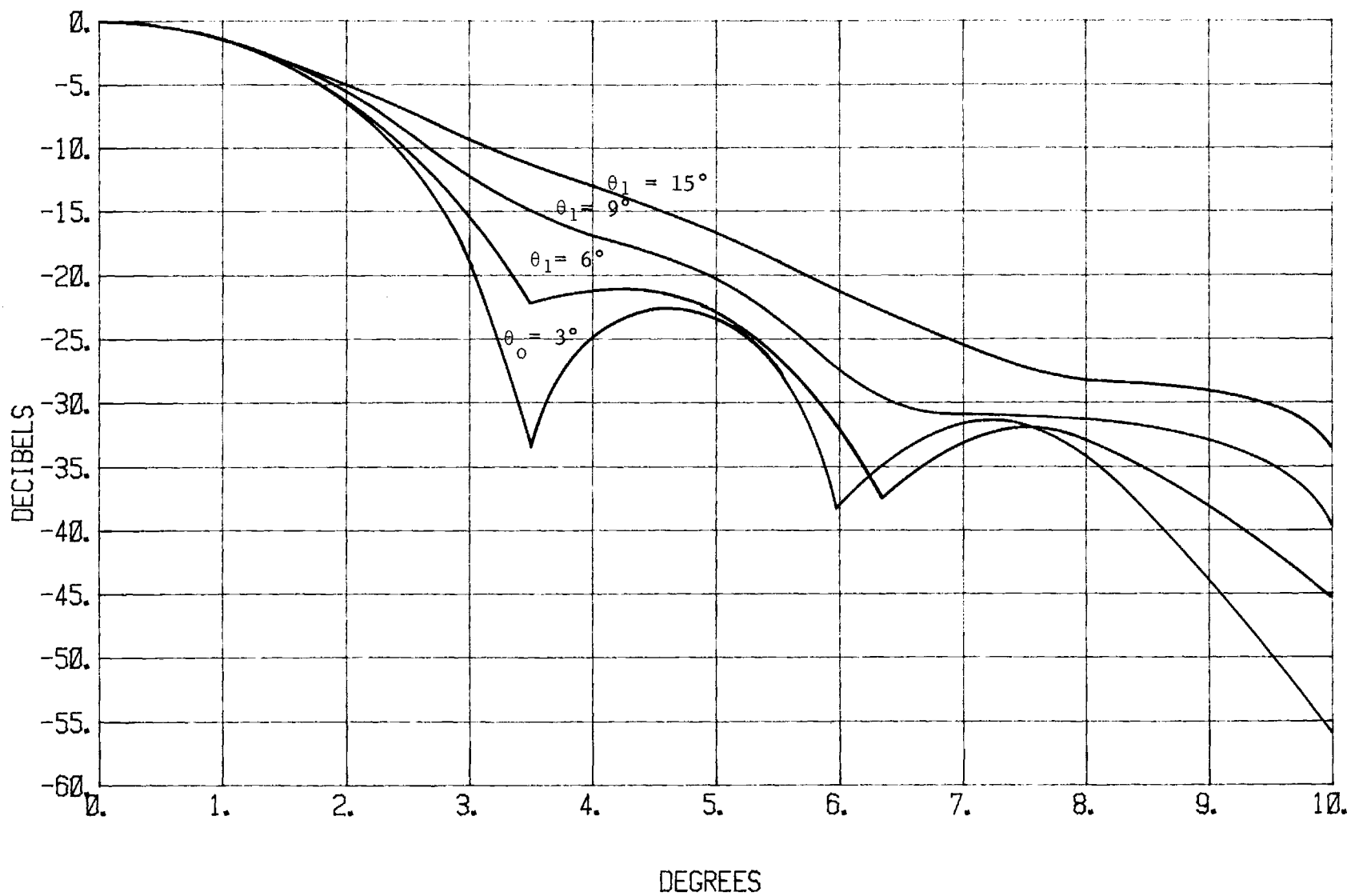


Figure 49. Defocusing of the Main Beam Vs. Steering Angle for $R = 12''$ and $\phi_{i11} = 90^\circ$.

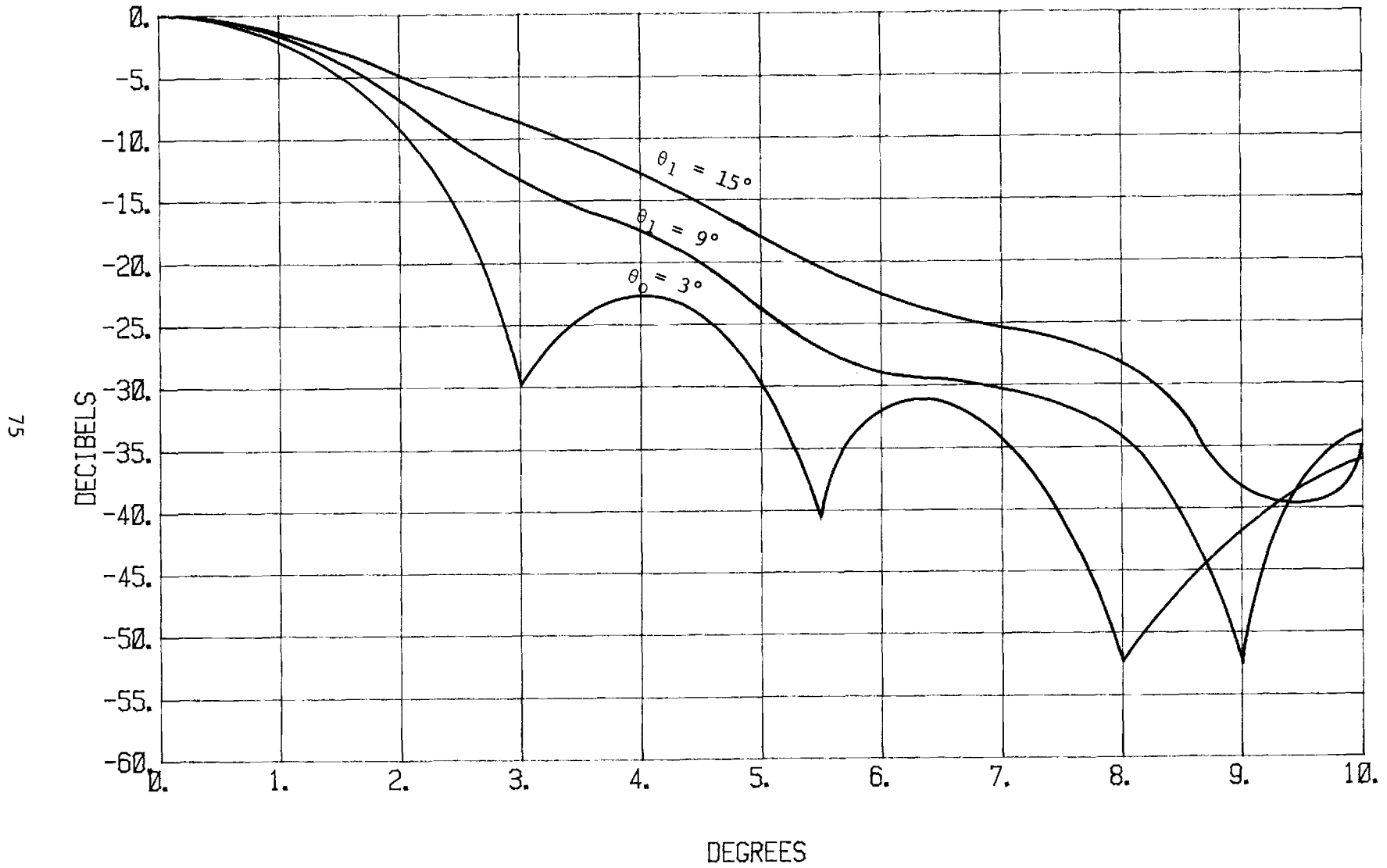


Figure 50. Defocusing of Main Beam Vs. Steering Angle for $R = 14''$ and $\phi_{i11} = 90^\circ$.

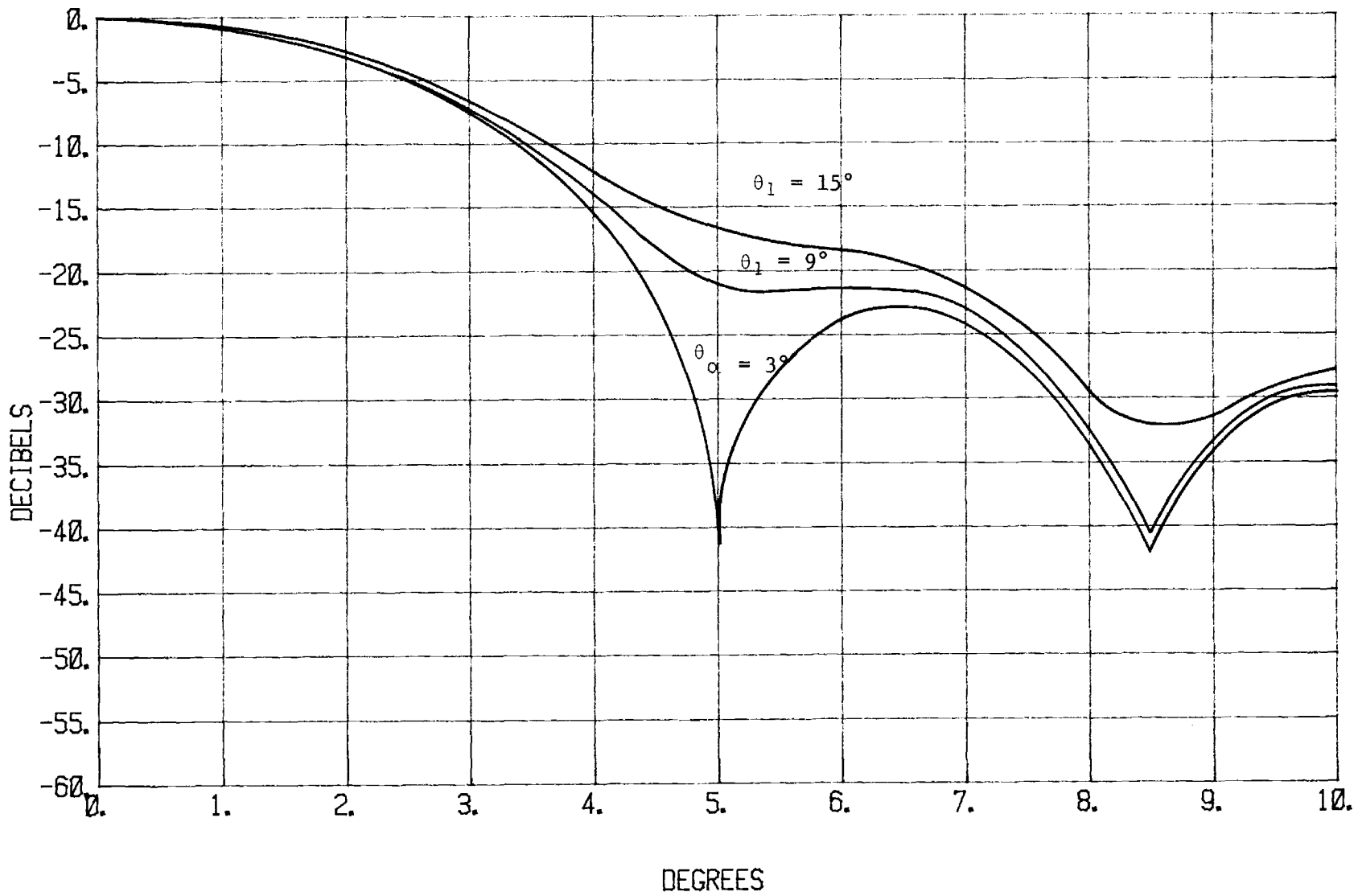


Figure 51. Defocusing of the Main Beam Vs. Steering Angle for $R = 12''$ and $\phi_{111} = 60^\circ$.

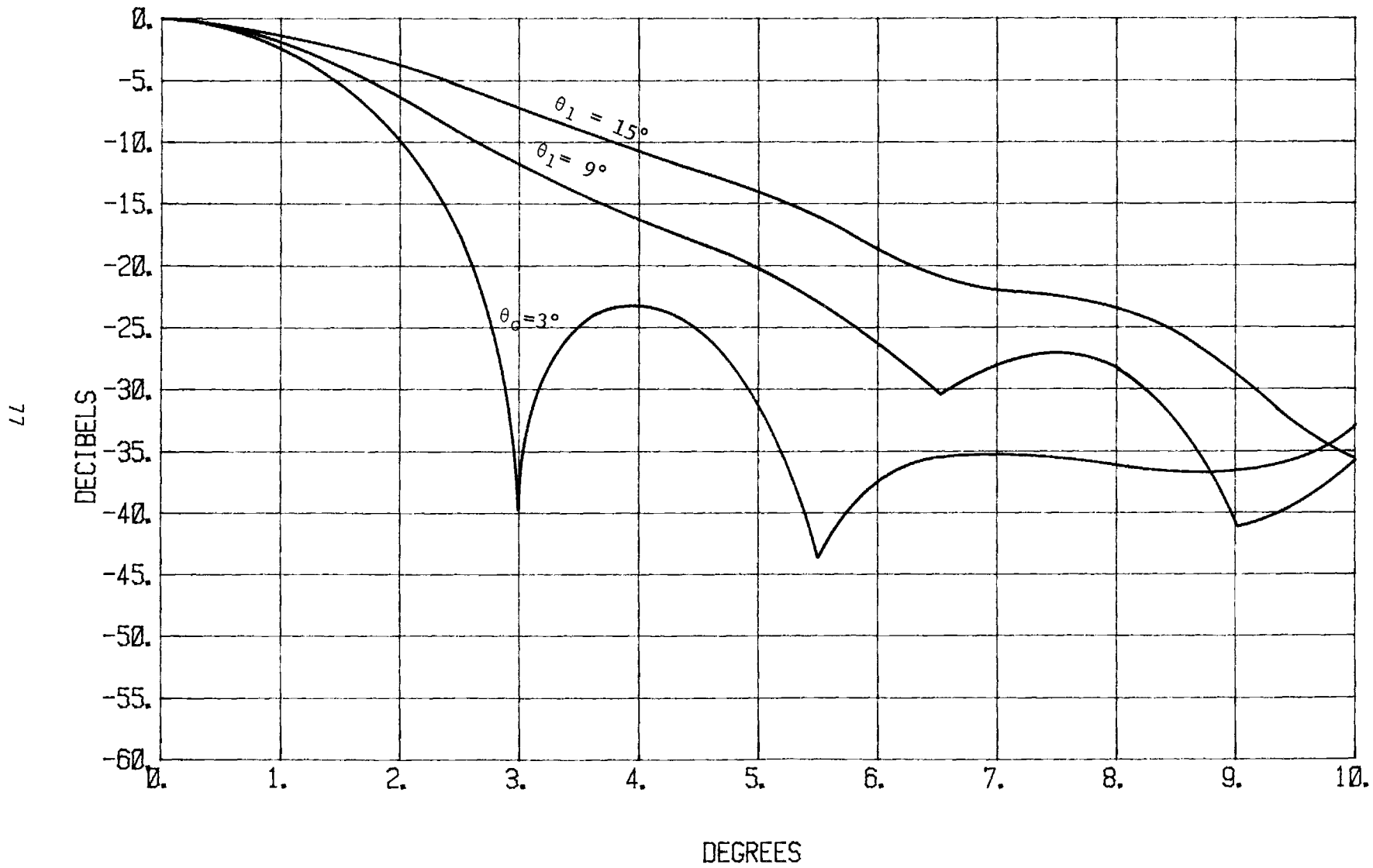


Figure 52. Defocusing of the Main Beam Vs. Steering Angle for $R = 12''$ and $\phi_{i11} = 120^\circ$.

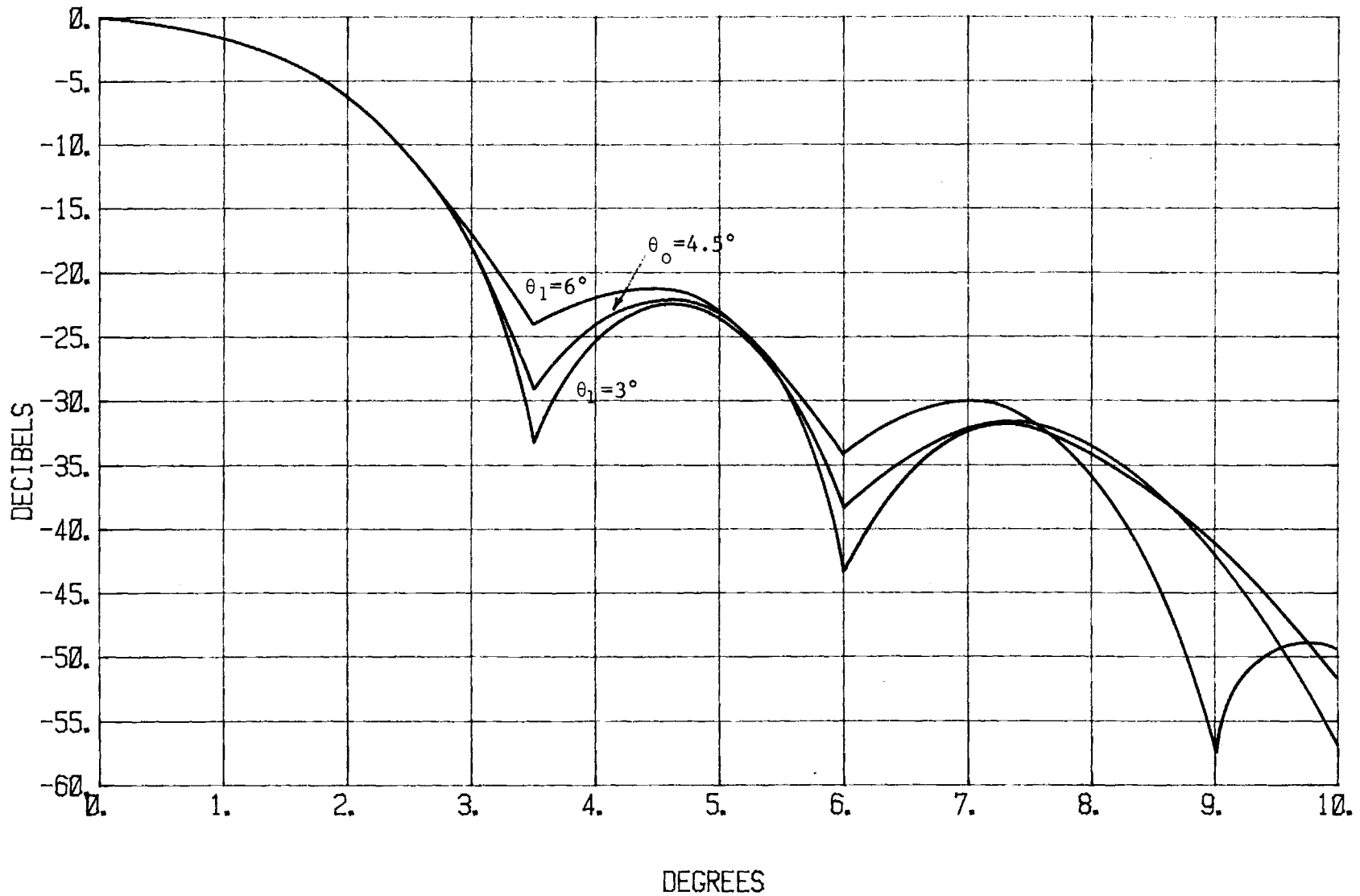


Figure 53. Defocusing of the Main Beam Vs. Steering Angle for $R=12''$ and $\phi_{111} = 90^\circ$.
 Note that $\theta = 4.5^\circ$.

At this point, the array model has been used to investigate all of the problems mentioned in Chapter II-F. The results of the investigation are the design curves shown in Figures 36, 43, and 47. These curves in conjunction with the defocusing information presented in this section provide the necessary information to design cylindrical array antennas with the proper illumination sector, element spacing, and radius to produce far-field patterns with the desired beamwidth and grating lobe levels.

IV. EXPERIMENTAL MEASUREMENTS AND RESULTS

Several portions of the cylindrical array were designed, built and tested during this program. This was done (1) to verify that certain critical components could be built to have satisfactory performance, and (2) to obtain components for building a partial array mock-up which was to be tested during this program. Only breadboards of these components were built and not the final units themselves. The items built were coax-to-waveguide adapters, parallel plate-to-waveguide transitions, and waveguide slotted arrays. The experiments performed and results obtained in the following sections were generated using Ku-band waveguide loaded with the dielectrics shown in Table IV. The dielectric was added to the Ku-band waveguide in order to reduce its cutoff frequency and thus permit operation of the waveguide over the 8 to 12 GHz band (X-band). This frequency range was chosen by EES personnel for two reasons: (1) adequate test equipment was available in this band and (2) a parallel plate feed horn structure which operates in this band was already available from a previous study and could be used to feed the slotted array. The X-band data that was generated during this program can be scaled to Ku-band frequencies for the final design.

A. Coax-to-Waveguide Adapter

Coax-to-waveguide adapters had to be developed during this program for two reasons. First, one possible termination for each waveguide array element is a 50 Ω coaxial load. A coax-to-dielectrically-loaded waveguide adapter is needed in order to couple energy from the dielectrically-loaded waveguide into this load. The second reason involves the measurement of both the tapered dielectric transitions and the dielectrically-loaded waveguide array test sections. In order to test and thereby generate design data, a method is needed to couple energy into each dielectric transition and into each traveling-wave array test section. Again, a coax-to-dielectrically loaded waveguide adapter is required.

A typical adapter test section is shown in Figure 54. The test sections were made by dielectrically loading Ku-band waveguide (0.702 x 0.391 inch O.D.) with the dielectrics shown in Table IV. The adapter

TABLE IV

Dielectrics Used In Loaded Waveguide Measurements

<u>Dielectric Name</u>	<u>Dielectric Constant</u>	<u>Dielectric Loss Tangent</u>
Lexan** Polycarbonate	2.98	0.010
Rexolite 1422** Cross-linked Styrene copolymer	2.53	0.00066
Stycase 35 PE Cross-linked Polystyrene-ethylene	2.5	0.001
Slygard 184* Silicone elastomer	2.75	0.001

*Tests were not performed with this material. It is suggested for possible use in the final array.

**Lexan and Rexolite are registered trade marks.

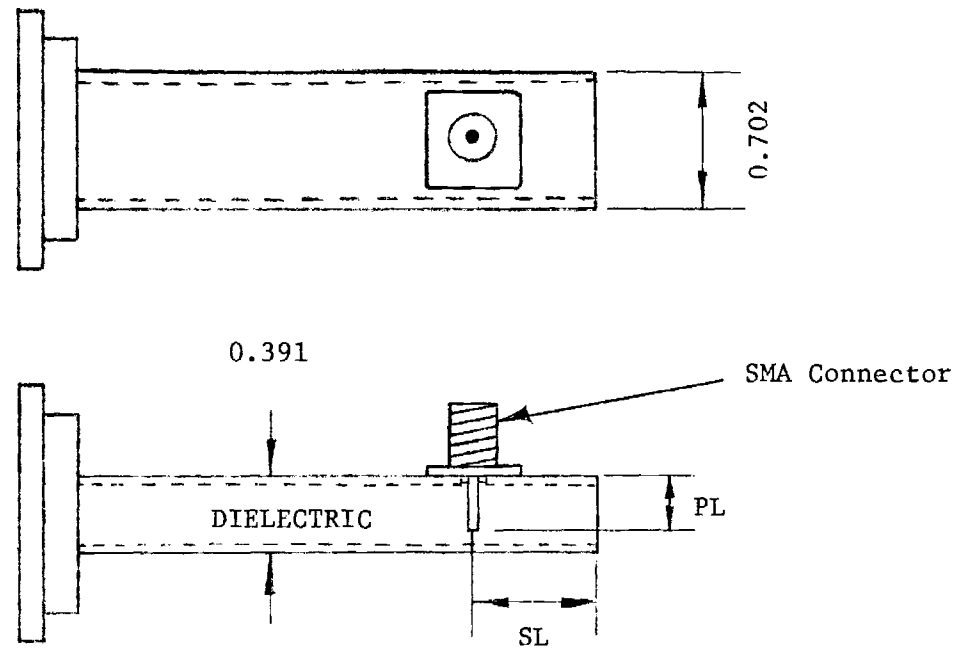


Figure 54. Adapter from SMA Coax-to-Dielectrically Loaded, WR-62 Waveguide.

included a modified OSM 204cc bulkhead connector along with a waveguide mounting flange. Both ends of the waveguide were left open. The flanged end is attached to a load (or another transition test section) and the non-flanged end is shorted. The objective of the design is to determine the dimensions SL and PL so that a good match is obtained. The probe-to-back wall spacing (SL) was varied by machining away the unflanged end of the adapter. A short was introduced by placing electrically conducting tape over the back wall. The probe depth (PL) was varied by drilling a deeper hole in the dielectric and using a longer pin on the OSM connector.

The adapters were tested by measuring the return loss with an H-P Network Analyzer looking into the coaxial input. As the frequency is swept across the band, the return loss is plotted on an X-Y recorder. Various loads were used on the flanged end of the adapter.

In the first series of tests, two identical adapters were made. The two adapters were clamped together (flanged ends) and a 50 Ω coaxial load was placed on the coaxial input of one of the adapters. The other coaxial input was connected to the H-P Network Analyzer where return loss measurements were made as a function of frequency (8 to 12 GHz). A number of tests were run as adjustments to SL and PL in Figure 54 were made in an effort to tune out any mismatches created by the probes. This method however, was not successful since a cavity-like resonance condition was observed when the two adapters were clamped together. The output generated was cyclic in nature (as a function of frequency) and of such magnitude that it made probe tuning almost impossible. A typical return loss versus frequency plot for this geometry is shown in Figure 55. This figure is for non-optimized SL and PL dimensions. For comparison, the return loss plot for 50 Ω load is shown in Figure 56 along with two dielectrically loaded, back-to-back adapters with optimized dimensions. Note that some of the residual VSWR in these measurements is the result of mismatch in the cables and connectors used to connect the analyzer to the device under test.

To eliminate the cavity resonance problem, one of the adapters was removed and replaced with a waveguide load. The loads had to be designed and built in-house since no dielectrically-filled waveguide loads were commercially available. Three different loads were designed and built.

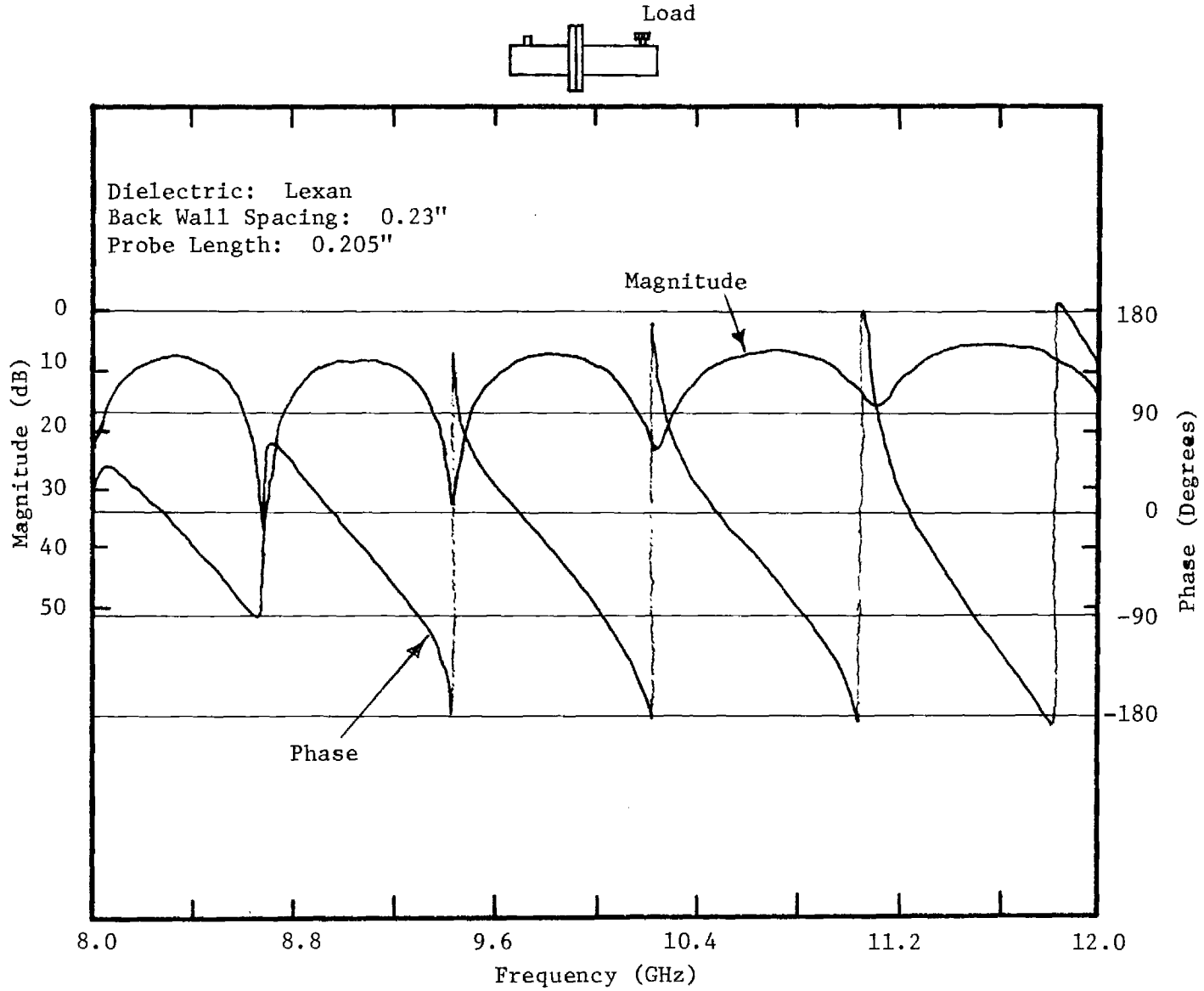


Figure 55. Return Loss of a Lexan Filled Adapter with SL = 0.23" and PL = 0.205"

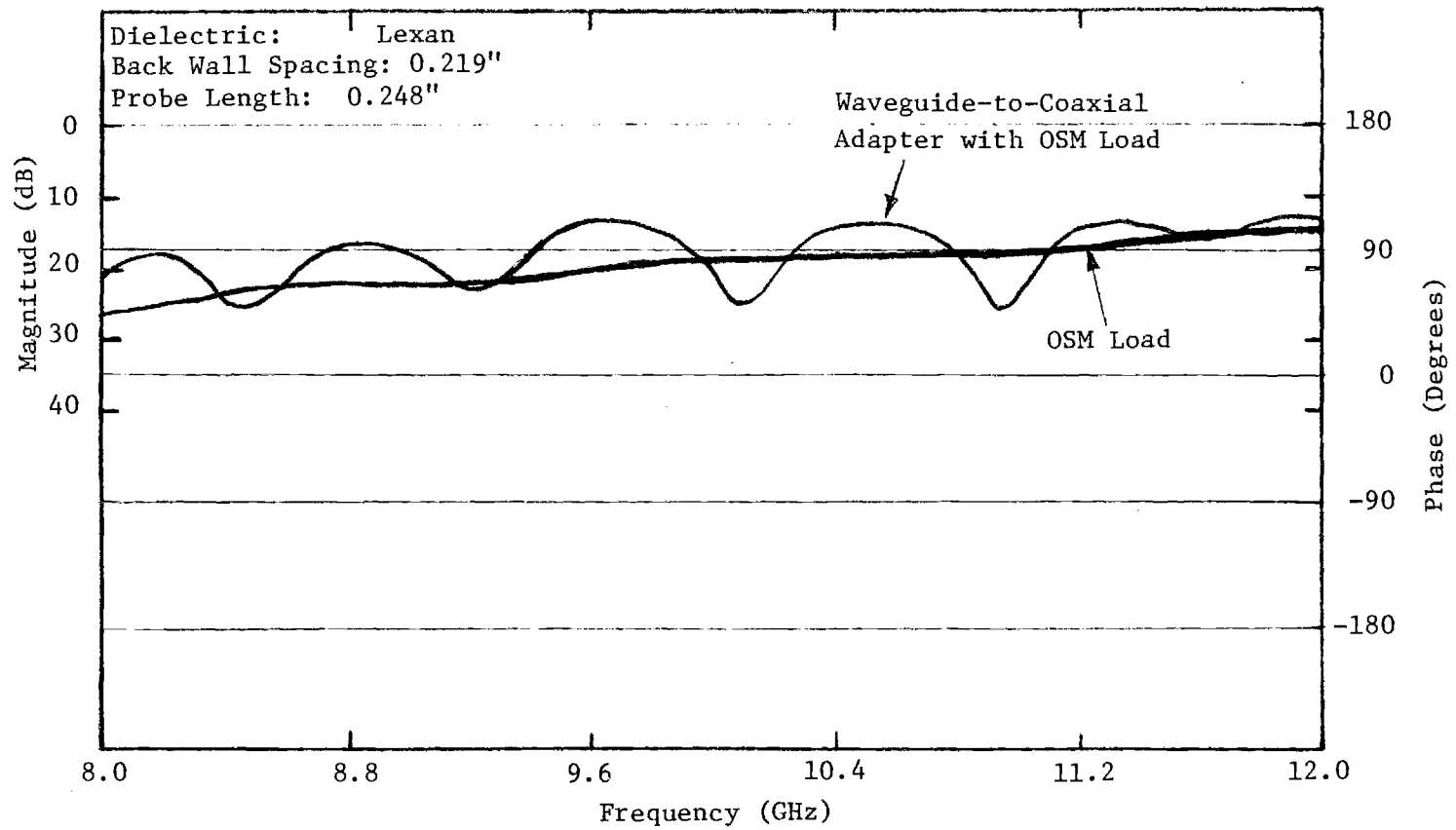


Figure 56. A Measured Return Loss of Two Dielectrically Loaded Adapters Connected Together With an OSM Load on One and the OSM Load by Itself.

Two of these are shown in Figure 57. These loads were fabricated by machining both a carbon loaded material and a dielectric and fitting the two together. Load A in Figure 57 was made using Lexan and Rexolite as the dielectric while Load B was made using only Lexan. The third load was built by pouring stycast into a standard commercially available Ku-band load.

A second series of tests was performed on the adapters using the above waveguide loads. The data from this series of tests were much easier to interpret. Typical results are shown in Figure 58. A Smith chart plot as a function of frequency is shown in Figure 59. Figure 60 is the response of a commercially available X-band adapter connected to a commercially available load. The commercial unit has a best-case return loss of 20 dB (1.22 VSWR). The best case for the Lexan adapter was 18 dB (1.3 VSWR). The Lexan and Rexolite adapters were slightly worse than the standard X-band unit; however, these results are considered very good since the commercial adapter was not dielectrically loaded while the EES units were.

The performance of the Stycast adapters was much worse than that of either the Lexan or Rexolite adapters. The differences here were due to a number of factors. First, the filling of a commercially available Ku-band coax-to-waveguide adapter with a dielectric changed its impedance from its originally designed value. Secondly, it was very difficult to completely clear the Stycast of air bubbles. And finally, the Stycast had a tendency to shrink away from the waveguide walls. These effects produced multiple reflections causing the degradation seen in the performance of the Stycast adapters.

The data for each dielectric were analyzed and three graphs were generated to show the effects of probe length and back wall placement on the adapter performance. Figures 61 - 63 present this information for Stycast, Rexolite, and Lexan respectively. These data were generated by averaging the data collected from two different transitions, both made of the same dielectric.

From the Lexan and Rexolite data it was determined that the optimum back wall distance from the center of the probe was $0.96 \frac{\lambda_g}{4}$ where λ_g is the guide wavelength in the dielectric. The optimum probe length from the inside guide wall was 0.61b for Lexan and 0.68b for Rexolite, where b is inside height of the waveguide. It has thus been shown that

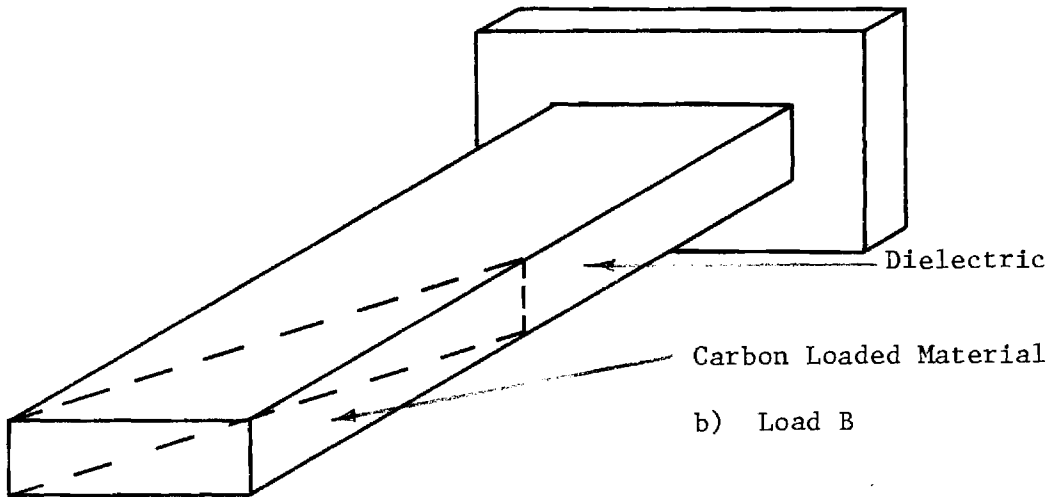
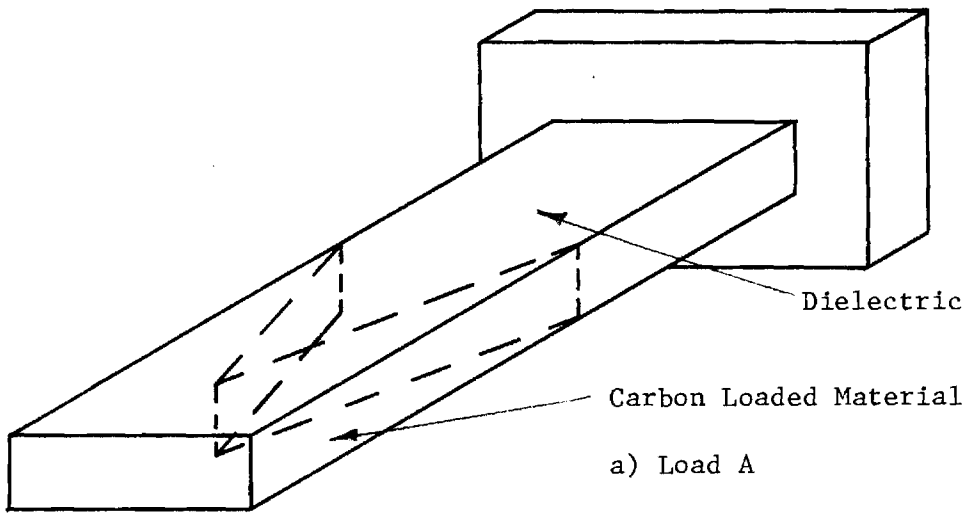


Figure 57. Dielectrically Loaded, Waveguide Terminations.

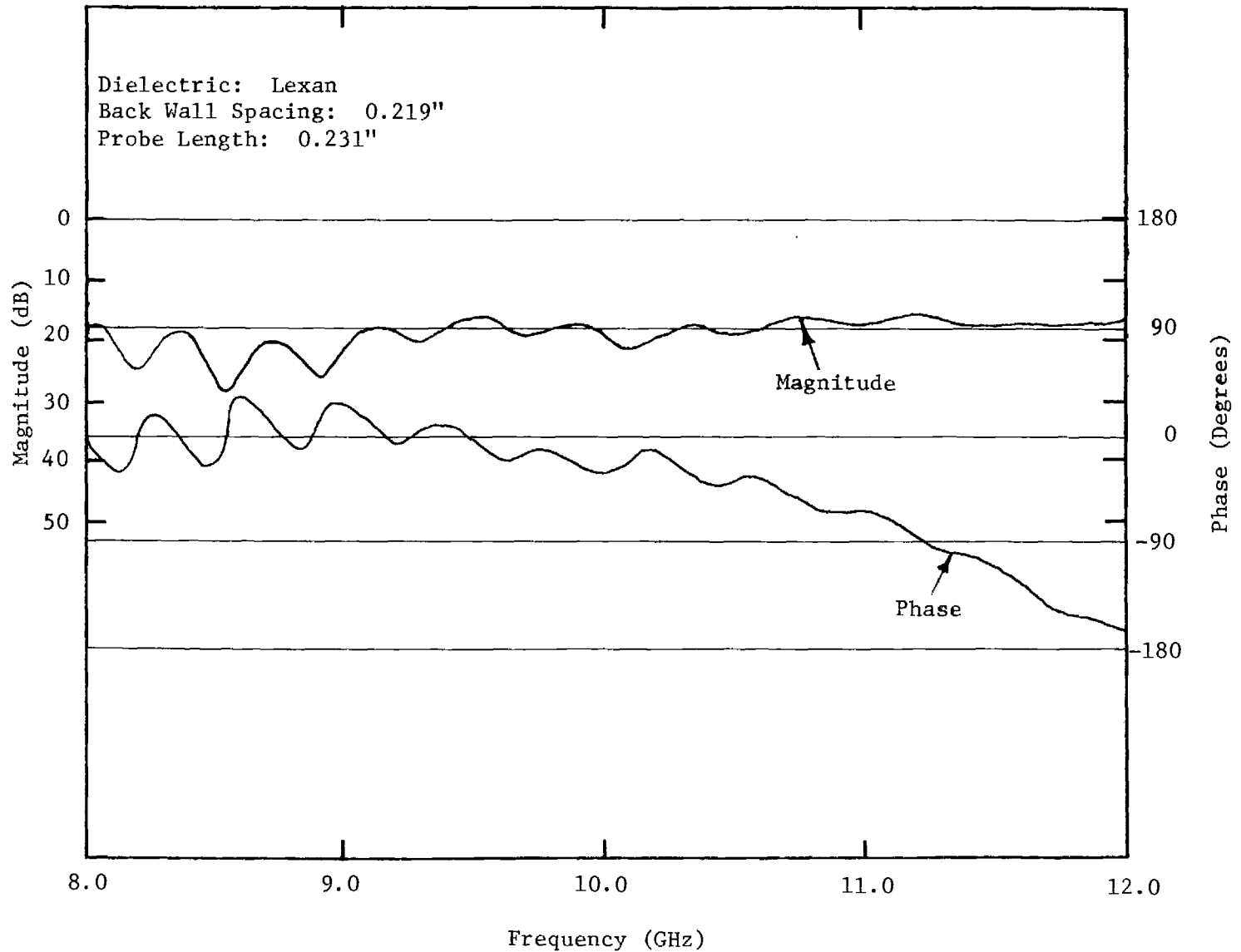
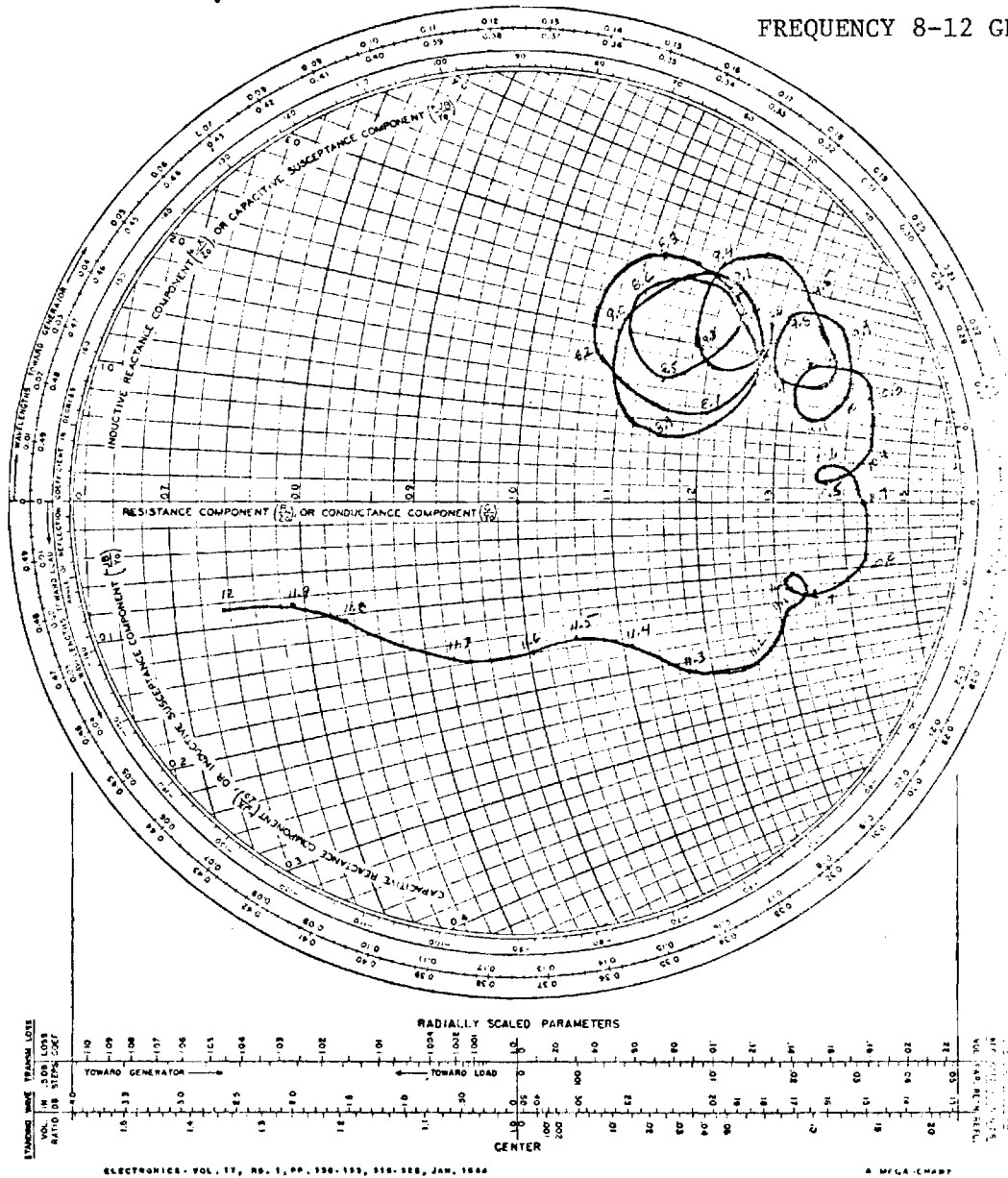


Figure 58. Return Loss of Lexan Adapter with Lexan Waveguide Load.

NAME	TITLE <i>Lexan W/L = .219 PL = .231 #4</i>	DWG. NO.
SMITH CHART FORM 02 3PR (2-49)	<i>General Waveguide Transition</i> RAY ELECTRIC COMPANY, PINE BROOK, N.J. © 1949 PRINTED IN USA	DATE <i>2-12-79</i>

Frang End IMPEDANCE OR ADMITTANCE COORDINATES

FREQUENCY 8-12 GHz



Note: Numbers on curve are frequencies in GHz
 Figure 59. Smith Chart Plot of Impedance of Lexan Coax-to-Waveguide Adapter as a Function of Frequency for SL = 0.219 Inches and PL = 0.231 Inches.

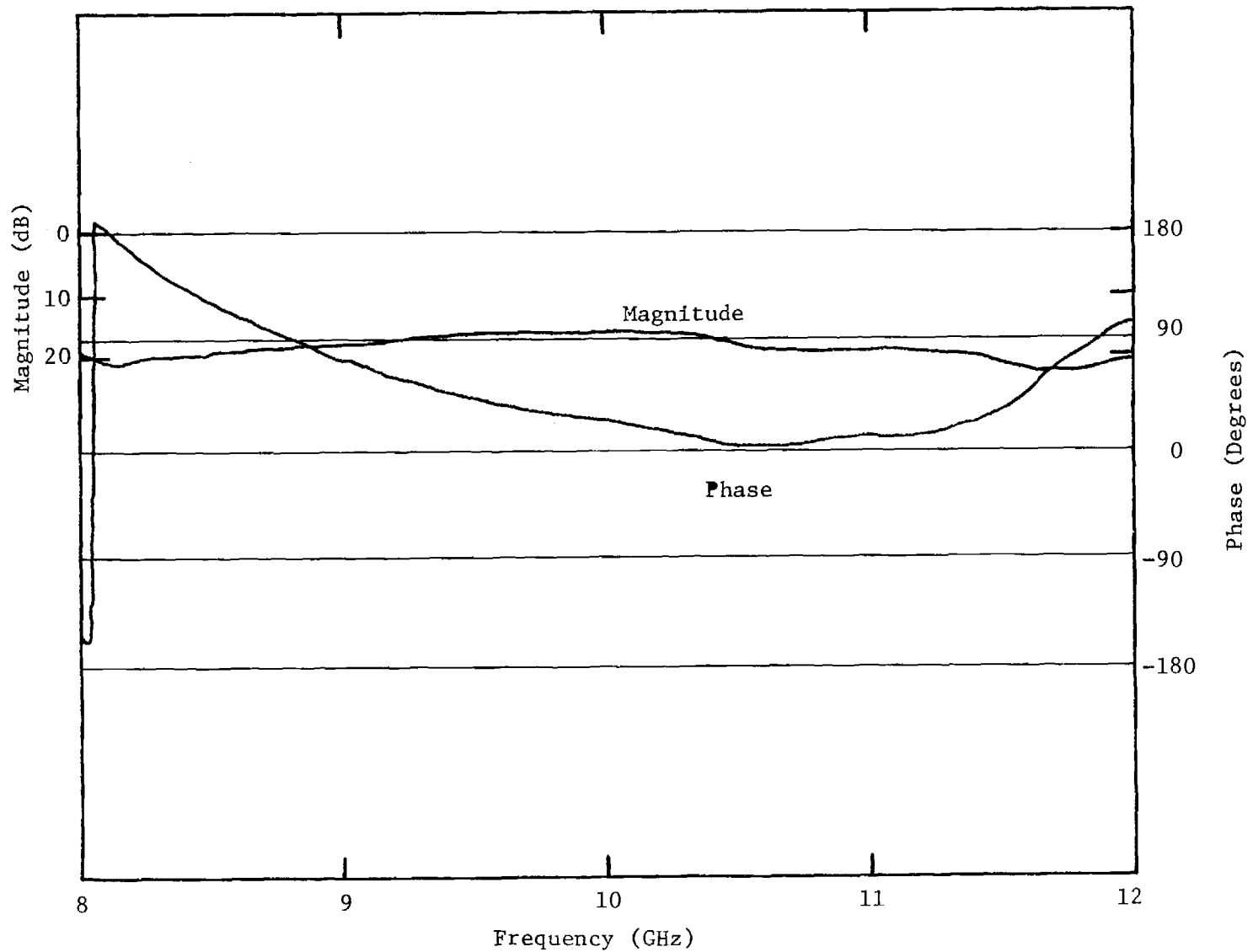


Figure 60. Return Loss of X-Band Waveguide-to-SMA Adapter with X-Band Waveguide Load.

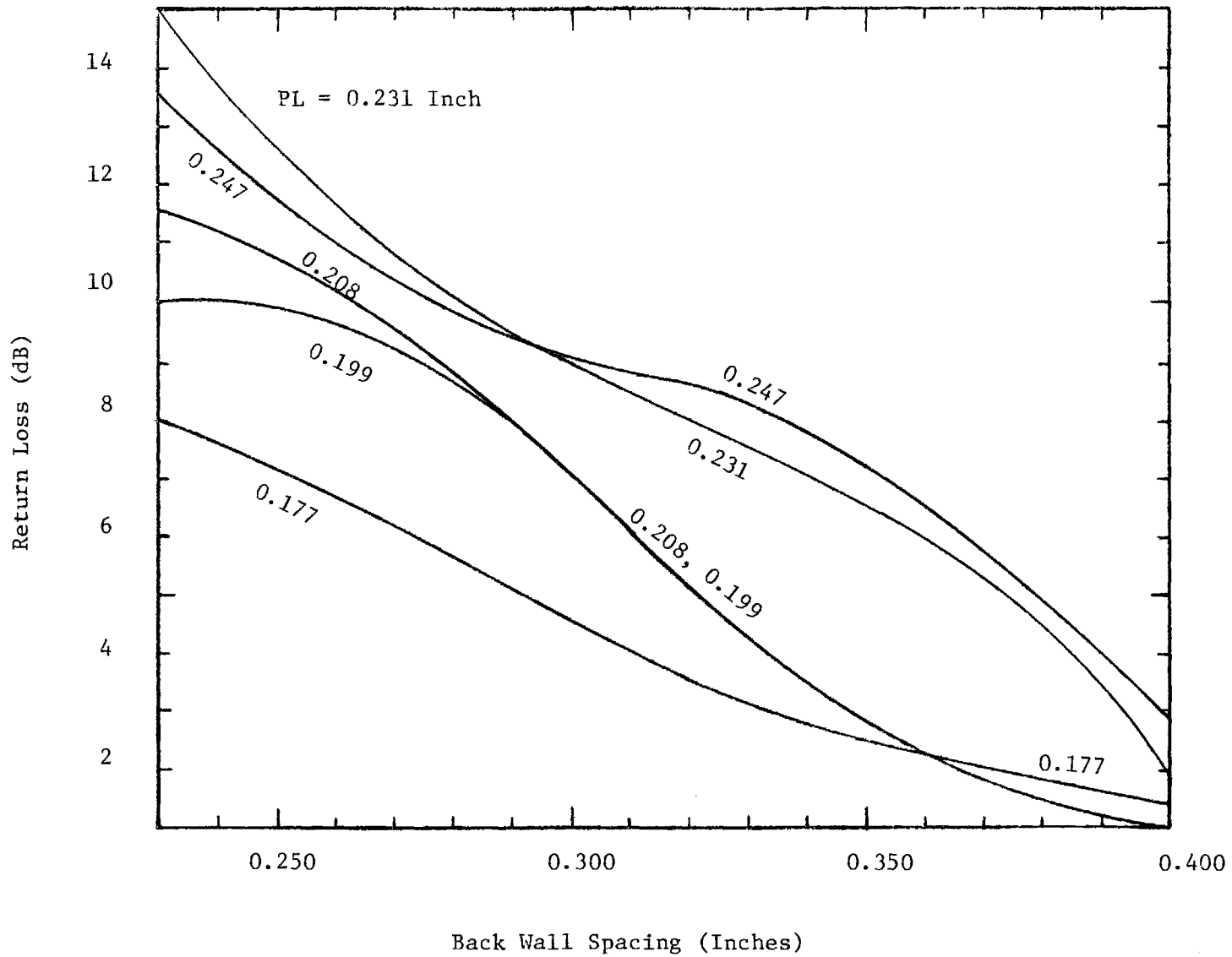


Figure 61. Return Loss of Adapter as a Function of Back Wall Spacing (SL) and Probe Length (PL) for Stycast Loading.

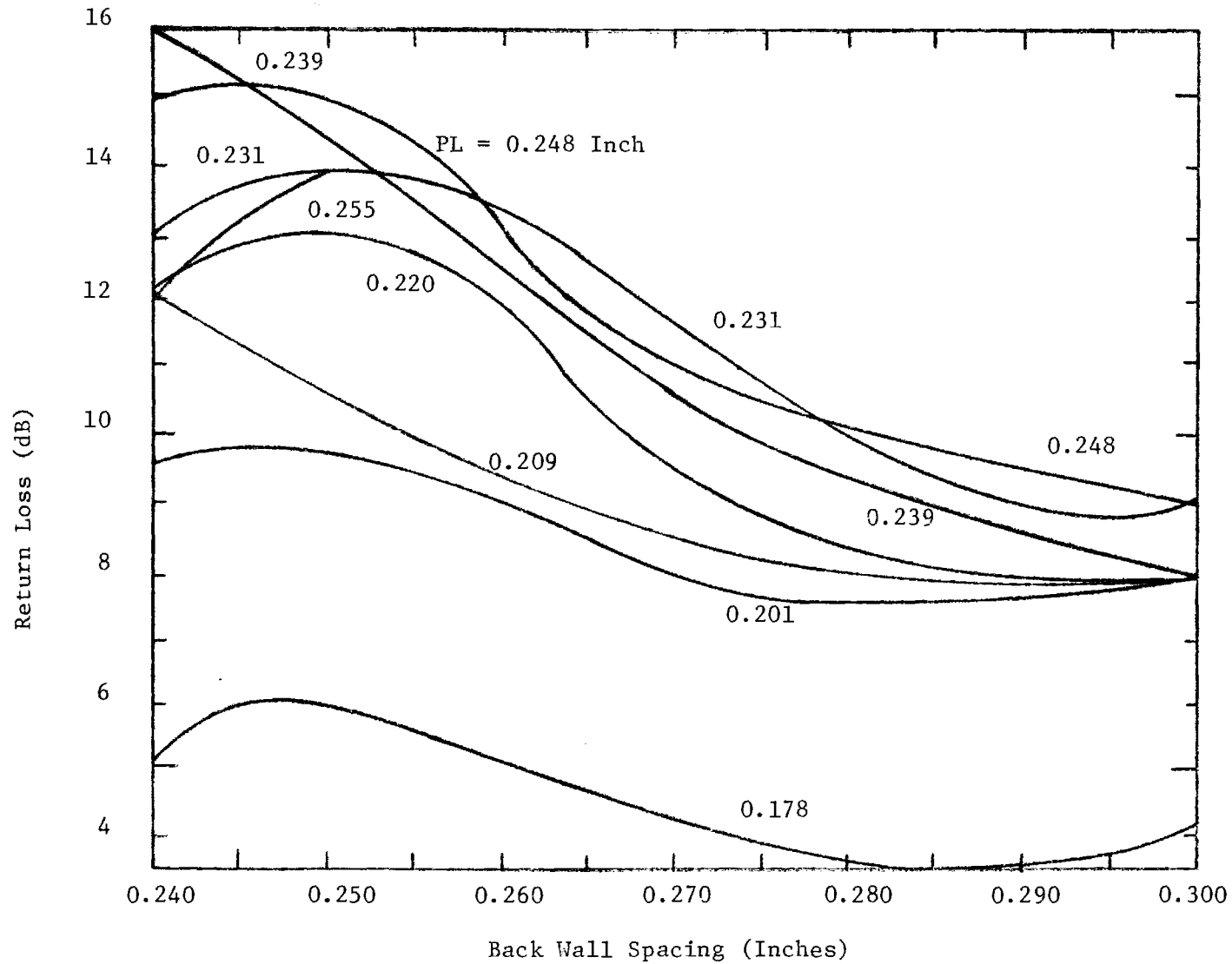


Figure 62. Return Loss of Adapter as a Function of Back Wall Spacing (SL) and Probe Length (PL) for Rexolite Loading.

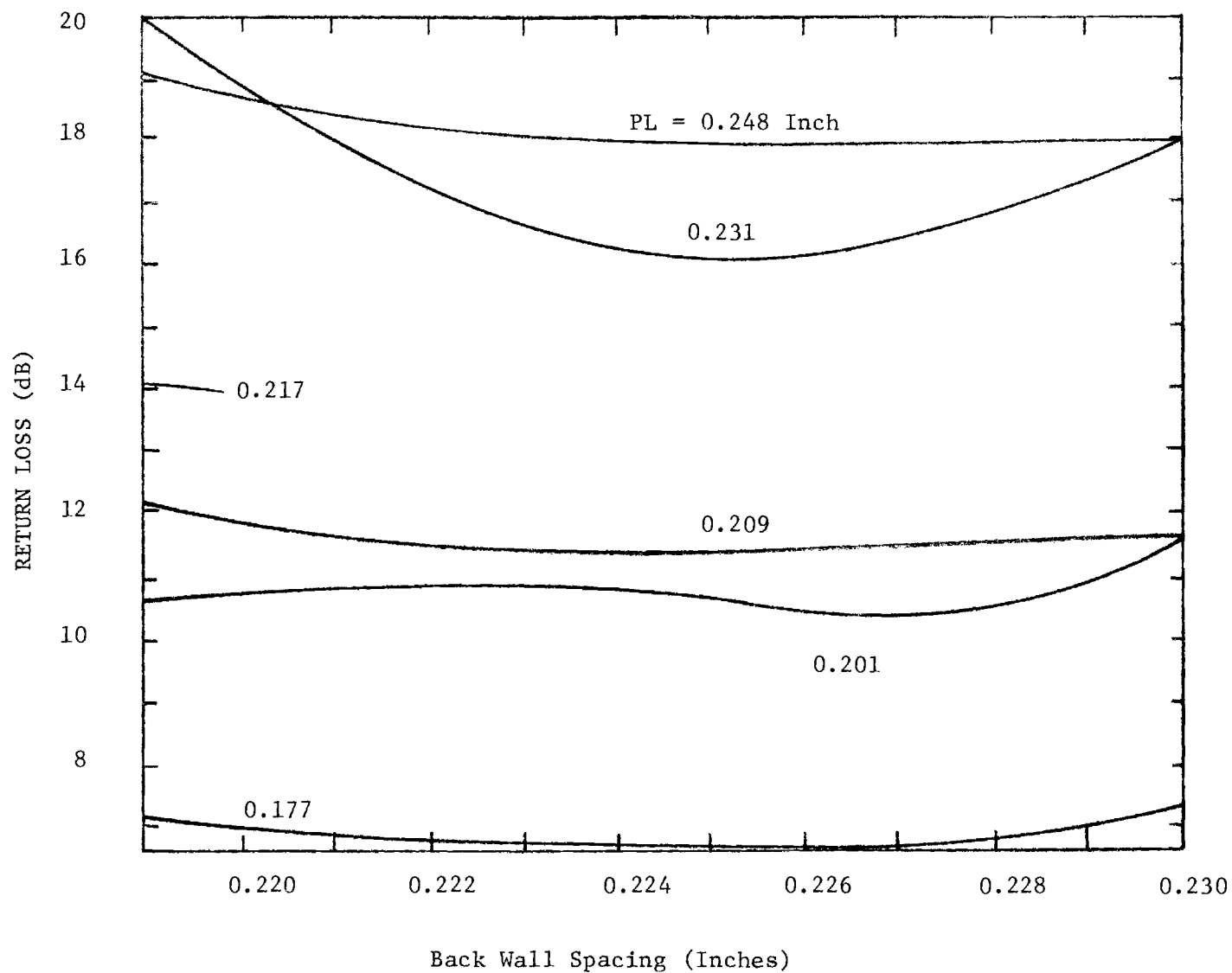


Figure 63. Return Loss of Adapter As a Function of Back Wall Spacing (SL) and Probe Length (PL) for Lexan Loading.

it is possible to make coax-to-dielectric loaded waveguide adapters having good performance. Still better performance might be obtained by varying the probe diameter. Further investigation in this area should be performed.

It was observed from these and other measurements that the best data were obtained from machined dielectrics inserted in the waveguide. For short sections of waveguide, the machining of the dielectric works quite well. However, it is difficult to insert long pieces of dielectric into waveguides without appreciable air gaps at the walls being present. Some of the pourable dielectrics EES used had problems with shrinking and air bubbles. From a fabrication standpoint, however, the pourable material is much easier to work with. For this reason, a pourable material called Silicone Elastomer SLYGARD 184 will be considered for the final configuration. Air bubbles were not present in test samples made by EES, using this material. Its characteristics are shown in Table IV.

B. Parallel Plate-to-Waveguide Transition

One of the key design items for the antenna is the selection of a method of coupling energy from the parallel plate region of the sectoral horn into each of the waveguides in the circular array. This involves the transition of energy from the TEM mode in the parallel plate region to the TE_{10} mode in the waveguide. As mentioned previously, there are a number of ways to achieve this.

Probe transitions are one possibility. The energy could be coupled out of the parallel plate region via coaxial probes and then through cables to another set of coaxial probes, one of which is located in each waveguide. This arrangement requires a large number of parts which makes the array more complex and expensive and less reliable. Previous experience has shown this method to be less than satisfactory for this application.

Another possibility, and the one recommended here, is the use of a dielectric transition. The dielectric transition is produced by extending the dielectric that fills the waveguides into the parallel plate region of the sectoral horn. Through proper design, energy can be efficiently coupled from the horn into the dielectric and then directly into the waveguide. Several transition test sections were built to determine optimum dimensions for such a device.

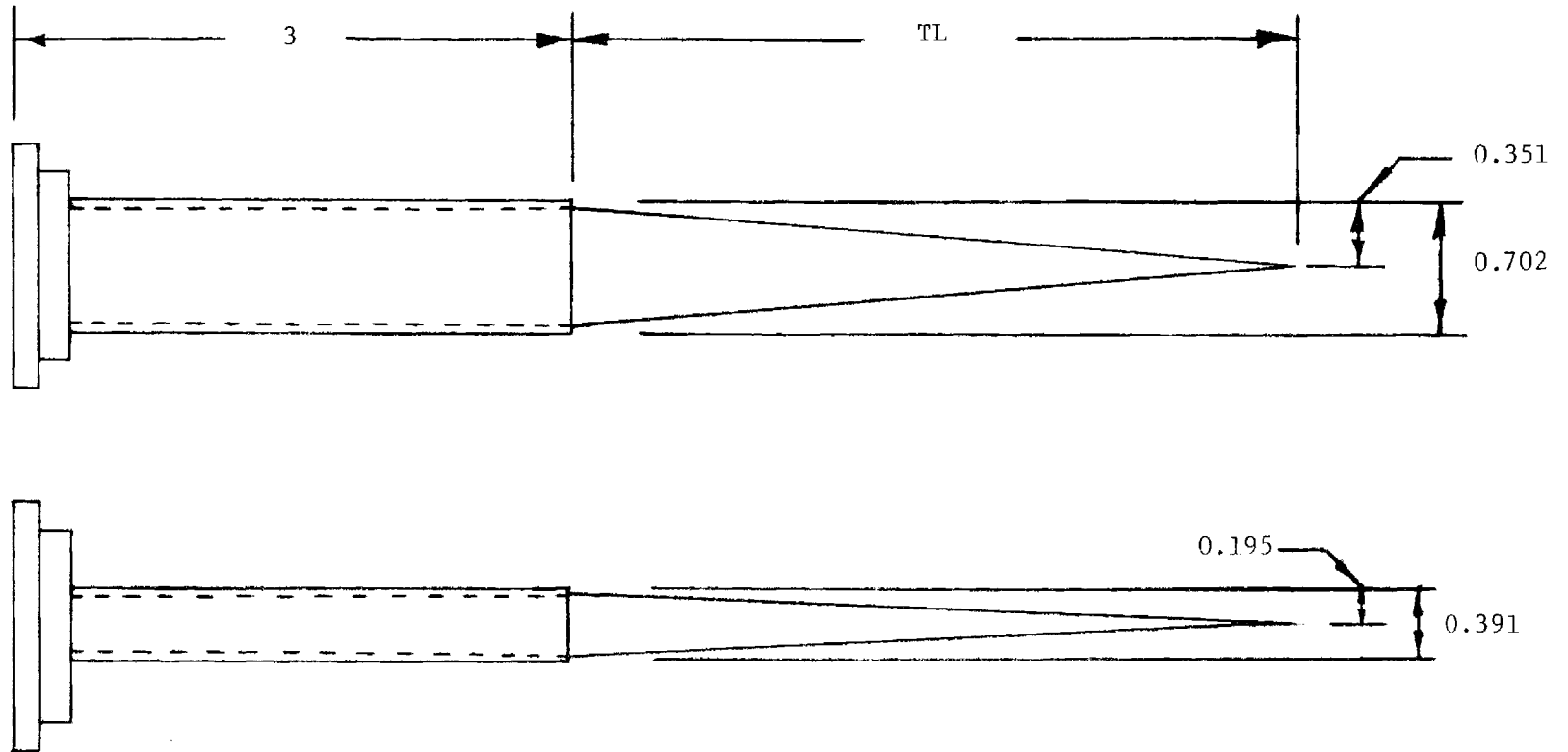
Figures 64 - 66 show the different types of transitions which were investigated. The long taper transitions of Figure 64 and 65 were made using Lexan. The rectangular transitions shown in Figure 66 were made using both Lexan and Rexolite. The transition shown in Figure 66 was not measured versus length due to a lack of time.

The coax-to-dielectrically loaded waveguide adapters discussed in the preceding section were used to couple energy into the transitions. The dielectric transitions were mounted between the parallel plates as shown in Figure 67. Absorber was placed between the parallel plates at the end opposite the transition test sections to reduce reflections. The two side elements shown in Figure 67 were not present for the tests on individual transitions.

The long tapered transitions were measured first. Each transition was tested, shortened, and retested to determine the effect of length on the return loss. Figure 68 is a plot of a typical data run. Changing the length of the sharp pointed tapered sections was difficult since shortening also meant retapering if a sharp point was to be maintained. Because of this difficulty only six measurements were made using the long tapered sections. These results are shown in Figure 69.

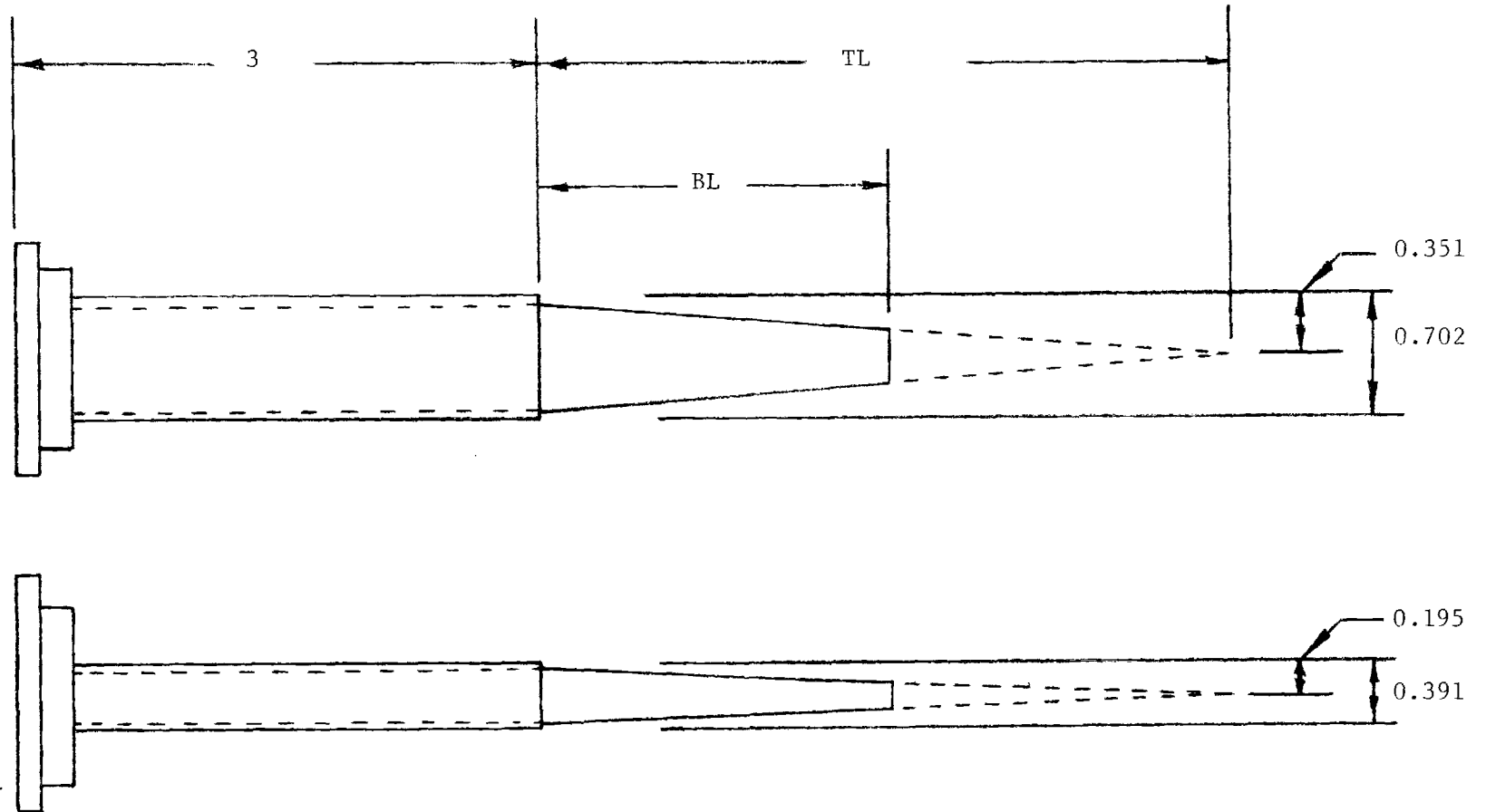
The blunt-tip tapered sections (Figure 65) were much easier to modify in length. These were modified by milling the end of the dielectric. Since the end was already flat, the slope of the taper was not changed. A plot of return loss versus length (BL) is shown in Figure 69. From these data it is evident that the longer taper has better characteristics. However, optimum lengths exist which produce good return loss even for short taper length.

Tests were next run to determine the magnitude of mutual coupling effects produced by adjacent transition sections. First, a single sharp transition was placed between the parallel plates and its return loss measured. The results of this measurement is shown in Figure 70. Next, three sharp transition sections were placed side by side as shown in Figure 67 and the return loss of the center one measured. The two outside transitions were not terminated due to physical clearance problems. The results of this measurement is shown in Figure 71. Comparing Figures 70 and 71 indicates that very little change occurs when multiple sections are added. As an additional check, a short was placed across the output



Note: All dimensions in inches

Figure 64. Pyramidally Shaped, Dielectric Transition From Dielectrically-Loaded WR-62 Waveguide to Air-Filled Parallel Plates.



Note: All dimensions in inches

Figure 65. Blunt Tip, Pyramidally Shaped, Dielectric Transition From Dielectrically Loaded WR-62 Waveguide to Air-Filled Parallel Plates.

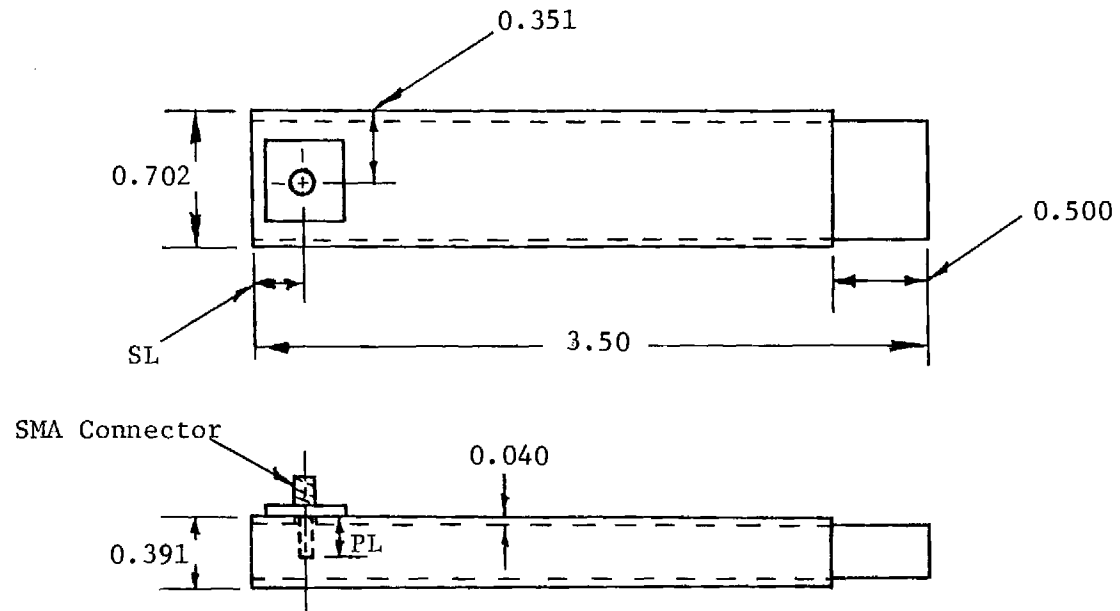


Figure 66. Blunt End Transition from Dielectrically Loaded WR-62 Waveguide to Air-Filled Parallel Plates.

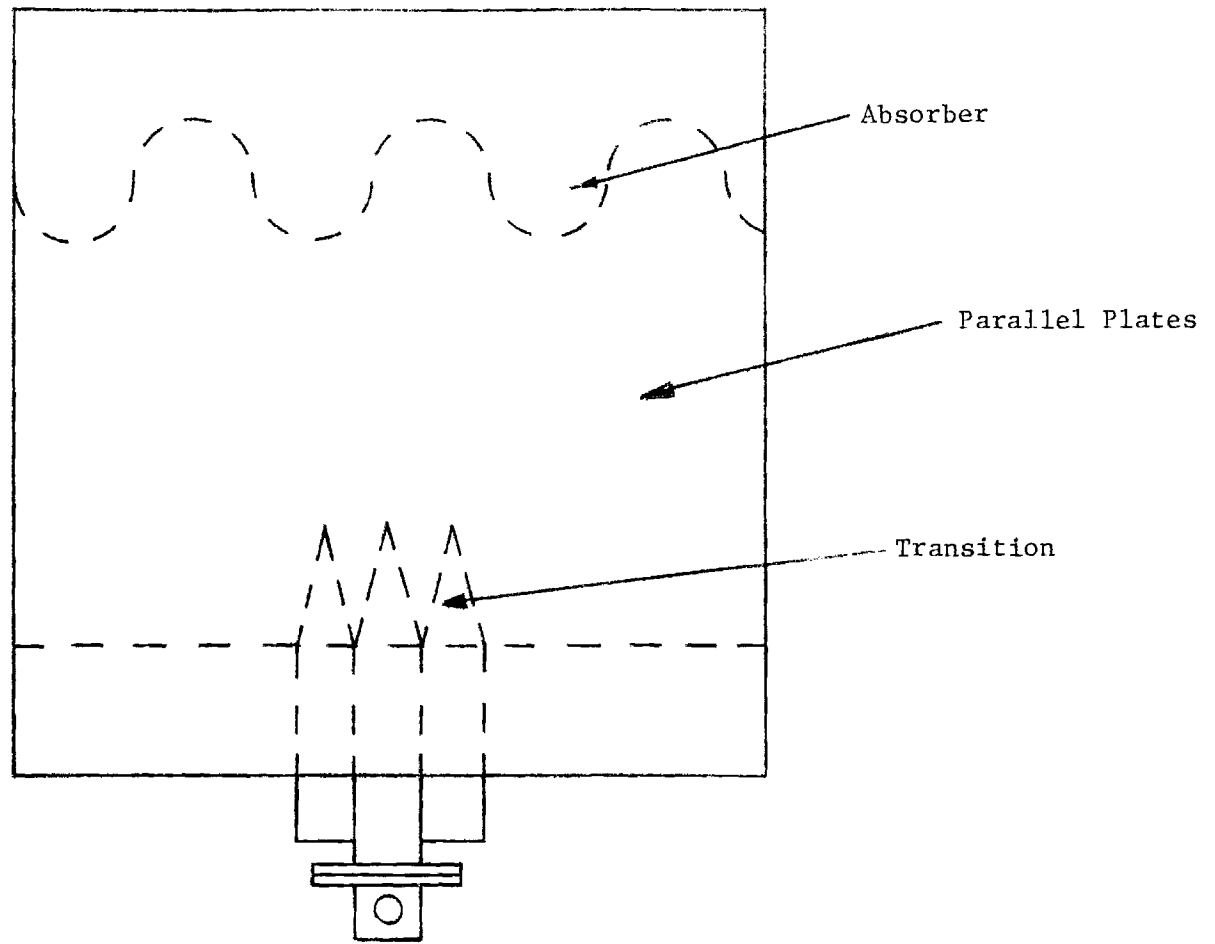


Figure 67. Configuration for Mutual Coupling Tests of Transitions Looking into Parallel Plates.

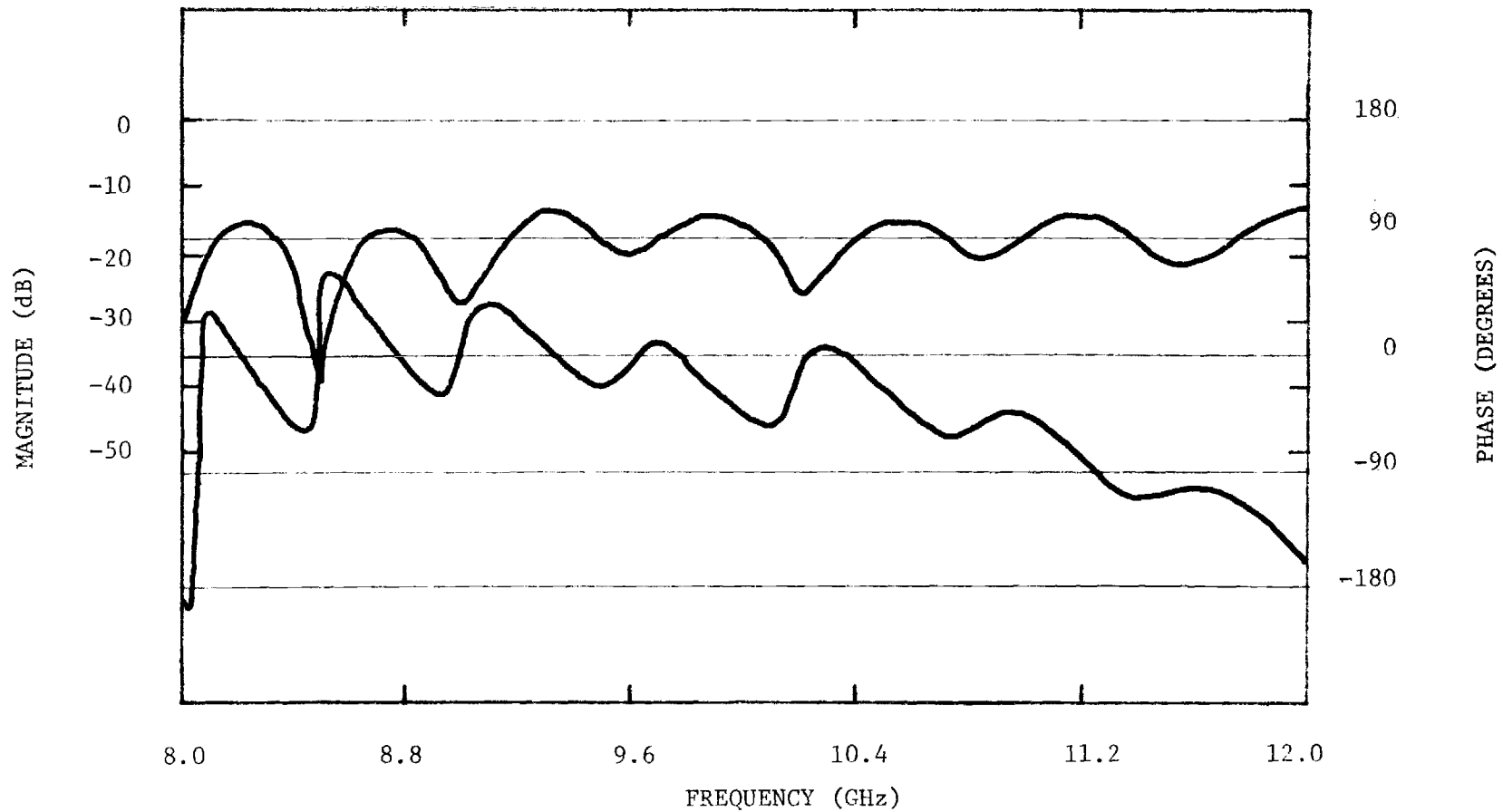


Figure 68. Return Loss From Coax-to-Waveguide Adapter and Pyramidally Shaped, Dielectric Transition in Parallel Plates with TL = 3.93 Inches. Dielectric is Lexan.

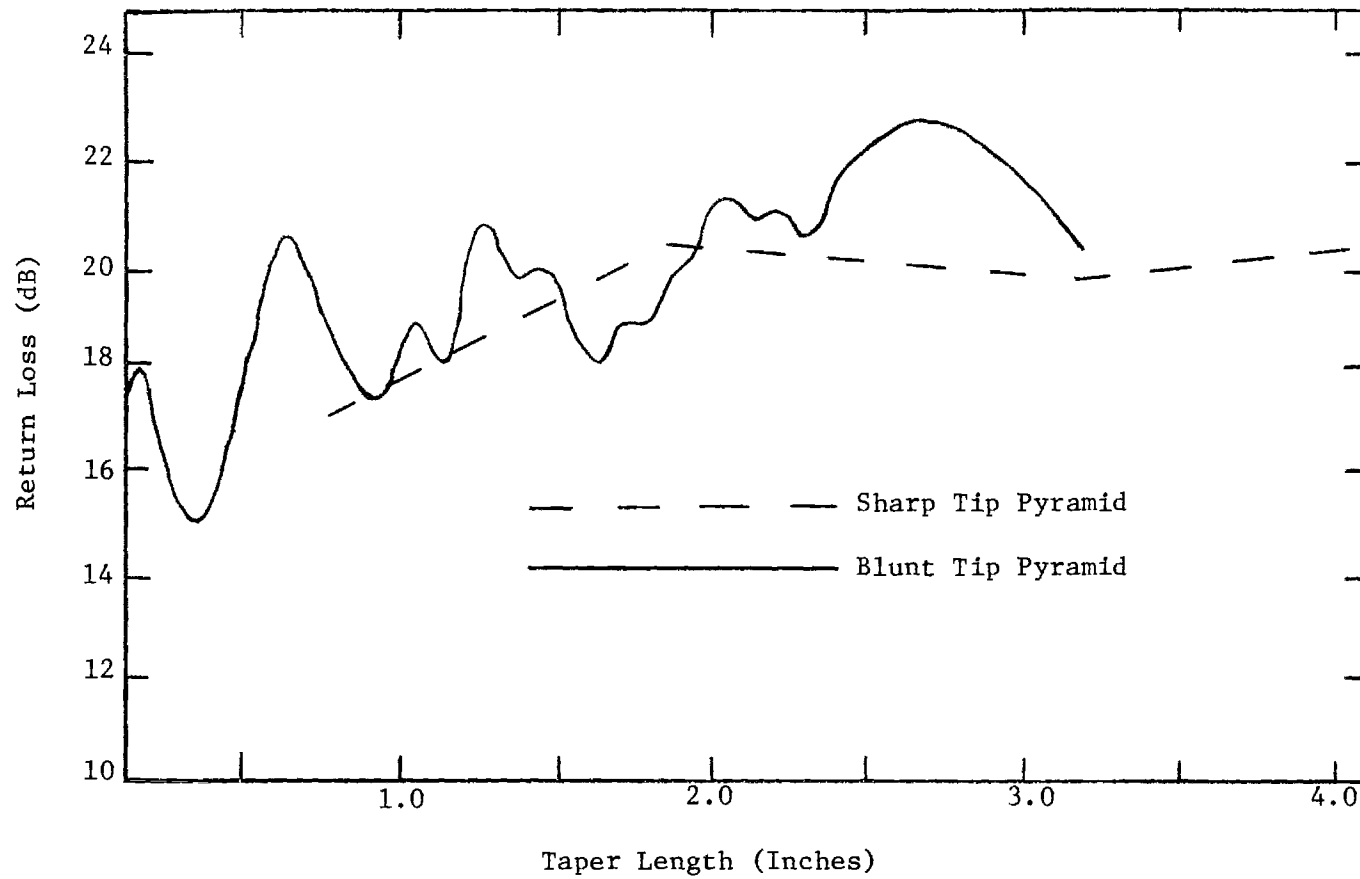


Figure 69. Return Loss Vs. Taper Length TL for Sharp Tip and BL for Blunt Tip Pyramidally Shaped Transitions.

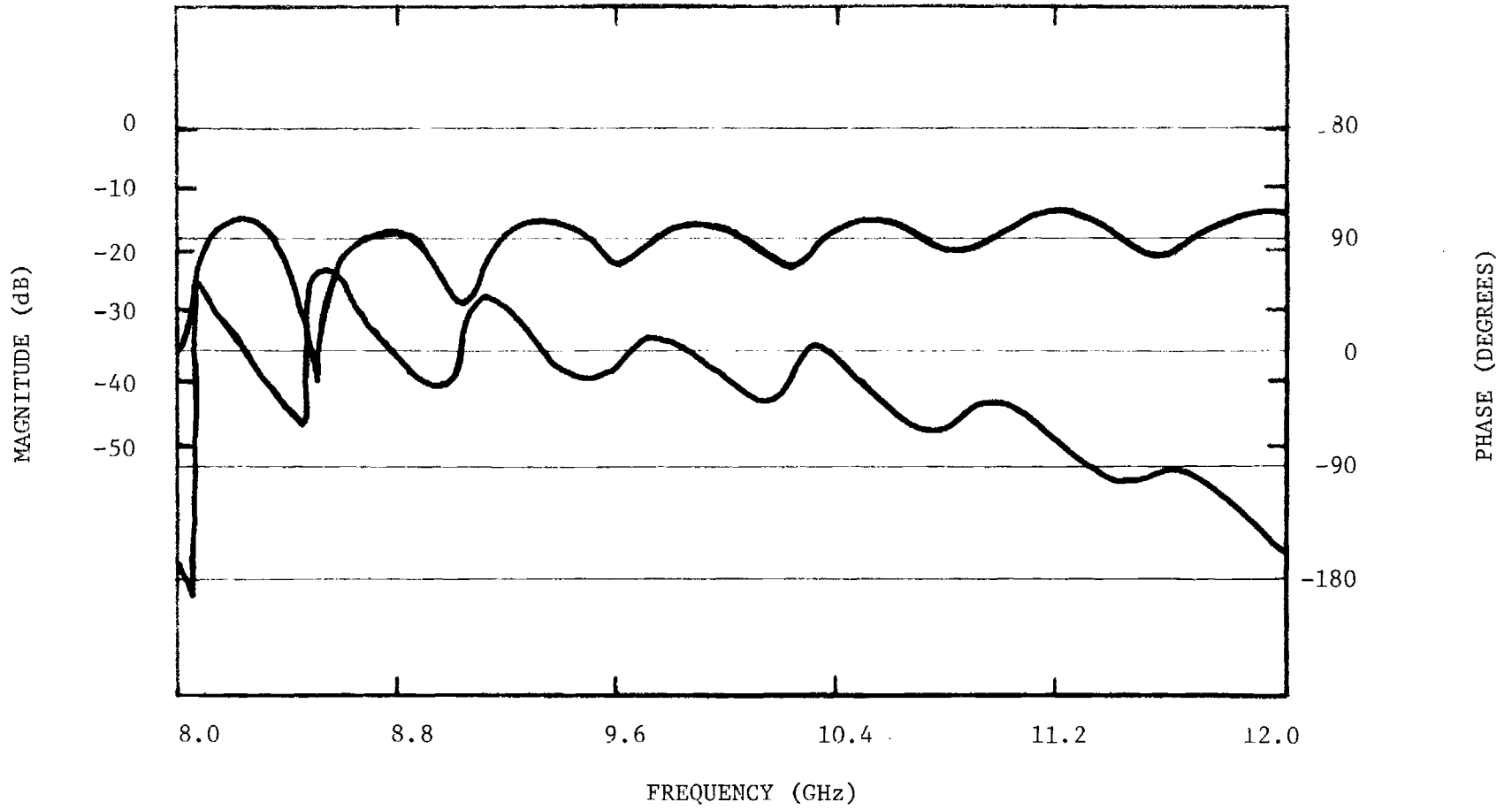


Figure 70. Return Loss From Coax-to-Waveguide Adapter and Pyramidally Shaped, Dielectric Transition in Parallel Plates with TL = 4.13 Inches. The Dielectric is Lexan and No Side Transitions are Present.

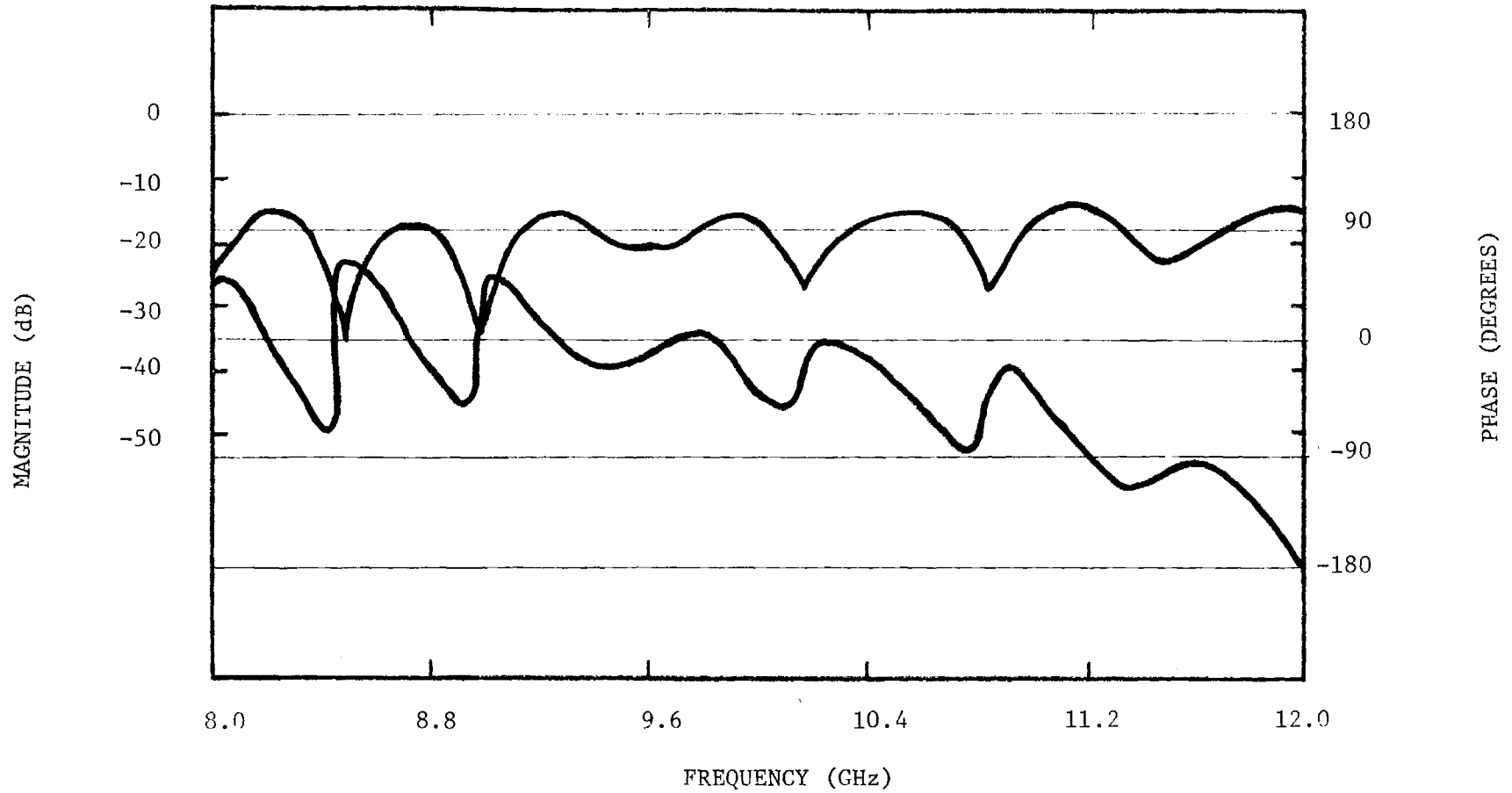


Figure 71. Return Loss From Coax-to-Waveguide Adapter and Pyramidially Shaped, Dielectric Transition in Parallel Plates with TL=4.13 Inches. The Dielectric is Lexan and There is One Transition on Either Side of the Active One.

of the two outside test sections. An oscilloscope display of the return loss and phase again indicated very little change. Similar tests using the blunt-tip tapered sections indicated the same trend. It was noted, however, that the shorter the test section, the greater the coupling between the adjacent sections.

The non-tapered blunt test sections shown in Figure 66 were also investigated for mutual coupling effects. Five test sections were made using both Lexan and Rexolite. Each test section was designed with no taper, a blunt end and a dielectric extension of 0.5 inches (out of the waveguide). Tests were made using one section, three sections, and five sections (see Figure 72). The outrigger transistions were all terminated in 50 ohm coaxial loads. Again the results indicated very little change as the number of sections increased.

A study of the preceeding data reveals a number of important points. First, the dielectric transitions will efficiently couple energy into the waveguides. Secondly, the optimum type of transition is the long tapered transition. A study of Figure 69 indicated a length of 0.65 inches gives a best return loss of 20 dB (1.22 VSWR). Optimum lengths also exist for short length transitions. Although not as broadbanded as the longer ones, they can provide satisfactory bandwidth for the cylindrical array.

C. Waveguide Slotted Arrays

Energy is coupled out of the waveguides through a series of slots cut in their walls. There are a number of slot types that can be used for this purpose. A decision was made early in the program (see Section I) to use broadwall slots. The most convenient form of broadwall slots is longitudinal shunt slots. The long dimension of these slots is parallel to the waveguide axis and the amount of power coupled out of the slot is determined by the distance the slot is displaced from the center line of the guide (dimension X in Figure 73). The position of the slots is chosen so that the power coupled out by the slots will match the desired amplitude distribution for the array. This in turn determines the elevation plane sidelobe level.

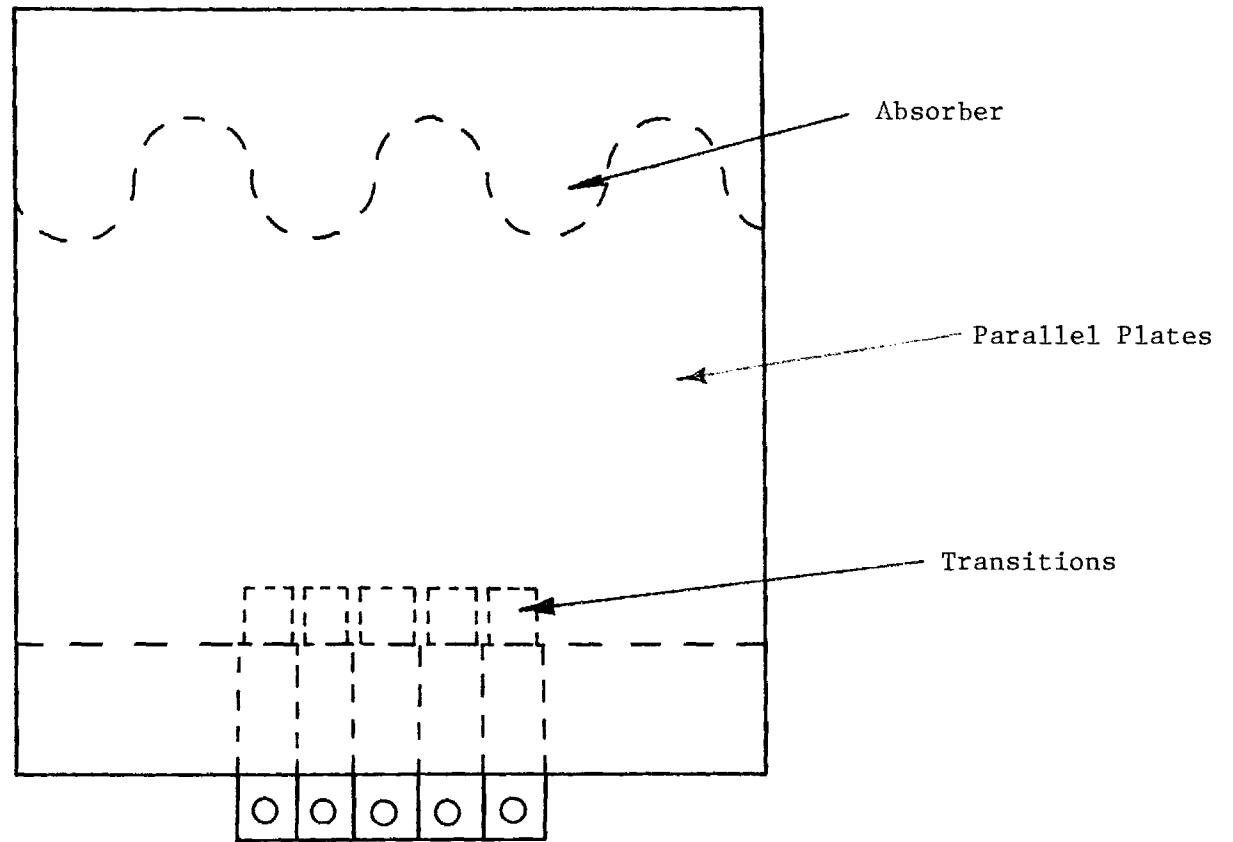


Figure 72. Configuration for Mutual Couplings Tests of Blunt Transitions Looking into Parallel Plates.

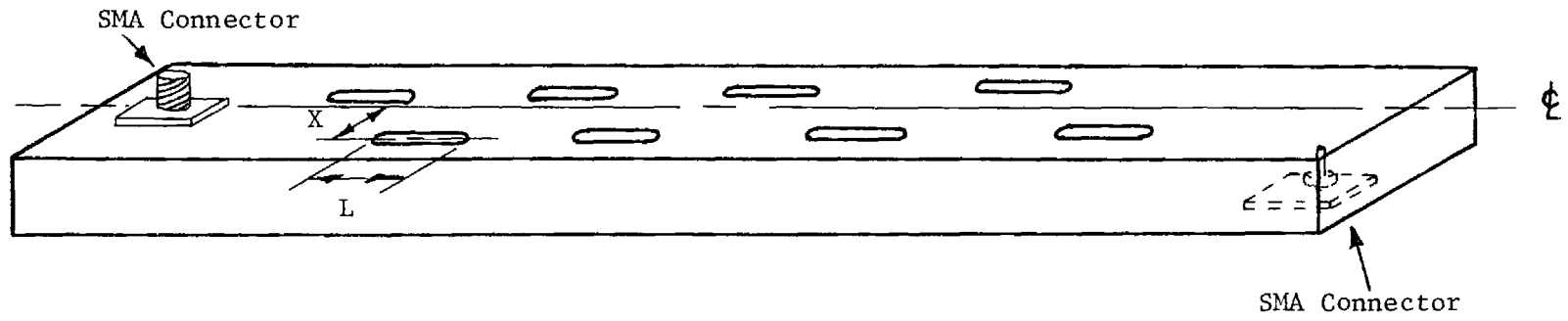


Figure 73. Illustration of an Individual Slotted Waveguide Array Used in the Partial Array.

The problem of designing the slotted arrays for this program was complicated by the fact that dielectric loading is used in the waveguide. The dielectric affects the admittance of the slot and its resonant frequency and no data could be found in the literature to accurately predict these effects. Consequently, several prototype slotted arrays were built to obtain information on these effects. Using these data the final array dimensions were selected for the partial array mock-up.

A traveling-wave array was selected since the radar frequency will be varied to produce elevation-plane scanning of the antenna beam. The basic slotted waveguide array used is shown in Figure 73. The slots were spaced slightly more than a half-wavelength apart, and the slots were alternated about the center-line of the array to keep them in phase electrically. All the slots could be kept on the same side of the center line if the slot spacing were increased to one wavelength. This, however, was discarded since it would produce excessively high grating lobes in the elevation plane of the final antenna.

D. Partial Array

A partial array was built to verify that the problem encountered under the previous contract could indeed be eliminated with the chosen design approaches and to validate and calibrate the theoretical array model. Even though the final array design is proposed for Ku-band, the partial array was built at X-band since much of the equipment was already available at this frequency and since the tolerances in building the various components would be less severe at X-band. A photograph of the partial array is shown in Figure 74. The basic support structure and parallel plate feed structure were those used under the previous contract. The parallel plate structure was modified so that the feedhorn illuminated the 47 coaxial probes directly instead of being reflected off a parabolic barrier and then onto the coaxial probes as had been done before. The position of the feedhorn was adjusted so that the phase was constant (maximum probe-to-probe phase deviation was $\pm 10^\circ$) at the coaxial pick-off probes. Semi-rigid coaxial cables (phase shifters) connect the output of the coaxial probes to the slotted waveguide sections. The lengths of the coaxial cables were selected so as to produce a collimated beam at a

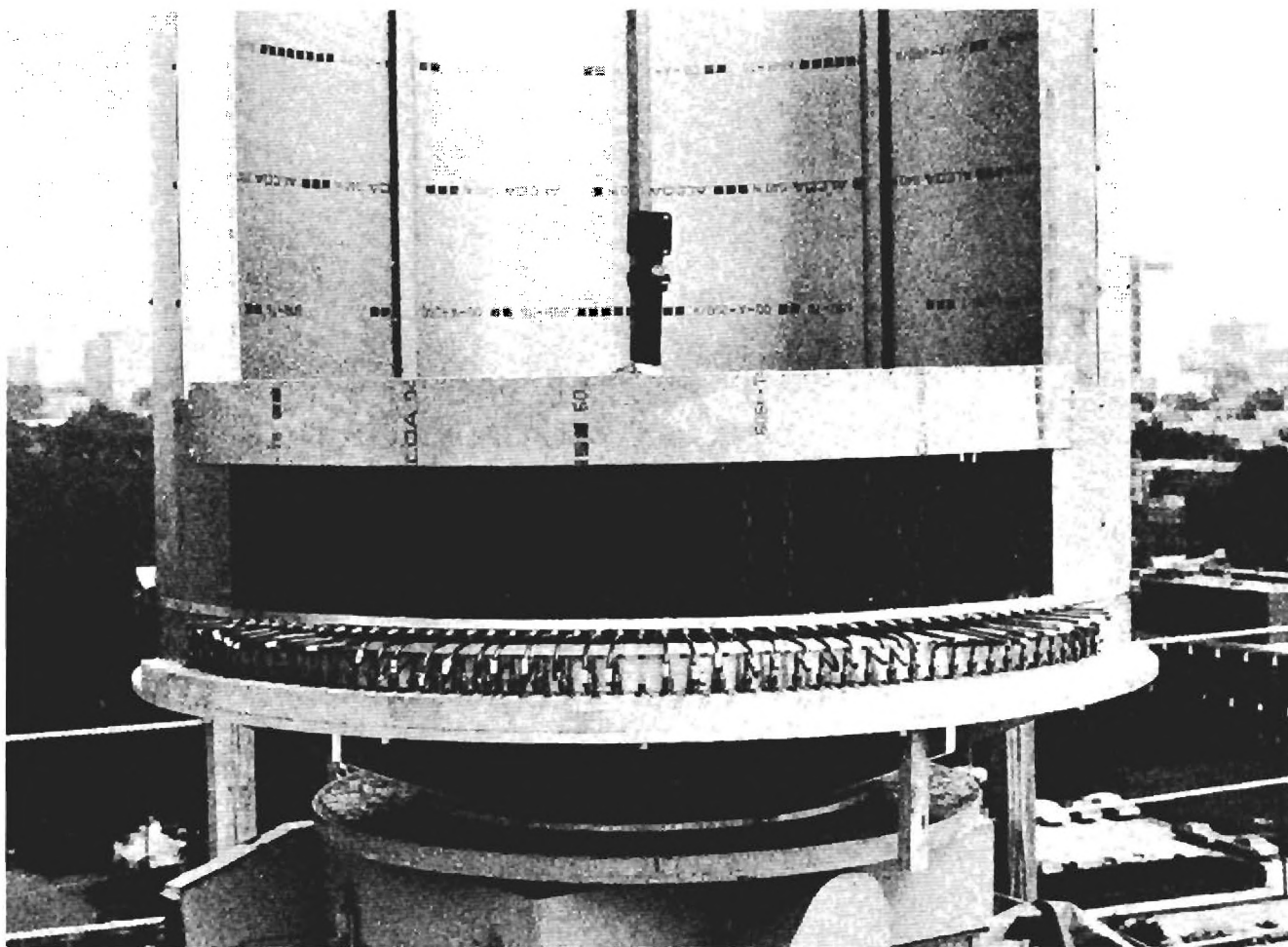


Figure 74. Photograph of Partial Array Mock-Up on Georgia Tech Antenna Range.

0° elevation angle at 8.75 GHz. The radiating waveguides covered a 114° arc of the cylinder, and the radius to the outer surface of the waveguides was 20.00 inches. Sheet metal made up the portion of the cylinder that was not covered by waveguides. The slot spacing was selected so as to produce a main beam peak at 3° elevation angle for 8.75 GHz with Rexolite filling the waveguides.

The waveguides were only made long enough (4.25") to prevent ground reflections which would occur if the array were too short (wide elevation beam). The long waveguide slotted arrays needed in the final antenna can be designed and built in a straightforward fashion. It is believed that the elevation pattern can be obtained from conventional slotted array design techniques. The main reason for building the partial array mock-up was to determine if the azimuth plane pattern could be controlled as had been predicted in the preceding theoretical sections.

The array was tested on the EES 1,000-foot, outdoor antenna range. Measured azimuth plane patterns are shown in Figure 75 - 78. The computer simulation for this case is shown in Figure 79. The computer grating lobes for this geometry ($R = 20''$, $S = 0.715''$, $\lambda = 1.35''$, and $\phi_{111} = 94.3^\circ$) should occur between 55° to 75° and be 23 dB below the main lobe. The measured grating lobe levels are -20 dB to -23 dB and are in the proper angular location. This agreement indicates that the mathematical model is accurate. The 14 - 16 dB first sidelobe levels are consistent with the aperture taper used. This taper was 7 dB at the edge of the illuminated sector and was determined by the parallel plate feed system that was used from the previous contract. The grating lobe levels will be reduced in the final array by decreasing the element spacing which can be done by making non-standard waveguides for the array. The first sidelobe levels will be reduced by increasing the azimuth taper through proper selection of the primary feed horn.

The measured azimuth and elevation beamwidths were 2.7° and 20°, respectively. The measured gain varied between 20.0 and 21.5 dBi with changing frequency. The large variation in gain appears to be the result of the VSWR varying between 1.2:1 to over 3:1. The VSWR performance of the antenna should be improved by using the dielectric transitions instead of the coaxial probes and cables.

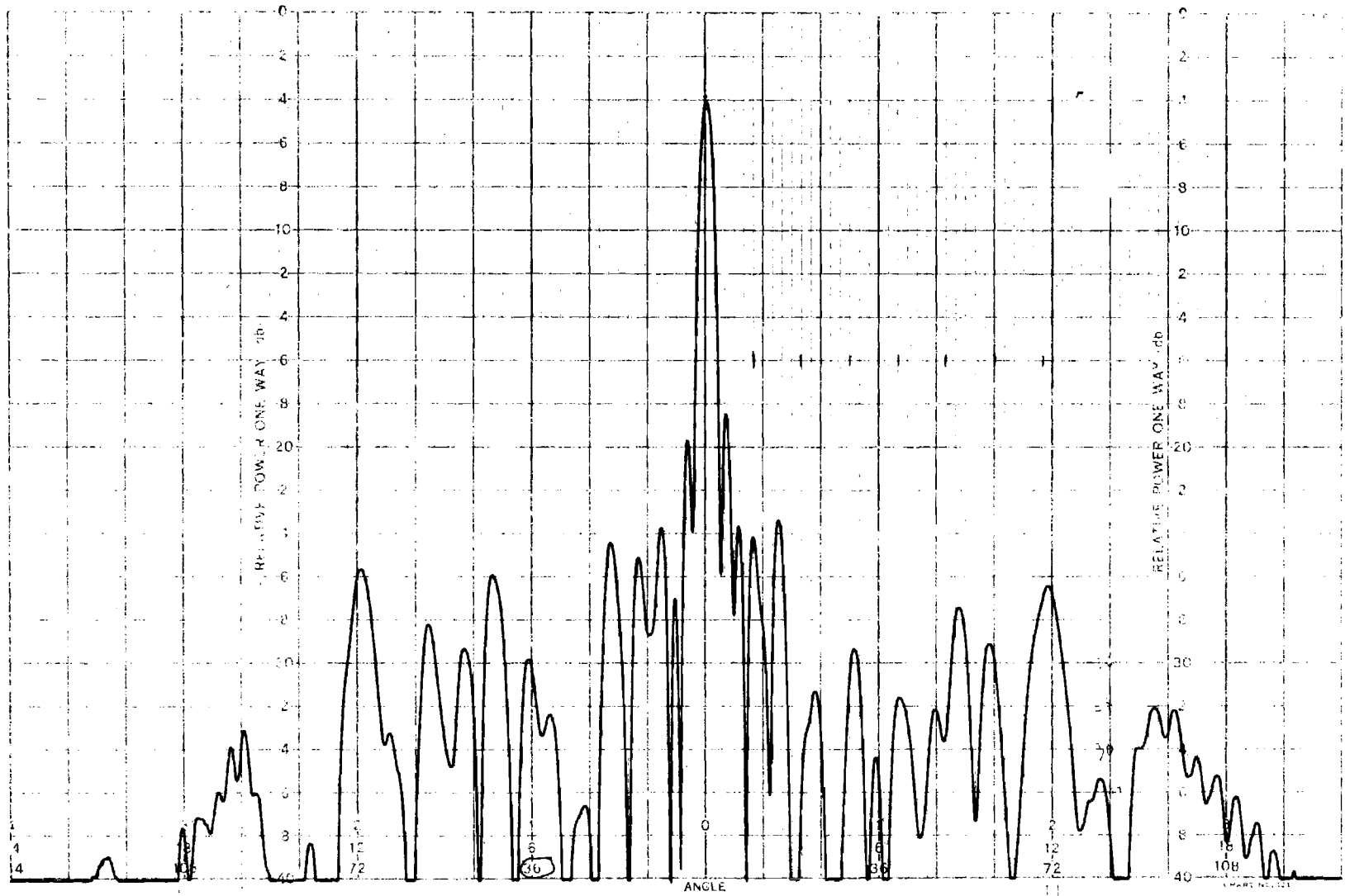


Figure 75. Azimuth Plane Pattern of Partial Array Mock-Up at 8.75 GHz.

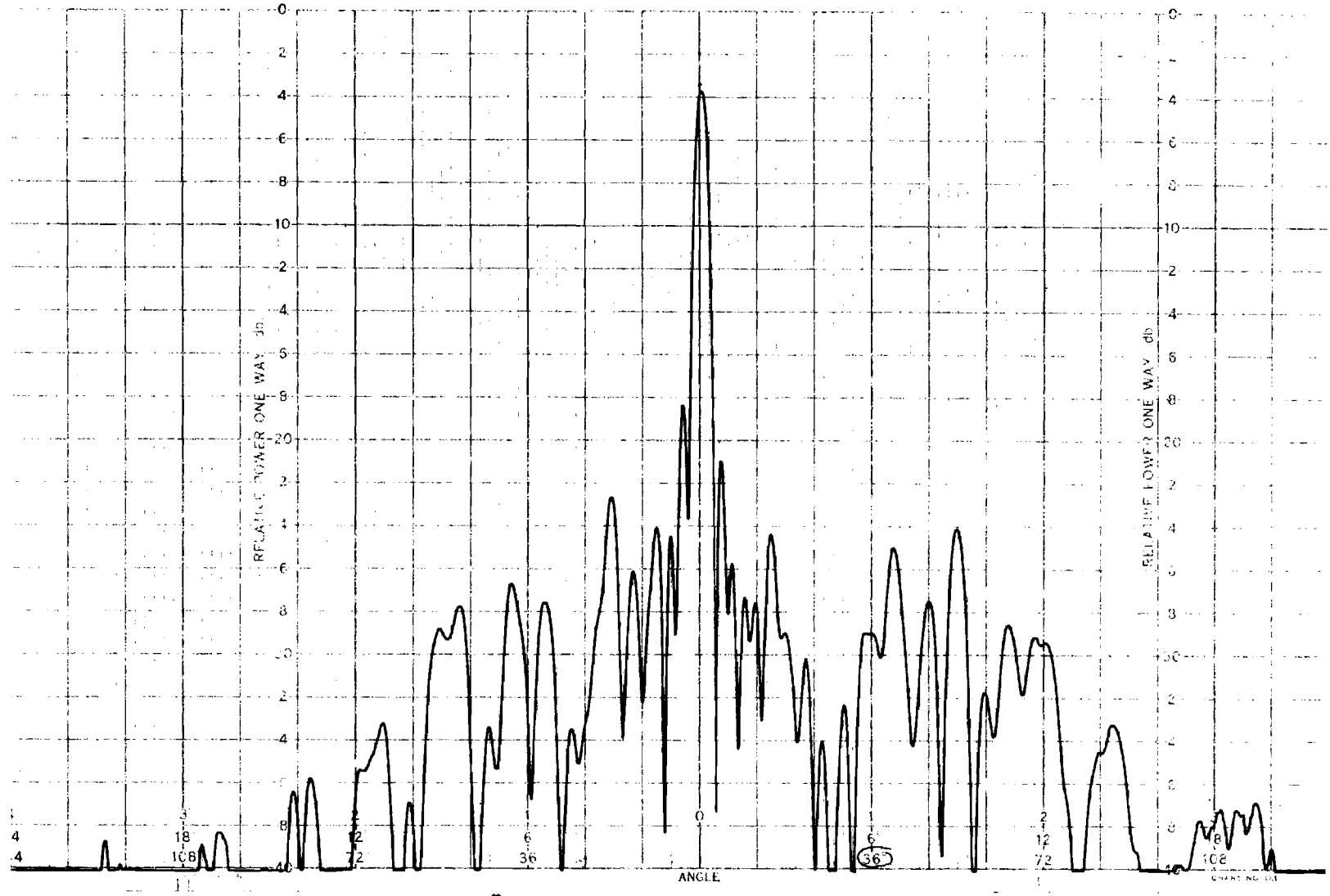


Figure 76. Azimuth Plane Pattern of Partial Array Mock-Up at 9.00 GHz.

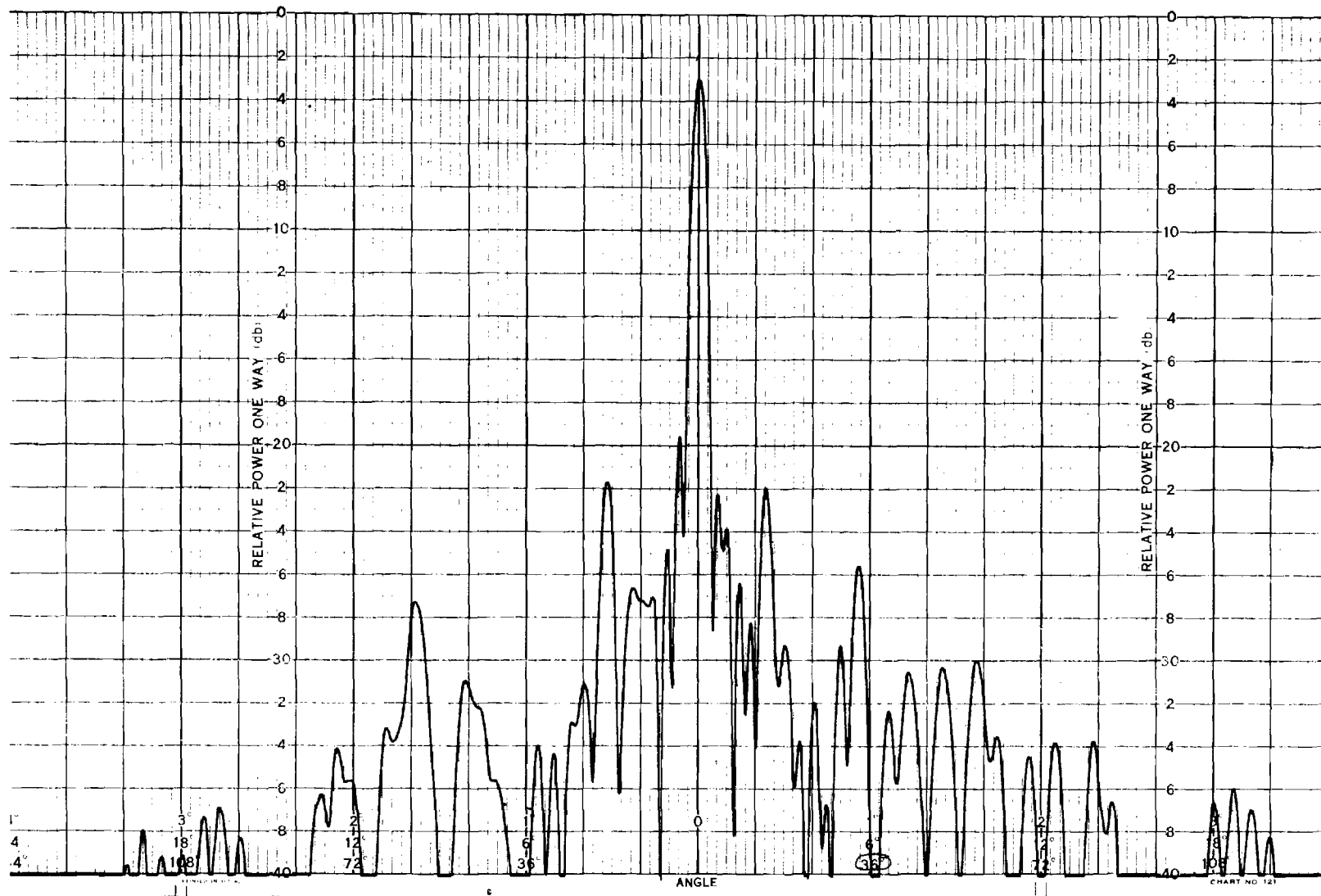


Figure 77. Azimuth Plane Pattern of Partial Array Mock-Up at 9.25 GHz.

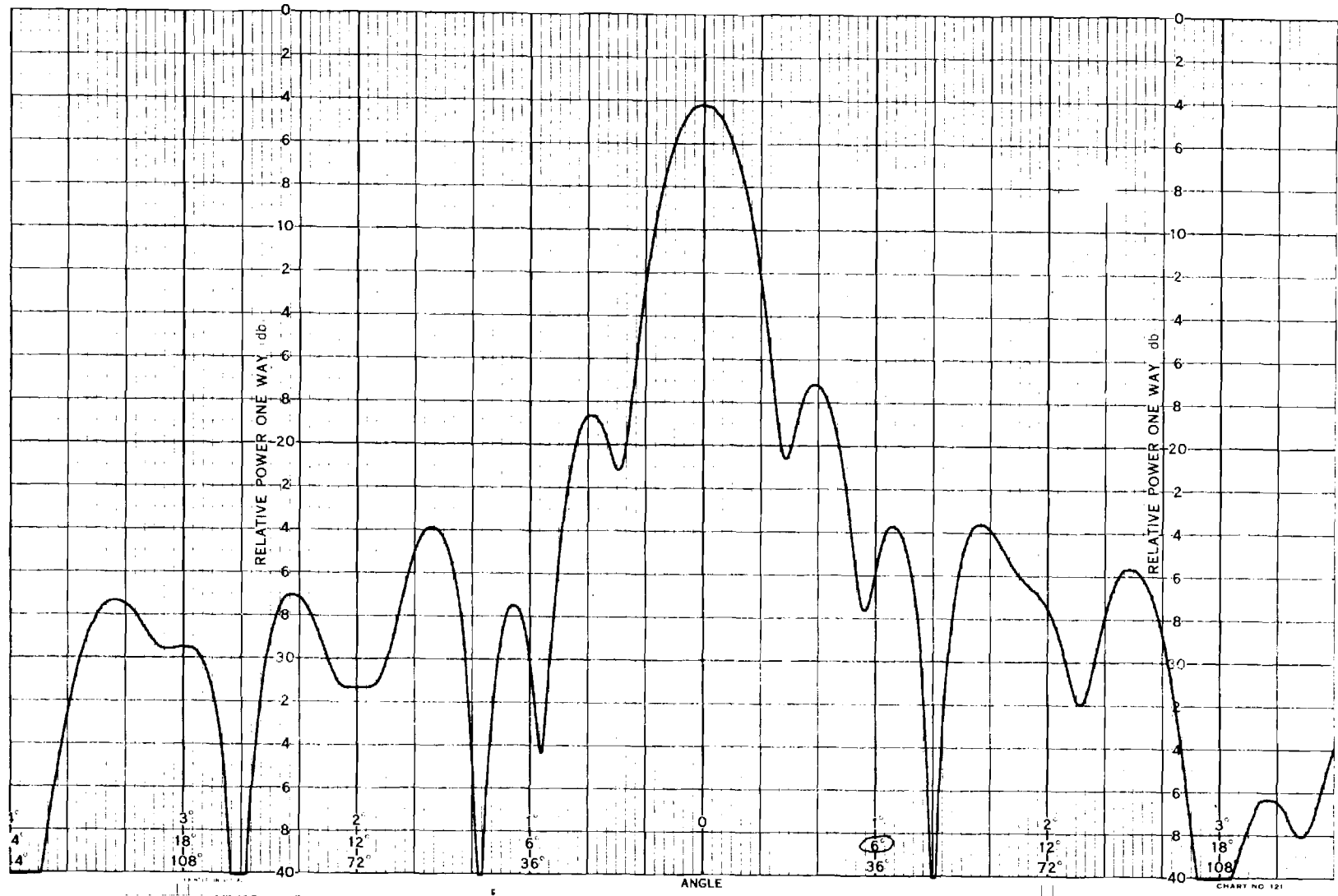


Figure 78. Expanded Azimuth Plane Pattern of Partial Array Mock-Up at 8.75 GHz.

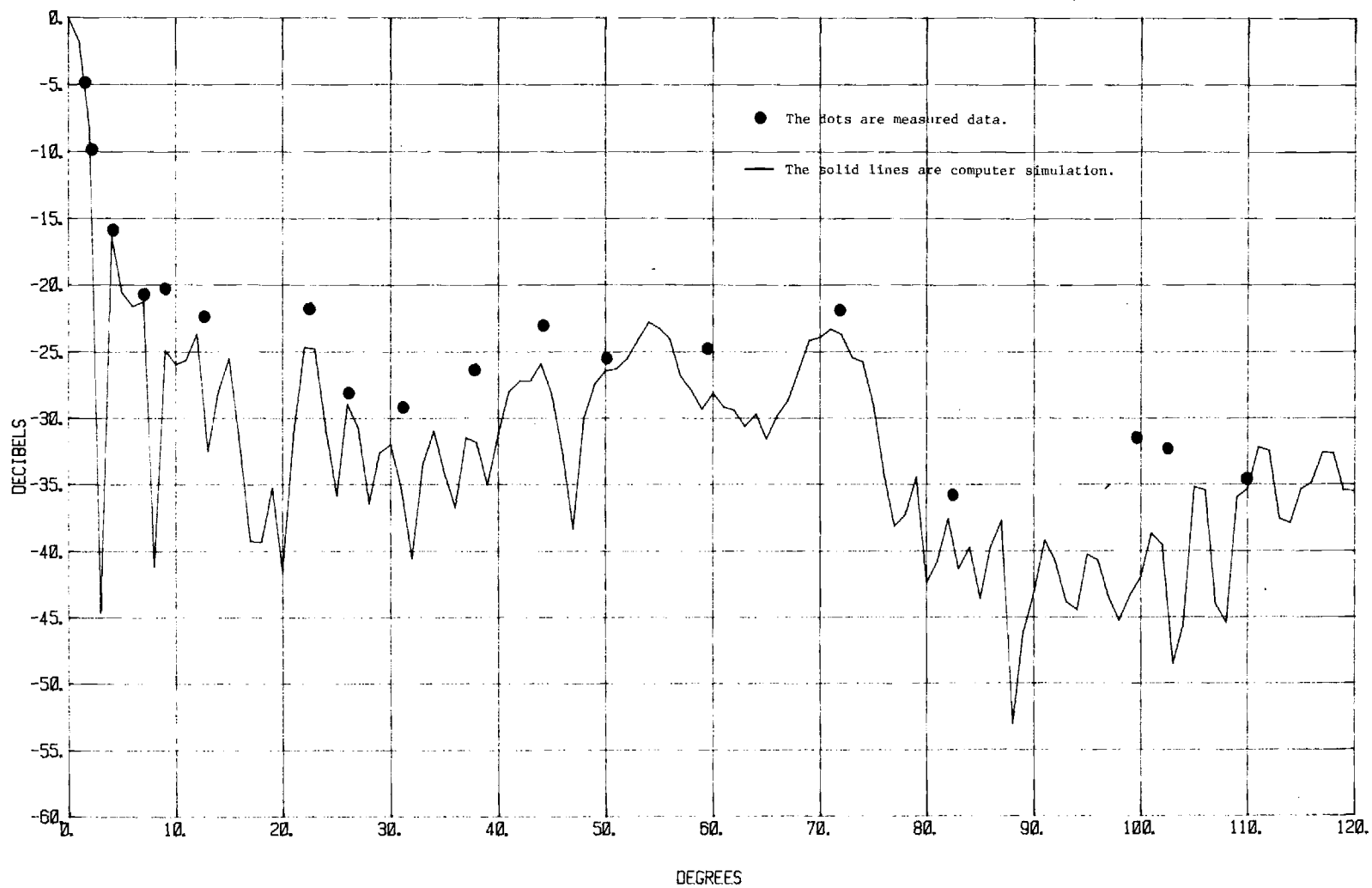


Figure 79. Computer Simulation of Prototype Array ($R = 20''$, $S = .715''$, $\lambda = 1.35''$, $\phi_{111} = 94.3^\circ$).

V. SUMMARY AND CONCLUSIONS

A design study has been performed for a lightweight, cylindrical array antenna for a hostile-mortar-locating radar system. The antenna beam must be capable of scanning 360° in azimuth and from $+3^\circ$ to $+6^\circ$ in elevation. The maximum weight of the antenna must be less than 100 pounds. A proposed design was developed which comprises (a) a cylindrical radiating structure composed of broadwall slots in dielectrically-loaded rectangular waveguide, (b) dielectric wedge transitions, and (c) a rotating geodesic lens feed horn/collimator.

The theoretical analysis performed during the program was verified by experimental data obtained during the program as well as by means of experimental and theoretical data obtained from the open literature. The work performed under this program has shown the following:

1. The theoretical model of the cylindrical array developed during this program is accurate.
2. The model permits the selection of array parameters such as element spacing, illumination sector, array diameter and illumination taper so that the desired array performance can be achieved.
3. The various breadboard components built during the program demonstrated that acceptable performance can be obtained, especially from the parallel plate-to-waveguide transition.

Based on this theoretical and experimental work it is recommended that:

1. A complete brassboard of the proposed array (Figures 37, 38, and 40) be built.
2. The frequency of operation be Ku-band.

The performance expected for the array is given in Table III and the estimated weight of the antenna is 78 pounds.

VI. REFERENCES

1. J. W. Cofer, Jr. and R. M. Goodman, Jr., "Lightweight, 360-Degree Scanning Antenna for HWL Application," Final Technical Report under Contract N00014-75-C-0229, Engineering Experiment Station, Georgia Institute of Technology, EES/GIT Project A-1713, October 1976.
2. T. S. Craven and W. H. Licata, "Lightweight Radar for HWL Applications," Final Technical Report under Contract N66001-78-C-0153, Engineering Experiment Station, Georgia Institute of Technology, EES/GIT Project A-2128, October 1978.
3. Hessel, A., "Mutual Coupling Effects in Circular Arrays on Cylindrical Surface - Aperture Design Implications and Analysis," Proceedings of 1970 Phased Array Antenna Symposium, Polytechnic Institute of Brooklyn, June, 1970.
4. Borgiotti, G. V. and Galzano, Q., "Mutual Coupling Analysis of a Conformal Array of Elements on a Cylindrical Surface," IEEE Trans. on Antennas and Propagation, AP-18, pp. 55-63, January, 1970.
5. Sureau, J. C. and Hessel, A., "Element Pattern for Circular Arrays of Waveguide-Fed Axial Slits on Large Conducting Cylinders," IEEE Trans. on Antennas and Propagation, AP-19, pp. 64-74, January, 1971.
6. Hsiao, J. K. and Rao, J. B. L., "Computer Analysis of Conformal Phased Arrays," NRL Report 7826, November, 1974.

APPENDIX

Analysis of Beamsteering Defocusing Error

The steering error can be derived from the information shown in Figure A1. The distances D_1 and D_2 can be written in wavelengths as

$$D_1 = \frac{R}{\lambda_0} \cos \theta_0 \quad (A1)$$

and

$$D_2 = \frac{R}{\lambda_0} \cos \phi \cos \theta_0 \quad (A2)$$

where λ_0 and θ_0 are the wavelength and steering angle, respectively. The difference between D_1 and D_2 is

$$\begin{aligned} \Delta D_0 &= D_1 - D_2 \\ &= \frac{R}{\lambda_0} \cos \theta_0 \{1 - \cos \phi\} \end{aligned} \quad (A3)$$

As the frequency is varied during steering, (A3) changes to

$$D_1 = \frac{R}{\lambda_1} \cos \theta_1 \{1 - \cos \phi\} \quad (A4)$$

where λ_1 and θ_1 are the new wavelength and steering angle, respectively. The new steering error then is defined as

$$\begin{aligned} \text{ERROR} &= \Delta D_1 - \Delta D_0 \\ &= \frac{R}{\lambda_0} \{1 - \cos \phi\} \left\{ \frac{\lambda_0}{\lambda_1} \cos \theta_1 - \cos \theta_0 \right\} \end{aligned} \quad (A5)$$

Error information is shown in Table A1. This table indicates that for $\theta_1 = 6^\circ$ is equal to $0.133 \lambda_0$ ($\phi_{111} = 90^\circ$, $R = 12''$). For the case of $\theta_0 = 4.5^\circ$, the defocusing error associated with a steering angle of $\theta_1 = 6^\circ$ is $0.093 \lambda_0$. This shows the defocusing error to be less for the system designed to operate at the arithmetic mean frequency. This is as expected since the frequency shift between the design angle (θ_0) and the shift angle (θ_1) is much less for the arithmetic mean case.

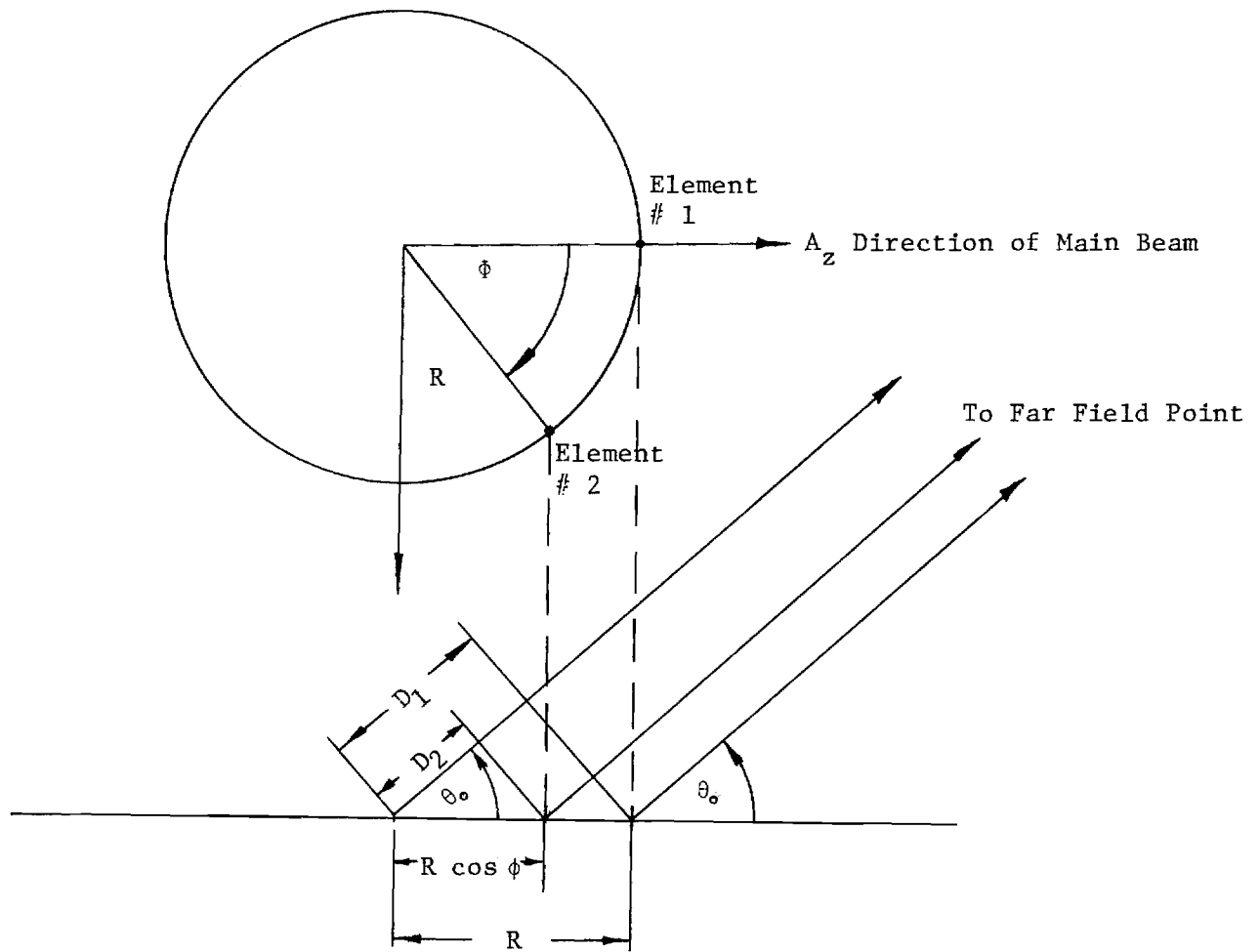


Figure 80. Diagram Showing Elevation Scanning.

TABLE A1
Steering Angle Errors

R	ϕ	θ_0	θ_1	λ_0	λ_1	ERROR
12"	45°	3°	6°	0.72"	0.698"	0.133 λ_0
12"	60°	3°	6°	0.72"	0.698"	0.227 λ_0
12"	75°	3°	6°	0.72"	0.698"	0.336 λ_0
12"	45°	4.5°	6°	0.709"	0.698"	0.093 λ_0
12"	45°	4.5°	3°	0.709"	0.72"	-0.067 λ_0
24"	45°	3°	6°	0.72"	0.698"	0.266 λ_0
24"	60°	3°	6°	0.72"	0.698"	0.454 λ_0
24"	75°	3°	6°	0.72"	0.698"	0.672 λ_0